Master's thesis

NTNU
Norwegian University of Science and Technology
Faculty of Natural Sciences
Department of Materials Science and Engineering

Magnus Lydvo Aas

Bimetallic Additive Manufacturing of IN718-CuAl7 for Tailored Functionalities

A Study in Mechanical Properties and Microstructural Features

Master's thesis in Materials Science and Engineering
Supervisor: Bjørn Holmedal
Co-supervisor: Håkon Linga
June 2023

NTNU
Norwegian University of
Science and Technology

Magnus Lydvo Aas

Bimetallic Additive Manufacturing of IN718-CuAl7 for Tailored Functionalities

A Study in Mechanical Properties and Microstructural Features

Master's thesis in Materials Science and Engineering
Supervisor: Bjørn Holmedal
Co-supervisor: Håkon Linga
June 2023

Norwegian University of Science and Technology
Faculty of Natural Sciences
Department of Materials Science and Engineering

NTNU
Norwegian University of
Science and Technology

Preface

This thesis represents the culmination of a five-year Master's degree in Materials Science and Engineering at the Department of Materials Science, Norwegian University of Science and Technology (NTNU). The research has been conducted during the spring of 2023 at the Department of Materials Science and serves as a continuation of the author's project report from autumn 2022.

The work was conducted in collaboration with SINTEF Manufacturing in Trondheim operating the 3D printer and providing the additive manufacturing material. This work aims to address the mechanical properties of laser metal wire deposition of CuAl7 onto IN718 and the microstructural features obtained to exploit the combined properties in industrial applications.

I want to thank my supervisor Bjørn Holmedal for his valuable expertise and patient supervision. I would also like to thank Håkon Linga and Trond Arne Hassel for the guidance on laboratory work and for sharing interesting and helpful knowledge. I want to thank Pål Christian Skaret for his help on the tensile tests, Ruben Åge Hansen for advising me regarding sample preparation and hardness testing, and Yingda Yu for giving me guidance on scanning electron microscopy.

Finally, I would like to thank my family and friends for supporting me, and to fellow students for the five fantastic years we have had together in Trondheim.

Trondheim, June 2023
Magnus Lydvo Aas

Abstract

Additive manufacturing, also known as 3D printing, of multi-material parts has proved to be valuable in solving engineering problems compared to traditional manufacturing processes and single-material parts. By including two or more alloys the desired intrinsic properties from each material can be combined to produce parts with tailored functionalities. In aerospace applications, high-performance components are needed to withstand harsh environments and strong forces. Inconel 718 has been widely used in the aerospace industry as it is a high-strength material, also at elevated temperatures, with high chemical and fatigue resistivity. However, the poor heat conductivity of Inconel 718 results in unwanted high heat accumulation. Aluminium bronzes, in this case, CuAl7, exhibit high thermal conductivity, making them suitable for cooling applications. These two materials can be combined to possess improved properties, desirable in high-performance applications such as rocket nozzles experiencing extreme temperature and pressure conditions. Additive manufacturing by laser metal wire deposition offers cost-efficient and clean material processing in addition to high deposition rates compared to other additive manufacturing techniques. It is based on a layer-by-layer deposition method and provides strong metallic interlayer bonding, important for the mechanical performance of the manufactured part.

The as-deposited material was investigated in light optical microscopy and scanning electron microscopy. Backscatter electron imaging, energy dispersive spectroscopy and electron backscatter diffraction was utilized for the microstructural characterization. The bimetallic interface showed good fusion with strong metallurgical bonding and the two materials exhibited high compatibility. Equiaxed nickel-rich dendrites, intermetallic phases and various types of particles formed in and around the boundary, including Laves phase and κ phases.

The mechanical properties of the as-deposited material were tested by tensile tests with different orientations and hardness tests. The fracture areas of the tensile specimens were examined to reveal fracture properties and for ductility measurements. Inconel 718 demonstrated high strength values while CuAl7 exhibited low strength, high ductility values and extraordinary strain hardening. The samples obtained from the interface showed low uniform strain values, fracture strain values as that for CuAl7 and a strength between that of the two distinct materials. The hardness at the bimetallic boundary was seen to be up to 400 HV0.5, while that of Inconel 718 and CuAl7 was 300 HV0.5 and 100 HV0.5, respectively. Different strengthening mechanisms were considered, including twinning, particle strengthening and deformation hardening, stemming from the microstructural features.

Sammendrag

Additiv produksjon, også kjent som 3D-printing, av multimaterialdeler har vist seg å være verdifullt for å løse ingeniørproblemer sammenlignet med tradisjonelle produksjonsprosesser og énmaterialkomponenter. Ved å inkludere to eller flere legeringer kan de ønskede iboende egenskapene fra hvert material kombineres for å produsere komponenter med skreddersydd funksjonalitet. Innen romfartsapplikasjoner er det stort behov for komponenter med høy ytelse som tåler tøffe miljøer og sterke påsatte krefter. Inconel 718 har blitt mye brukt i romfartsindustrien fordi det er en sterk legering med høy kjemisk- og utmattelsesbestandighet, også ved høy temperaturer. På den annen side fører den lave termiske ledningsevnen til Inconel 718 til uønsket høy akkumulasjon av varme. Aluminiumbronser, i dette tilfellet CuAl7, har høy termisk ledningsevne, noe som gjør legeringene egnet for kjølingsapplikasjoner. Disse to materialene kan kombineres for å oppnå forbedrede egenskaper som er ønskelige i høytytende applikasjoner, for eksempel rakettdyser som utsettes for ekstreme temperatur- og trykkforhold. Additiv produksjon med laser og metalltråd tilbyr kostnadseffektiv og ren materialbehandling i tillegg til høy deponeringshastighet sammenlignet med andre additive produksjonsmetoder. Denne metoden er basert på en lag-for-lag-prosessteknikk og gir sterke metalliske bindinger mellom lagene, noe som er viktig for den mekaniske ytelsen til den ferdigstilte komponenten.

Det 3D-printede materialet ble undersøkt ved hjelp av lysmikroskopi og skanning- elektronmikroskop. Tilbakespredte elektron-bilder (backscatter electron imaging), energidispersiv spektroskopi (energy despersive spectroscopy) og elektron-tilbakespredningsdiffraksjon (backscatter electron diffraction) ble brukt for karakterisering av mikrostruktur. Høy grad av sammensmelting med sterk metallurgisk binding ble oppnått i det bimetalliske grensesnittet som resultat av god kompatibilitet mellom materialene. Ekviaksede nikkelrike dendritter, intermetalliske faser og ulike typer partikler dannet seg i og rundt grensesnittet, inkludert Laves-fase og κ-faser.

De mekaniske egenskapene til det printede materialet ble testet ved hjelp av hardhetstesting og strekktesting i ulike retninger. Bruddflatene til strekkprøvene ble undersøkt for å avdekke bruddegenskaper og for duktilitetsmålinger. Inconel 718 viste høye styrkeverdier, mens CuAl7 viste lav styrke, høye duktilitetsverdier og ekstraordinær arbeidsherding. Prøvene som ble hentet ut fra grensesnittet viste lave verdier for uniform tøyning, bruddtøyningsverdier som de for CuAl7 og en styrke tilsvarende en mellomverdi av de to rene materialene. Hardheten i det bimetalliske grensesjiktet ble målt til å være opptil 400 HV0.5, mens hardheten for Inconel 718 og CuAl7 var henholdsvis 300 HV0.5 og 100 HV0.5. Ulike styrkemekanismer ble vurdert, inkludert partikkelbidrag, tvillingdannelser (twinning) og deformasjonsherding, med utspring fra mikrostrukturelle egenskaper.

Abbreviations

Nomenclature

Abbreviation	Full name
Al	Aluminium
AM	Additive Manufacturing
a	Angular (With An Angle)
B	Boron
BSE	Backscatter Electron
bcc	Base Centered Cubic
bct	Body Centered Tetragonal
C	Carbon
Co	Cobalt
Cr	Chromium
Cu	Copper
DED	Directed Energy Deposition
EBSD	Electron Backscatter Diffraction
EDS	Energy Dispersive Spectroscopy
Fe	Iron
fcc	Face Centered Cubic
GB	Grain Boundary
h	Horizontal
IN718	Inconel 718
IPF	Inverse Pole Figure
IQ	Image Quality
LMD	Laser Metal Deposition
LMWD	Laser Metal Wire Deposition
LOF	Lack Of Fusion
LOM	Light Optical Microscopy
Mn	Manganese
Mo	Molybdenum
NAB	Nickel Aluminium Bronze
Nb	Niobium
Ni	Nickel
P	Phosphorus
PBF	Powder Bed Fusion
S	Sulphur
SE	Secondary Electron
SEM	Scanning Electron Microscopy
Si	Silicon
SLM	Selective Laser Melting
SS	Solid Solution
Ta	Tantalum
Ti	Titanium
v	Vertical

List of Symbols

Symbol	Description	Unit
A_0	Initial area	mm^2
A_u	Uniform area	mm^2
A_f	Fracture area	mm^2
d	Hatch spacing	mm
D	Grain diameter	mm
e	Nominal strain (engineering strain)	[%]
e_u	Uniform strain (uniform elongation)	[%]
P	Laser power	W
P_w	Hot-wire power	W
s	Nominal strength (engineering strength)	MPa
s_u	Ultimate tensile strength	MPa
v_t	Traverse speed (scanning speed)	mm/s
v_w	Wire feed rate (wire speed)	mm/s
Z	Relative laser focal position	mm
ε_f	True fracture strain	[%]
ε_u	True uniform strain	[%]
σ_u	True ultimate tensile strength	MPa
σ_y	Yield strength	MPa

Table of Contents

List of Figures

List of Tables

1 Introduction

1.1 Background and motivation

Additive manufacturing (AM) has experienced substantial advancements over the past few decades and is now widely used in the design and manufacturing of high-performance components. The application of AM processes has increasingly expanded to various industrial sectors including energy, automotive, medical and aerospace (DebRoy et al. 2017). The methodology of additive manufacturing offers precise manufacturing of intricate 3D components that are unattainable through conventional processes like casting, thus highlighting its profound value in future markets. However, despite significant advancements in AM for various materials, including steel, aluminium alloys and nickel-based superalloys, challenges remain in producing cost-effective standardized components with consistent properties.

Over the years, numerous AM methods have been developed, categorized into distinct techniques such as Direct Energy Deposition (DED) and Powder Bed Fusion (PBF). In total, seven distinct categories have been defined in ISO/ASTM 52900 (ISO/ASTM 2021). These techniques differ based on the heat source used, such as lasers or electron beams, which melt the feedstock material consisting of either wire or powder. The molten material is subsequently solidified and bound to the substrate. Laser Metal Deposition (LMD) is a DED process known for its high deposition rates, clean processing and high surface performance, involving lower costs compared to powder-based systems. Moreover, this project focuses on laser metal deposition with wire feedstock, taking advantage of its favourable characteristics and suitability for the project objectives.

Bimetallic structures can exhibit remarkable properties by tailoring distinct functionalities from different materials. By combining the high strength and fatigue properties with high thermal conductivity, high-performance aerospace components such as rocket nozzles can be obtained. Few studies have been conducted regarding LMD of bimetallic AM using Inconel 718 and CuAl7. The aim of this thesis is therefore to investigate the mechanical properties, in terms of strength, ductility and hardness, of the bimetallic structure assessing the properties of the interface and compare these to the pure alloys. In addition, the microstructure will be addressed and its impact on the mechanical properties of the 3D printed material.

2 Literature review

2.1 Additive Manufacturing

Additive manufacturing (AM) includes a range of manufacturing technologies. Unlike subtractive fabrication methods, AM relies on layer-by-layer techniques of one or multiple materials, resulting in reduced waste and significantly shorter lead times. Initially limited to the production of porous structures and prototypes, AM has evolved to meet industrial requirements enabling the manufacturing of dense, high-quality parts (Herzog et al. 2016). Research in the AM community reveals a significant potential for AM to emerge as a viable option in serial production in various industries (Bourell 2016; Murr et al. 2012; Appleyard 2015). However, to enhance commercial attraction in the field, further advancements are required in hardware-software integration, affordability of equipment, automation, and overall development. The most common AM methods utilize welding techniques, employing heat sources such as arcs, electron beams, lasers, and plasma. These methods offer unique advantages, having the possibility to construct complex 3D parts without the need for dies or moulds. Furthermore, the digital models used can be stored and reused, enabling precise component reproduction (Oliari et al. 2017).

Direct-to-metal processes, such as Powder Bed Fusion (PBF) and Direct Energy Deposition (DED), initiate with a computer model that directly translates into a net-shaped part (DebRoy et al. 2017). These processes offer significant advantages in terms of effectiveness and time-saving, although some post-processing steps such as surface finishing and heat treatment often are required. In contrast, indirect processes necessitate additional processing steps, e.g. machining or casting, after the printing of the part. Although there are challenges with the printing of some materials, research has revealed the possibility of using a wide range of materials for AM purposes (DebRoy et al. 2017; Lewandowski and Seif 2016). Commonly employed metals include steel, aluminium alloys, nickel-based superalloys, copper alloys and titanium alloys. Other metallic materials may be utilized, either in pulverized form or as wire feedstock, although more research is needed in the field (Herzog et al. 2016).

2.1.1 Multi-material additive manufacturing

The possibility to produce multi-material components from AM has been on the radar for a few years. Multi-material additive manufacturing (MMAM) offers the possibility to combine single material properties in the same component. Bandyopadhyay et al. 2022 have published a review on additive manufacturing of bimetallic structures, covering different AM processing strategies, characterization techniques, the challenges involved and further work. An illustration of different metal processes and the respective properties is presented in Figure 1. As pure metals exhibit poor multidiscipline functionalities, they could be alloyed by conventional processing methods to achieve enhanced properties such as mechanical properties and corrosion resistance. In the later years, a higher complexity of properties and geometries, including site-specific functionalities, have been demanded in high-performance parts. Additive manufacturing meets the requirements for producing such components, but conventional manufacturing could also be utilized (Bandyopadhyay et al. 2022). AM of multi-material structures also brings challenges. The binding between the different materials needs to be of sufficiently high quality, i.e. a strong bonding between the two materials, and the formation of intermetallic phases and cracks needs

to be controlled and assessed.

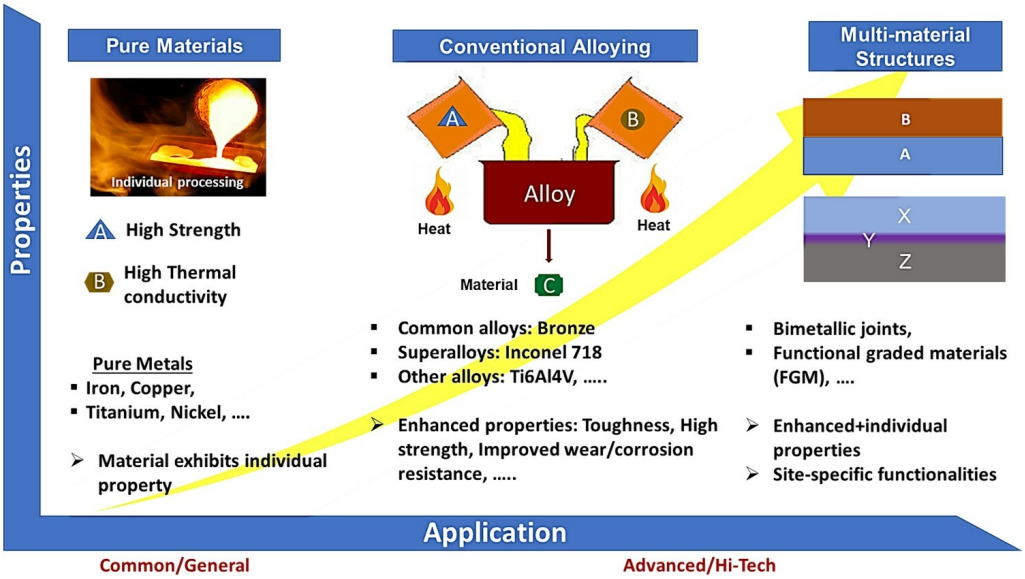

Figure 1: Illustration of different processing methods and its effect on material properties. From Bandyopadhyay et al. 2022, copyright 2022 by The Author(s).

Several publications have been found regarding MMAM of components for aerospace applications, but more studies are needed to fully understand the material features when combining different alloys in bimetallic structures. C. Wang et al. 2020 discuss the combination of titanium alloys with high specific strength and Inconel alloys with high-temperature performance, including an interlayer of tantalum/copper (Ta/Cu) to achieve high-quality bonding between the two materials. Bimetallic AM of Inconel 718 (IN718) and Cu have been reviewed applying powder bed fusion (A. Marques et al. 2022; Ringel et al. 2022), hot pressing sintering (Ana Marques et al. 2022) and direct energy deposition (Onuike et al. 2018). Specific research regarding the DED of bimetallic additive manufacturing of IN718 and CuAl7 was not found. However, more publications assess AM of nickel aluminium bronzes (NAB), possessing some of the same chemical content as a mix of IN718 and CuAl7 (Ni, Fe, Cu, Al) (Dharmendra et al. 2021; Orzolek et al. 2022; Cai et al. 2022).

2.2 Laser metal deposition

Laser metal deposition (LMD) is a direct energy deposition (DED) method and can use both powder or wire as feedstock material. There is a wide range of applications where LMD techniques are used, such as in the production of turbine blades and gears or in repairing damaged parts by cladding (Herzog et al. 2016). They offer high surface performance on engineering components and a variety of high-quality coatings. The advantages of LMD, compared to common techniques of thermal spraying and welding, are low dilution, the low extent of pores, and strong metallurgical bonds, a key factor when cladding layers on different substrates (Abioye, Medrano-Tellez et al. 2017). In terms of saving potentials, LMD with wire, or laser metal wire deposition (LMWD), has proved to be more appreciated than powder-based systems, such as powder-feeding LMD and powder bed fusion (PBF). LMWD offers better surface finish and higher material deposition rates, but also increased operational safety (Zapata et al. 2016) and reduced costs, both environmental

and economical, due to a cleaner processing environment the effective deposition method (Abioye, Folkes et al. 2013). The many advantages have led wire as feedstock to a more and more standardized technique. Due to the improved surface finish and a more focused energy supply than wire and arc additive manufacturing (WAAM), for instance, laser and electron-based heat sources are more consequently used to produce net-shaped parts.

2.2.1 Printing method

The printing method has a high influence on both the mechanical properties, solidification structure and the formation of defects in the as-deposited material. Process control and monitoring are therefore essential in wire-based DED systems (Dass and Moridi 2019). The main process parameters in LMWD are the laser power (P), wire traverse speed (v_t), wire feed rate (v_w), relative focal position (Z) and hatch spacing (d). Much research has been given to the examination of the relationships between these process parameters in different AM materials (Bombach et al. 2018; Zapata et al. 2016; Motta et al. 2018; Abioye, Folkes et al. 2013). It is seen that process control, in addition to post-processing such as heat treatment, is important to obtain the desired material quality in terms of defects, microstructure, mechanical properties and surface finish.

A consequence of low heat input or other suboptimal printing parameters may lead to defects in the material such as lack of fusion, porosity, surface roughness and residual stress cracking (DebRoy et al. 2017). An energy density is generated around the wire close to the deposition surface and creates a melt pool (weld pool), seen from Figure 2. The focal point determines the laser spot size and must be adjusted according to the wire feed rate and laser power to give sufficient melting of wire (Motta et al. 2018). The traverse speed is also influencing the deposition and needs to be set according to the values of the laser power and the traverse speed. Hatch spacing is the overlapping distance between each interlayer bead, and an optimized hatch spacing is needed to prevent gaps or lack of fusion in the overlapping region. In addition, the LMWD equipment is often installed with a hot-wire system, making it possible for the wire feedstock to be preheated before entering the melt pool. This is an advantage for inducing higher energy inputs to the melt pool in order to achieve sufficient wire melting. Bombach et al. 2018 found that the activation of hot-wire led to larger recrystallized regions between the deposition layers by LMD with IN718 due to the reheating of previous layers.

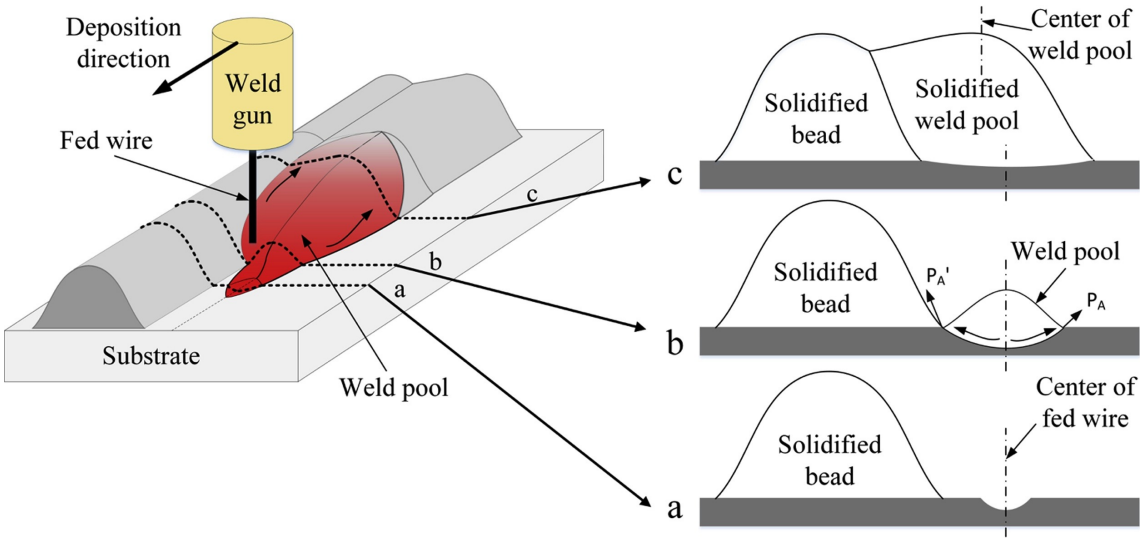

Figure 2: Overlapping beads applied by a wire feeding AM method and cross-section profiles at three different positions. From Li et al. 2018, copyright 2017 by Elsevier B.V.

2.3 Temperature distribution

The temperature changes the AM material undergoes are of great importance to understanding the solidification structure and texture in the deposition material. The thermal history in AM processes, especially in terms of local cooling rates, is the main factor in predicting the final microstructure, such as the formation of dendrites and cell structure. The solid-state transformations that are present during building can also be determined and are highly dependent on the alloy system used.

In addition to the temperatures, the thermal properties of both the substrate material and the deposited metal have a great influence on the final solidification structure in the AM part. The melt pool is able to exceed the liquidus temperature of the alloy by several hundred degrees Celsius. The maximum temperature can reach even higher than the boiling point. Figure 3a) and b) illustrates a 3D schematic of the temperature distribution along the deposition direction. Due to a high scanning speed, the melt pool is elongated behind the heat source, while it is compressed in front of it. The heat is transferred from the melt pool, where the temperature is at its highest, to the previously deposited material and further down to the substrate. During the deposition of the first few layers, the substrate works as a heat sink, and the substrate can be actively cooled to control the heat distribution in the AM part during deposition. But as more and more layers are built, the heat sink effect decreases due to the heat loss to adjacent deposition material. As a result, the melt pool size and peak temperature will increase with the increasing number of layers. Materials with low thermal conductivity, such as IN718, will accumulate more heat than high thermal conductive alloys, such as CuAl7.

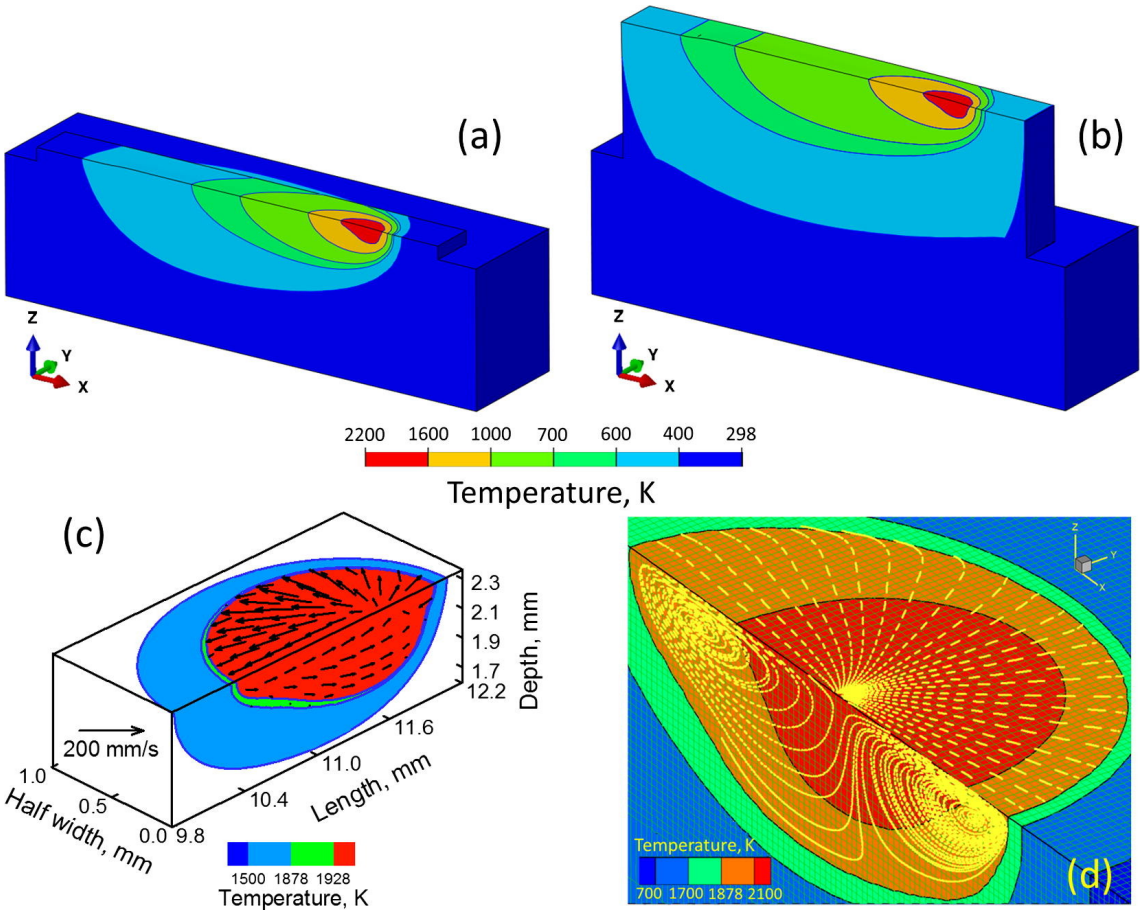

Figure 3: Temperature distribution during deposition with LMD with IN718 powder using 300W laser power and 15mm/s traverse speed. The scanning direction of the laser beam is along the positive x-axis. The figure shows the temperature distribution in a) the 1st layer and b) the 10th layer. c) and d) shows the pool shape of the 10th layer and the circulation inside the molten metal pool driven by surface tension gradient, respectively. From DebRoy et al. 2017, copyright 2017 by Elsevier Ltd.

In AM processes, the produced part will experience multiple heat increases during building. Figure 4a) shows the influence of temperature along the bead width direction (y-axis) of a single bead deposition of IN718. y=0 is the melt pool centre, from which the temperature decreases gradually towards the perimeter of the laser. The local cooling rate is seen to be very rapid, which is typical for AM processes. It takes only a couple of hundred milliseconds for the material to cool 2000℃. The cooling rate in a thermal cycle is influenced by the peak temperature and the position it is measured relative to the applied layer. The material properties, the geometry of the component and the type of manufacturing process also governs the heat accumulated and thus the temperature gradient. The cooling rate have a high influence on the microstructure, with higher cooling rates depress diffusion which results in fine gain structure (Ana Marques et al. 2022). Table 1 presents an overview of typical cooling rates in AM processes compared to conventional casting and laser welding. It is seen that LMDs have cooling rates similar to that of conventional welding, and observations in welds can therefore be used to understand the temperatures the as-deposited material in LMD processes undergo. From Figure 3b) it is obvious that the already deposited material will undergo several thermal peaks when adding layers.

Figure 4b) illustrates the thermal cycles in the first three layers in AM of stainless steel. The first layer has three peaks, one for each layer applied. It can be observed that the main temperature peak for each deposition layer increases with the number of layers, due to the heat accumulation in the AM part.

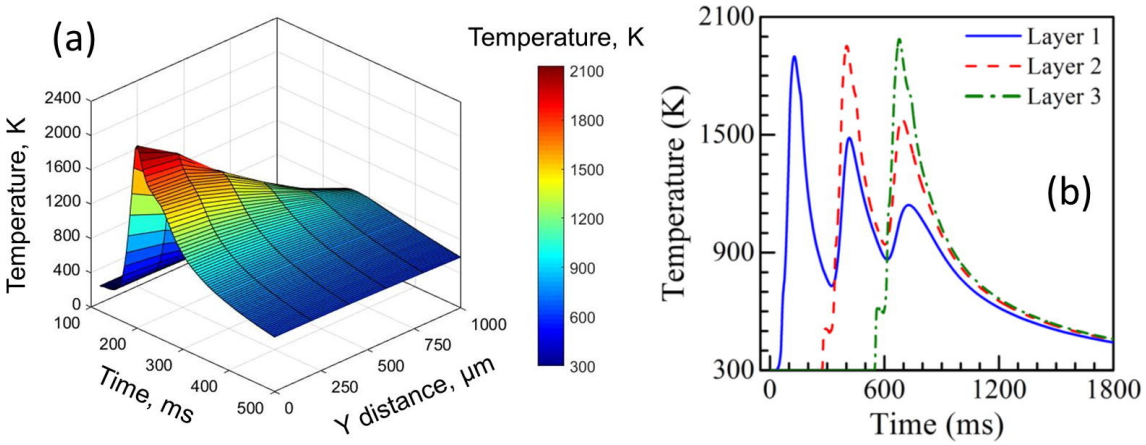

Figure 4: a) Variation of temperature with respect to time at different locations on the deposition layer surface during a single layer LMD with powder of IN718 on the IN718 surface. The laser power was 250W and the scanning speed was 15mm/s. b) Measured thermal cycles in the first three layers with DED of 316 stainless steel with a 210W laser power and a scanning speed of 12.7mm/s. From DebRoy et al. 2017, copyright 2017 by Elsevier Ltd.

Table 1: Typical cooling rates in different AM processes compared to conventional manufacturing processes (DebRoy et al. 2017).

Type of process	**Scanning speed [mm/s]**	**Cooling rate [K/s]**
Casting	-	$10^0 - 10^2$
Laser welding	-	$10^2 - 10^6$
LMD with IN718	25-40	$(5 - 30) \times 10^3$
PBF with laser of Al-alloy	100-400	$(1 - 6) \times 10^6$

2.4 Structure in AM materials

The heat sources used in both AM and welding processes are very similar. Multi-layered deposits are therefore highly related to multi-pass welds. Furthermore, many similarities can be seen in the material microstructure and texture for the two cases (DebRoy et al. 2017). However, the process methods such as scanning speeds and the layer-by-layer control are not the same, resulting in divergence in the as-deposited AM structure. Distinct research is therefore required to understand the microstructural behaviour in additive manufacturing in terms of solidification, texture, particles and mechanical properties.

2.4.1 Solidification structure

An understanding of the behaviour of the melt pool is essential to predict the grain structure and the crystallographic texture. The grains forming in the fusion zone and the local solidification rate are both influenced by the melt pool shape and size. The literature refers to two important parameters that affect the solidification structure of a solidified alloy. These are the local solidification rate R and the temperature gradient G (DebRoy et al. 2017) and depend on both the shape of the fusion zone and the temperature field. Figure 5 shows a solidification map of how different combinations of R and G give rise to different solidification structures. The ratio of G and R alters the morphology of the solidified material. As seen in the figure, a high G/R ratio gives planar or cellular grain growth, while a low G/R ratio results in a dendritic structure. By multiplying G and R, however, the cooling rate is calculated, which affects the size of the solidification structure. A high GR product means high cooling rates, which gives rise to fine solidification structures. By inducing higher heat input, which can be easily altered in AM deposition, the cooling rate will be reduced, resulting in a coarse solidification structure. For most alloys, this influences the hardness as a coarser microstructure often results in lower hardness values (DebRoy et al. 2017).

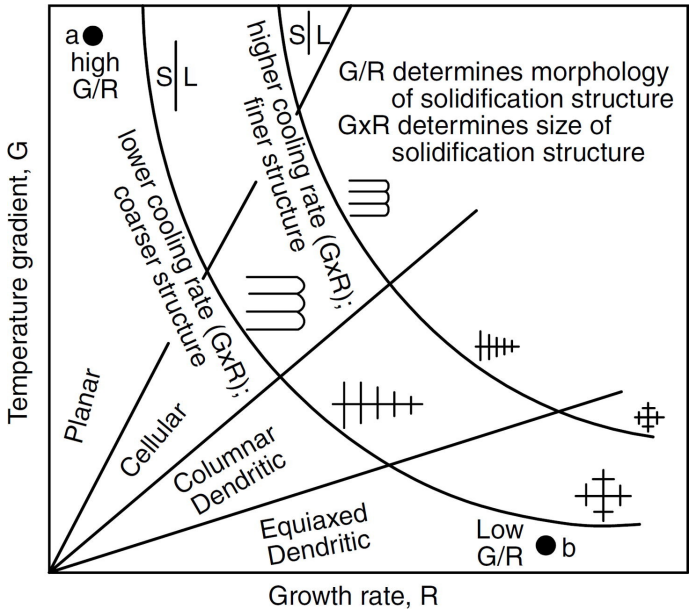

Figure 5: Solidification map where the temperature gradient, G, and the growth rate, R, influences the solidification structure. From DebRoy et al. 2017, copyright 2017 by Elsevier Ltd.

The nucleation plays an important role in layer-by-layer deposition processes. Both the number of nucleation sites and the nucleation site positions affect the solidification structure. The nucleation behaviour of the first layer is governed by the substrate material. Deposition of a material with the same chemical composition as the substrate material will not require the formation of new nucleation sites. Instead, epitaxial growth from the substrate will take place. In many cases, however, there is an advantage to using dissimilar materials. Such cases can be when using a different support structure than the deposition material, or in processes of multi-material deposition. Then, for nucleation to take place at the melt pool boundary, an energy barrier needs to be triggered that further initiates the grain growth (DebRoy et al. 2017).

In processes of multi-layer deposition, the grain growth will occur in the solidification of the previous as-deposited layer (Zhong, Gasser, Kittel et al. 2016). Due to the re-melting of preceding layers, the quality of the material will be improved. The reason for this is the breakdown of oxide films, the removal of surface contamination and the increased interlayer bondings caused by a high heat input (DebRoy et al. 2017). Within a short distance from the substrate, the microstructure of the substrate is dominating the structure of the new solidified metal. But, further away from the boundary, competitive grain growth is observed during solidification. This phenomenon is seen in polycrystalline materials, i.e. where the dendrites have various crystallographic orientations. This is described further in Section 2.4.2.

The grain solidification structure affects mainly the mechanical properties and the solidification cracking resistance of the as-deposited material. For nickel-based superalloys, both columnar, either planar, cellular or dendritic substructure and equiaxed dendritic grains are widely observed (DebRoy et al. 2017). The former grain type is in general coarse and anisotropic, while the latter is often smaller with uniform properties. Much attention has been given to the research of grain morphology, and especially anisotropy, of AM material in recent years (Zhong, Gasser, Kittel et al. 2016; Herzog et al. 2016; Popovich et al. 2017). Anisotropic properties are in most cases undesired due to mechanical weaknesses and susceptibility to solidification cracking when exposed to multi-directional stresses. Process-controlled solidification is then necessary to modify the microstructure and to achieve homogeneous material depositions. To do so, one can promote the formation of equiaxed grains by a low G/R ratio. This can be done by increasing the scanning speed. An improvement in the material ductility and toughness is then achieved, as well as in reducing the susceptibility to solidification cracking. The G/R ratio is observed to decrease in the upper deposition layers for materials with low heat conductivity due to lower temperature gradients and increased instability of the solidification interface (Manvatkar et al. 2014). Post-processing heat treatment is also a widely used method to increase the fraction of equiaxed grains in the as-deposited material.

In AM, the solidification happens in non-equilibrium conditions. Various phases appear and disappear during rapid cooling and several heat cycles. Direct observations and measurements of local cooling rates and characterization of solidification and phase transformations are therefore necessary to understand how the microstructure evolves (Herzog et al. 2016).

2.4.2 Texture

During solidification, the texture in AM depositions develops a certain way. The solidification texture is determined by the maximum heat flow directions at the boundaries of the melt pool, and the easy growth directions of the grains. As a result, there will be an alignment of dendrites during solidification (DebRoy et al. 2017). Since the competitive growth is a direct consequence of the compromise between the easy growth directions of dendrites and the maximum heat flow direction, materials with different crystal structures will have different easy growth directions (Zhong, Gasser, Kittel et al. 2016). Nickel-based superalloys have a face-centred cubic crystal structure, and thus the preferred growth direction is in the <100> direction (DebRoy et al. 2017). Among all the randomly oriented grains during solidification, the dendrites along this direction will grow faster and thus outperform the misaligned dendrites. Most commonly, a columnar dendritic structure is obtained in these cases.

A common observation in AM is a fibre texture parallel to the build direction. However, this is not entirely true. Figure 7c) and d) shows a sketch of the maximum heat flow directions and the possible primary dendrite growth directions during building, respectively. The first pattern in Figure 7d) takes only the maximum heat flow directions into consideration. This is however not favourable because the driving force for nucleation is much higher than that for grain growth. The lowest energy required for nucleation to take place is when the orientation of the new solidification pattern is perpendicular to the previous pattern. This is illustrated in Solidification pattern 2 in Figure 7d). In the boundary between each layer, epitaxial growth will take place from the secondary dendrites from the previous layer, thus minimizing the amount of energy required for nucleation. For this case, however, the deviation between grain orientation and maximum heat flow rate is 30°. This is, as well, an unrealistic option. A compromise between these two cases will therefore be an ideal solution. The primary dendrite growth direction and the maximum heat flow direction will in this case deviate 15° from the preferred directions in all layers, seen as Solidification pattern 3 in Figure 7d). By manipulating melt pool size and shape through different scanning strategies, it is possible to control the texture in the AM part. The strategies include adjustments in the process parameters that determine the re-melting of previous layers. In general, it is possible to favour epitaxial growth by ensuring the previously deposited material is sufficiently re-melted, hence giving the material a texture that increases the mechanical strength of the AM part (DebRoy et al. 2017).

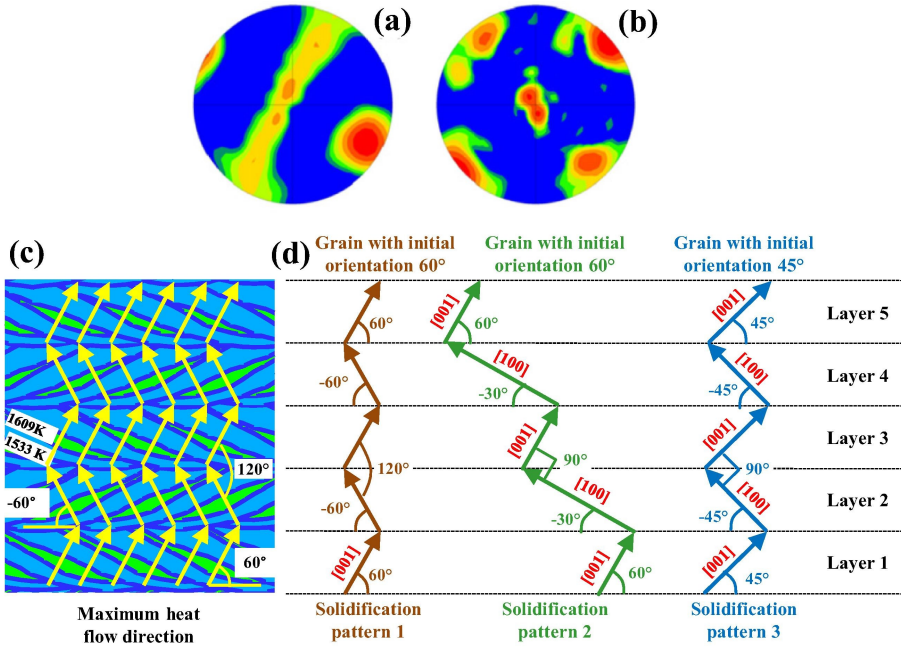

Figure 6: Texture obtained by DED with laser. Inverse pole figures of a) unidirectional and b) bidirectional scanning. From DebRoy et al. 2017, copyright 2017 by Elsevier Ltd.

The anisotropic nature of additively manufactured specimens is not ideal in high-performance parts. The material is often required to exhibit excellent mechanical properties in industrial applications. Examination of the mechanical properties of IN718 in both horizontally built (transverse) samples and vertically built (longitudinal) samples have been done (Ni et al. 2017; Strößner et al. 2015). The tendency was that the vertically built specimens showed lower tensile strength but higher fracture strain than the horizontally built specimens. This is seen in Figure 7.

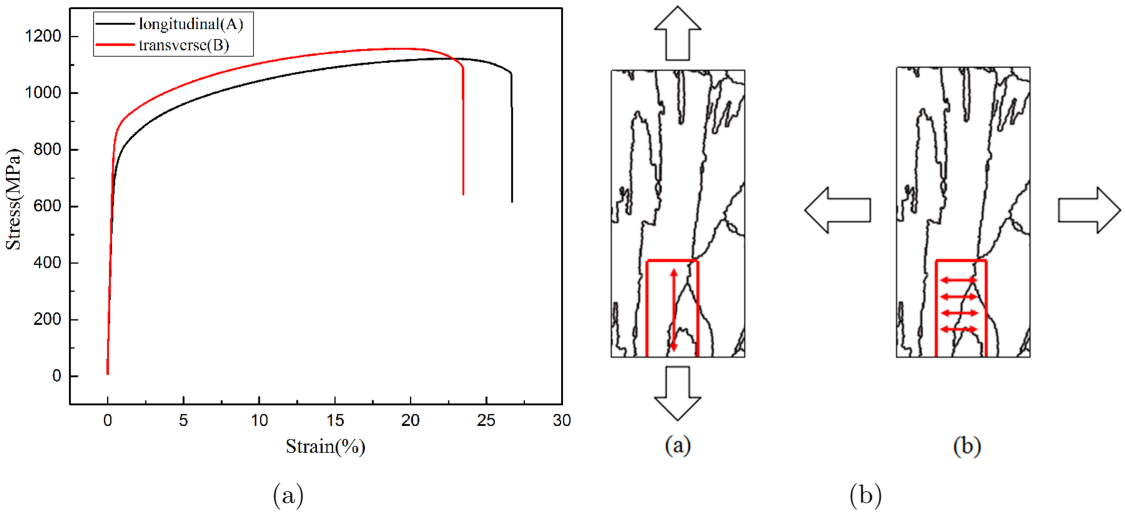

Figure 7: Mechanical properties of IN718 in transverse tensile direction and longitudinal tensile direction. The transverse built sample exhibit higher strength but lower ductility than the longitudinally built. From Ni et al. 2017, copyright 2017 by Elsevier Ltd.

2.5 Nickel Based Superalloys

Nickel is a widely used metal in technological applications because of its great properties. The FCC atomic structure gives the material high toughness and high ductility, and the combination of high corrosion resistance at high temperatures and high strength makes nickel both an appreciable base metal and an alloy component. Nickel is mostly used in machine and motor applications, as well as high-temperature environments such as rocket engines, spacecraft, petrochemical equipment and nuclear reactors (Solberg 2017). Unfortunately, due to the high prices, the area of use is limited. Cheaper alternatives are often used, but when the adequate properties of nickel are desired, there is a lack of other replacements. Therefore, companies often want to invest in highly durable and high-quality nickel alloys. These alloys may be defined as superalloys, a category of alloys with exceptionally high strength and corrosion resistance at elevated temperatures. Superalloys were first developed in the United States in the early 1930s for the production of more effective gas turbines in aeroplane engines. The alloys were either nickel-based or cobalt-based. Today, the former is most widespread as the types Inconel, Udiment, Waspaloy, Astroloy, Renè and Nimonic. Each of these has variants in terms of chemical composition and is systematized as the name followed by a number, for example, Inconel 718. Nickel-based superalloys consist of a large fraction of alloying elements, each contributing to distinct material functions. These elements can be Cr, Al, Si, C, Mn, Ti, Mo, Fe, Co, W, V, Nb and Ta. Most of them make up the chemical composition of Inconel 718, see Table 3.

The superalloys consist of both austenite formers, like Ni, and ferrite formers, such as Cr and Mo. To obtain the austenitic structure, the Ni content must not be lower than 25%. The austenite contributes to higher strength and higher oxidation resistance. Cr is present for the alloy to form a protective Cr_2O_2 layer at high temperatures and increases the high-temperature oxidation resistance of the alloy. Al also has the same property as Cr and forms oxides at high temperatures. The Fe-Cr-Ni ternary phase diagram is shown in Figure 8. Some Ni may be displaced by Fe, which is a much cheaper metal. Also, both

Fe and Mo contribute to solid solution strengthening. On the other side, the temperature resistance of Fe is lower and decreases the limiting operating temperature of the alloy. During annealing, up to around 760℃, Al and Ti form $Ni_3(Al, Ti)$ particles.

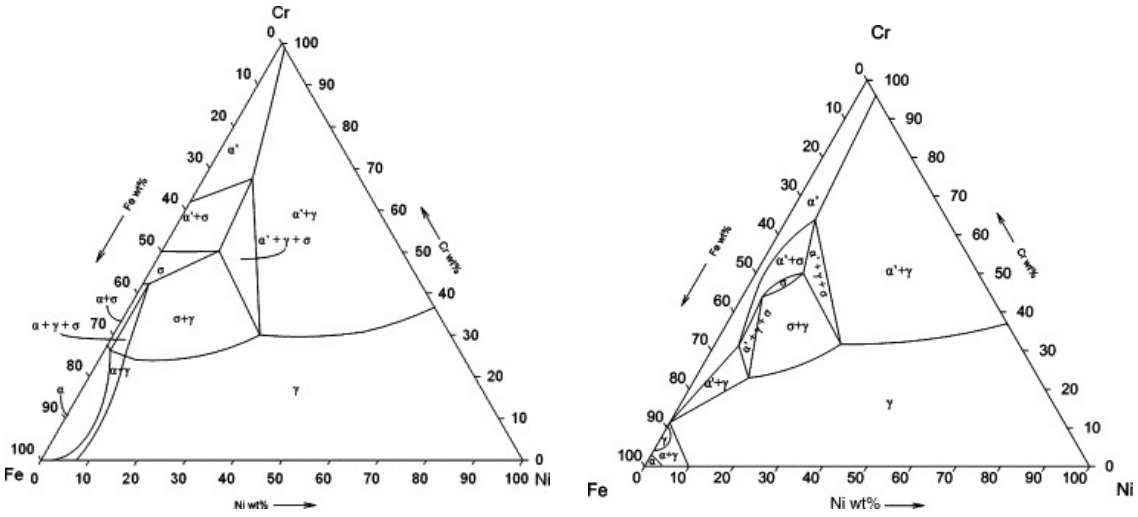

Figure 8: Ternary phase diagrams of Fe-Cr-Ni at a) 750℃ and b) 850℃. From Yen et al. 2008, copyright 2008 by Elsevier.

2.5.1 Inconel 718

Inconel 718 (IN718) is one of the most used and most important nickel-based superalloys today. A combination of high strength, high corrosion resistance up to around 700℃, high creep-rapture resistance and good weldability makes IN718 a sought-after material (Zhong, Gasser, Kittel et al. 2016). It is widely used in the spacecraft industries, more specifically in parts such as airfoils, rotating parts, supporting structures, pressure vessels, and aircraft engines. More and more attention has been given to additive manufacturing of IN718 in recent years, making high-performance parts with complex geometries on demand. Due to the high exposure to defects and poor microstructural features in the deposited material, materials with preferred mechanical properties are not easy to manufacture. In AM, the behaviour of the material during deposition and the properties of the as-deposited material is highly influenced by the physical properties of the AM material. In the case of IN718, the material has good thermal stability with high strength that is maintained at elevated temperatures, seen from Table 2. Compared to aluminium bronze, another alloy widely used in engine components with a thermal conductivity of about 70W/mK at room temperature (Engineering ToolBox 2022), the thermal conductivity of IN718 is low. This property affects how much heat the deposition material accumulates during processing. The thermal-induced stress will also be higher for low thermal conductivities, in addition to limiting processing speeds during building. However, the high viscosity of IN718 can be of advantage, offering the possibility to increase the melt pool size and thus favour laser metal deposition rather than powder bed systems (Herzog et al. 2016).

Table 2: Properties of as-built Inconel 718 (Meltio 2022b; Special Metals Corporation 2022; DebRoy et al. 2017).

Property	**Value**	**Unit**
Density	8200^a	kg/m^3
Hardness	245^b	HV30
Viscosity	5×10^{-3}	kg/ms
Melting range	1260 - 1336	℃
Yield strength	537 ± 32^c	MPa
Tensile strength	833 ± 50^c	MPa
Elongation	25 ± 3^c	%
Thermal conductivity	11 / 21^d	W/mK

[a] Annealed [b] As-built [c] Near isotropic properties [d] At 20℃/ At 650℃

Table 3: Limiting chemical composition of Inconel 718 in percent by weight [wt%] from AMS specifications (Special Metals Corporation 2022).

Element	**[wt%]**	**Element**	**[wt%]**
Nickel (Ni)	50.00 - 55.00	*Cobalt (Co)*	1.00 max.
Chromium (Cr)	17.00 - 21.00	*Manganese (Mn)*	0.35 max.
Iron (Fe)	Balance	*Silicon (Si)*	0.35 max.
Niobium & Tantalum (Nb+Ta)	4.75 - 5.50	*Copper (Cu)*	0.30 max
Molybdenum (Mo)	2.80 - 3.30	*Carbon (C)*	0.08 max.
Titanium (Ti)	0.65 - 1.15	*Phosphorous (P)*	0.015 max.
Aluminium (Al)	0.20 - 0.80	*Sulphur (S)*	0.015 max.
		Boron (B)	0.006 max.

2.5.2 Phases in IN718

Inconel 718 receives its strength from both particle/precipitation strengthening and solid solution strengthening. The microstructure is governed by the formation of particles and intermetallic compounds and is affected by both the thermal history and the chemical composition of the alloy. The equilibrium phases in IN718 includes matrix γ, γ', δ, MC, $M_{23}C_6$, M_6C and Laves (Wei et al. 2013). The γ matrix is a solid solution fcc Ni. The primary strengthening precipitates are the γ'' precipitates (Strößner et al. 2015). This is a metastable phase made up of Ni and Nb, forming fine, disk-shaped Ni_3Nb intermetallic particles with bct (DO22) crystal structure. γ' is contributing as a secondary strengthening precipitate and is observed as $Ni_3(Al, Ti)$. γ' has a cubic ordered face-centered LI2 crystal

structure, and it is less frequent than the γ'' phase (DebRoy et al. 2017). Both γ' and γ'' are coherent with the γ matrix. Thus, strain fields around the precipitates are formed, preventing dislocations from moving (Hosseini and Popovich 2019). Moreover, σ phase (CrFe) can also be appear when the material is exposed to stresses at temperatures of 700℃ over time (Strondl et al. 2008). However, this phase is not much reported in AM of IN718.

In AM, the solidification takes place in non-equilibrium conditions because of the rapid cooling of the molten pool. Unlike in cast processes, where macrosegregation of alloying elements takes place, the microstructure of an as-built AM material often consists of a supersaturated solid solution with microsegregation in the interdendritic regions. The microstructure of IN718 will is mainly a super-saturated γ solid solution, with a high fraction of Ni, Cr and Fe (Hosseini and Popovich 2019). In additive manufacturing of IN718, columnar grains are formed and aligned parallel to the build direction. Thus, a strong anisotropy is therefore observed. A dendritic structure is often easy to detect and consists of a large amount of Laves phases precipitated in the interdendritic zones, primarily because of Nb and Ti microsegregation (Liu et al. 2020; Hosseini and Popovich 2019). It is formed in Nb-rich liquid at the late stage of solidification and is reported to have a considerable influence on the microstructure as long chains of Laves phase tend to form in the interdendritic regions in IN718. The Laves phase is known as a Nb and Mo-rich intermetallic brittle phase, and it is seen to be detrimental for material ductility and strength as it acts as a crack initiator. The crack can also easily propagate with this phase present (Hosseini and Popovich 2019). The formation of this phase is dependent on the cooling rates in the material and a cooling rate experienced in LMWD is found to be low enough to promote the formation of the Lave phase (Bombach et al. 2018). It is reported that this phase decreases the mechanical properties of the AM part, where properties such as ductility, ultimate tensile strength and fracture toughness are decreased due to the formation of microscopic cracks (Zhong, Gasser, Backes et al. 2022). The formation σ phase is also observed in additively manufactured IN718 due to segregation.

There will not be enough time for γ' or γ'' to form, and for this, solution heat treatment is necessary to achieve the desired mechanical properties (Hosseini and Popovich 2019). The heat treatment involves two steps, solid solution annealing at high temperatures and age treatment at lower temperatures (Tucho et al. 2017). Undesirable phases tend to form in IN718, such as NbC, $\delta - Ni_3Nb$ (DOA) and Laves, reducing the ductility, fatigue and creep rupture strength. This is mainly because Nb is a constituent highly susceptible to segregation, thus Nb-rich phases will easily form (Tucho et al. 2017). The isothermal transformation diagram in Figure 9 shows the forming of different phases being exposed to temperatures over time. During solution heat treatment at temperatures up to around 1000℃, the Laves phase will be dissolved, and elements such as Ti and Nb will be homogeneously distributed in the γ matrix (Hosseini and Popovich 2019). This will furthermore promote the formation of fine-dispersed γ' and γ'' precipitates. However, depending on the heat treatment, γ'' can transform to incoherent δ, thus reducing the strength (Hosseini and Popovich 2019).

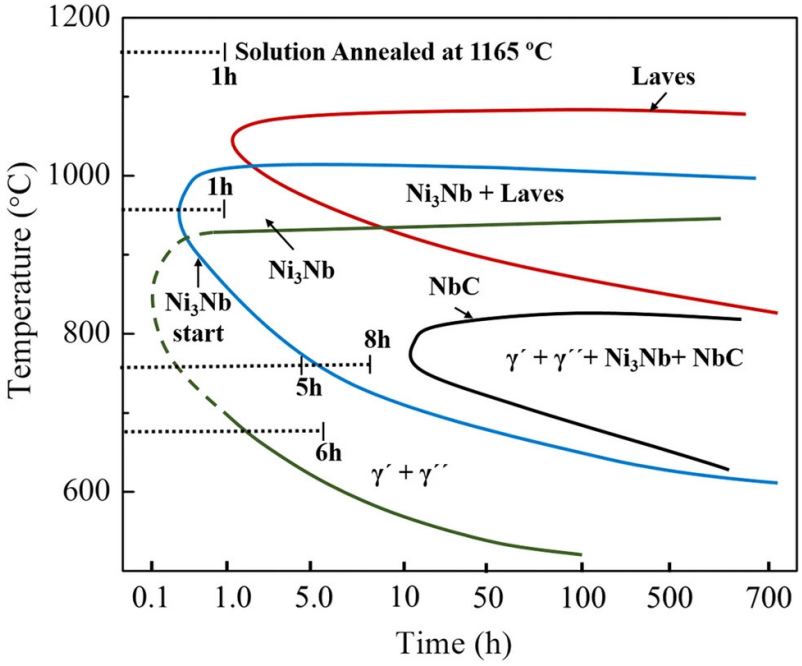

Figure 9: Time-temperature-transformation diagram of IN718. From Sahu and Bag 2021, copyright 2021 by Springer Nature.

Table 4: Phases in IN718 (Hosseini and Popovich 2019).

Phase	**Chemical symbol**	**Crystal structure**
γ	Ni-Cr(matrix)	fcc (A1)
γ'	$Ni_3(Al, Ti, Nb)$	fcc (L12)
γ''	Ni_3Nb	bct (D022)
MX	$(Nb, Ti)(C, N)$	fcc (B1)
Laves	$(Ni, Fe, Cr)_2(Nb, Mo, Ti)$	tcp (C14)
δ	$Ni_3(Nb, Ti)$	tcp (D0a)
σ	$CrFe$	tcp (D8b)

2.6 Aluminium Bronze Alloys

Aluminium bronze alloys have good mechanical properties in terms of high hardness, toughness and tensile strength, combined with high corrosion resistance and thermal conductivity (Solberg 2017). They are abrasion and fatigue resistant and form a Al_2O_3 layer at the surface which protects the metal at temperatures up to 300°C. From the binary phase diagram in Figure 10 it is seen that with an Al content of a maximum of 9.4 wt%, the Al stays in solid solution in the Cu(α) matrix. At these compositions, aluminium-bronze alloys are formed. Common alloying elements are Fe, Ni, Pb and Zn. Fe is used as a grain refiner, and Ni is contributing to higher corrosion protection and increased strength. Pb works as a lubricator through the precipitation of Pb particles, increasing

the machining properties, while Zn increases the strength and the castability. The alloys with an Al content of between 7 and 10 wt% are often used in chemical-resistant applications and in parts required to withstand high temperatures. It is reported that these alloys have a $R_{p0.2} = 150 - 465$ MPa and a $R_m = 550 - 730$, with a maximum elongation of 25-3% (Solberg 2017). The investigation of the use of aluminium bronzes in AM is still a scantily explored field, although the literature on nickel aluminium bronze is increasing in topicality.

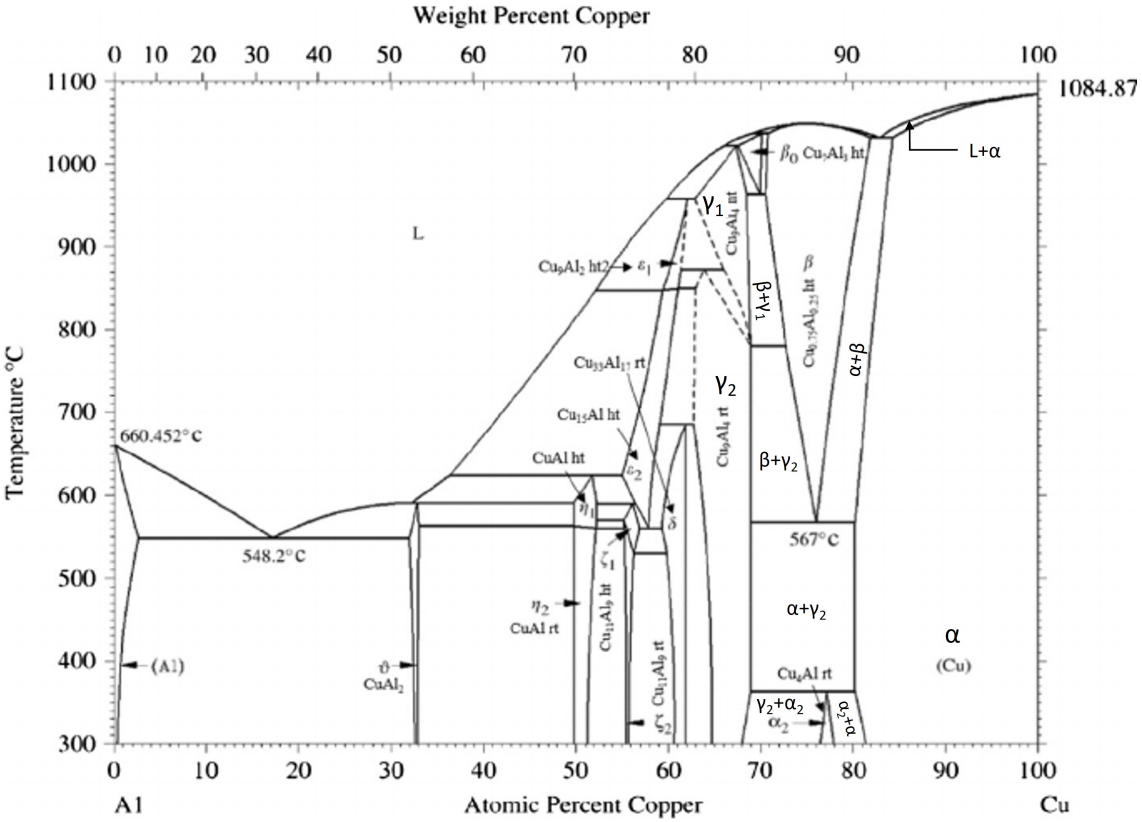

Figure 10: Al-Cu phase diagram, obtained from Kah et al. 2015. Additional phases on the Cu-rich side were named in the picture by the author.

2.6.1 CuAl7

The mechanical properties of CuAl7 are shown in Table 5, obtained from the wire producer UTP Maintenance 2023. The material exhibits high ductility performance and the strength is gained mostly from strain hardening with an increase of more than 100% from the yield strength. In Table 6 the limiting chemical composition of the alloy is listed.

Table 5: Mechanical properties of CuAl7 (UTP Maintenance 2023).

Property	**Value**	**Unit**
Hardness	120 (126)[a]	HB(HV)
Melting range	1030-1040	℃
Yield strength	180[a]	MPa
Tensile strength	400[a]	MPa
Elongation	40[a]	%

[a] *As-built*

Table 6: Limiting chemical composition of CuAl7 in percent by weight [wt%] from ISO specifications (ISO 24373 2018). (*The total of all other elements shall not exceed the value of "Others total").

Element	**[wt%]**	**Element**	**[wt%]**
Copper (Cu)	bal.	*Lead (Pb)*	0.02 max.
Aluminium (Al)	6.0-8.5	*Silicon (Si)*	0.10 max.
Iron (Fe)	*	*Zinc (Zn)*	0.20 max.
Manganese (Mn)	0.5 max.		
Nickel (Ni) incl. Co	*	*Others total**	0.50 max.

2.6.2 Phases in aluminium bronze

Aluminium bronzes with an Al content of a maximum of approximately 9wt% have an equilibrium structure of a single α phase with Al in a solid solution. The α phase has a fcc (A1) structure. Between 9 and 12wt% Al at temperatures above 567℃, a bcc (A2) β phase will form, together with α. In Kainuma et al. 2013 it is also reported of a second bcc β phase with designation B2. This is an ordered CuAl structure compared to the disordered A2 bcc Cu. Below 567℃, seen from Figure 10 and Figure 11, a eutectoid will transform from the β phase, consisting of α and γ_2. At high cooling rates, however, this decomposition will not occur. Instead, a diffusionless martensitic transformation into β' is energetically desired, with minor differences from fcc in the lattice parameter (3R, 9R, 18R or 2H crystal structure) (Orzolek et al. 2022). This is a super-saturated solid solution and a highly disordered, unstable needle-shaped phase (Hájek et al. 2016). It has a complex twin relation. The β' phase is often unwanted due to its hard and brittle nature, which reduces the ductility and increases the strength of the alloy (Sláma et al. 2014).

The presence of Ni and Fe in addition to Al results in a modified phase diagram where Ni and Fe suppress the β region. This is reported in nickel aluminium bronze (NAB) processing (Orzolek et al. 2022; Hájek et al. 2016). As Cu and Ni are neighbouring elements in the periodic table, complete miscibility is seen between them (Hou et al. 2021). The microstructure in NAB consists of an α or β' matrix and up to five different

κ particles (κ_I, κ_{II}, κ_{III}/κ_V, κ_{IV}). Fe is known as an α stabilizer, and Al and Ni are β formers. Orzolek et al. 2022 have reported that with cooling rates as of those in wire-arc DED processing, the microstructure will consist of Widmanstätten α with martensitic constituents and several κ phases. The coarsening of the microstructure will increase with decreasing cooling rates. In comparison to cast material, this microstructure results in increased yield strength and a superb enhancement in ductility. At even higher cooling rates, in laser-based or electron beam AM, the microstructure is more refined and consists of β' martensite and κ phase in the nanometer scale. In this case, the yield strength is increased considerably, but the ductility is reduced compared to cast-produced NAB.

The different κ phases in NAB are named with respect to the temperatures they are formed and the cooling rates in the material. A thorough investigation has been performed by Orzolek et al. 2022. κ_I forms at the highest temperatures, around 900°C, inside the α grains during cooling and has the chemical formula Fe_3Al. However, due to the high cooling rates, this phase is not observed in NAB alloys processed by AM. κ_{II} also has a Fe_3Al stoichiometry, but can also contain Cu, Ni and Mn, with a BiF3 (DO3) crystal structure. The nucleation is present on the boundary of the prior β phase in alloys with a low Fe content (up to 5wt%). Orzolek et al. 2022 reported the presence of the κ_{II} phase in AM processes due to the thermal cycles associated with multi-pass welding. From Dharmendra et al. 2021, κ_{II} is observed as globular Fe_3Al. For LMWD, with even higher cooling rates, nanoscale κ_{III}/κ_V and κ_{IV} are observed within the martensitic plates. κ_{III}/κ_V are Ni-rich $NiAl$ intermetallic phases, including fractions of Cu, Ni and Mn, with a CsCl (B2) crystal structure (Orzolek et al. 2022). κ_{III} is seen to have a lamellar structure, while κ_V is more needle-like (Dharmendra et al. 2021). κ_{IV} are fine Fe-rich Fe_3Al particles and nucleates in the centre of the α grains.

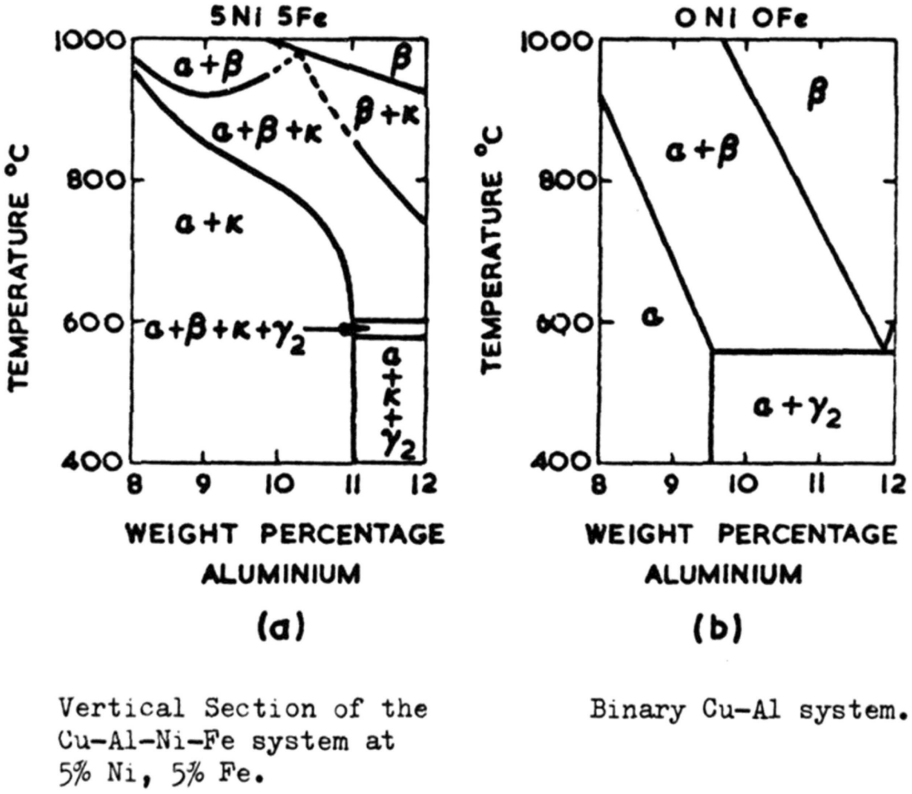

Figure 11: Phase diagram of the Cu-Al-Ni-Fe system with 5% Ni and 5% Fe (a) and the Cu-Al system (b). From Orzolek et al. 2022, copyright 2022 by Elsevier.

Table 7: Phases in NAB (Sláma et al. 2014; Orzolek et al. 2022).

Phase	**Chemical symbol**	**Crystal structure**
α	Matrix	fcc (A1)
β	Matrix	bcc (A2)
γ_2	Cu_9Al_4	P-43m
β'	Matrix	fcc' (3R, 9R, etc.)
κ_I	Fe_3Al	D03
κ_{II}	Fe_3Al	BiF3 (DO3)
κ_{III}/κ_V	$NiAl$	CsCl (B2)
κ_{IV}	Fe_3Al	bcc

3 Theory

3.1 Stress and strain

3.1.1 Stress

For a bar subjected to an axial tensile load, F, a free body diagram can be sketched as in Figure 12.

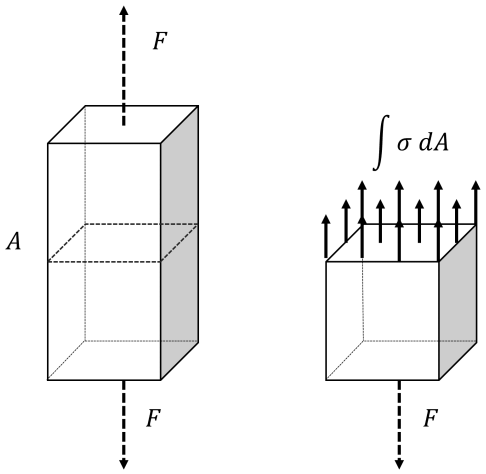

Figure 12: Free body diagram of a bar subjected to axial tensile load.

The bar has a cross-section area, A, where the normal stress component is found. The total stress working on A, $\int \sigma dA$, inside the material must balance the applied external load, F (Dieter 1988). With a uniformly distributed stress, the true stress is defined as:

$$\sigma = \frac{F}{A} \tag{1}$$

The area in Equation 1 depends on the deformation of the bar. However, a more common method of measuring the stress is to only use the area before deformation, A_0. This yields the equation for the engineering stress (nominal stress):

$$s = \frac{F}{A_0} \tag{2}$$

In the rest of the report, s and σ are used for engineering/nominal stress and true stress, respectively.

3.1.2 Strain

Strain is the amount of deformation in a material, and is defined as the ratio between the change in length and the original length in a tensile test (Equation 3). The average linear engineering strain is thus:

$$e = \frac{\delta L}{L_0} = \frac{L - L_0}{L_0} = \frac{L}{L_0} - 1 \tag{3}$$

L_0 is the initial length between two gauge marks on the surface of the undeformed tensile specimen and L is the length measured instantaneously between these two marks as the material is deformed. For measuring L, an extensometer is used to track the length between the marks.

As the dimensions of the specimen will change continuously during the tensile test, the engineering strain will not represent the true deformation characteristics. For each increase in length, the new length must be used to calculate the instantaneous strain. Hence, the definition of true strain can be represented as in Equation 4.

$$\varepsilon = \int_{L_0}^{L} \frac{dL}{L} = \ln \frac{L}{L_0} \tag{4}$$

3.1.3 Stress-strain relationship

Equations relating engineering stress to true stress, and engineering strain and true strain can be defined. By assuming volume conservation and uniform deformation (Equation 5), one can arrive at Equation 6 and Equation 7.

$$V = A_0 L_0 = AL \implies \frac{L}{L_0} = \frac{A_0}{A} \tag{5}$$

$$\sigma = s(1 + e) \tag{6}$$

$$\varepsilon = \ln(1 + e) \tag{7}$$

3.1.4 Ductility measures

To investigate the ductility of a material, two material properties are of interest (Ohring 1995). Fracture strain is based on specimen elongation and the reduction of the area until failure builds on the decrease in the cross-section area. The true strain at fracture, ε_f, is found by implementing the area of fraction in Equation 4, using the constancy-of-volume assumption (Equation 5).

$$\varepsilon_f = ln\left(\frac{A_0}{A_f}\right) \tag{8}$$

The reduction of the area until fracture is found by dividing the decrease in the area by the original cross-section area:

$$q = \frac{A_0 - A_f}{A_0} \tag{9}$$

3.2 Dislocation movement

A dislocation is known as the most important line defect in crystal structures and is responsible for the slip phenomenon resulting in plastic deformation. Dislocation theory can be used to understand the plastic deformations and the strengthening mechanisms present in polycrystalline solids (Dieter 1988).

The two simplest forms of dislocations are edge dislocation and screw dislocation (Dieter 1988). An edge dislocation is illustrated in Figure 13 with the symbol $\perp$. The atoms around the simple cubic lattice are displaced around the dislocation, where an extra plane of atoms is inserted. It results in a stress field around the dislocation, with compressive stress above the line defect and tensile stress below. The displacement is equal to the Burgers vector, b, which is always perpendicular to the dislocation line. When shear stress (τ) is applied to the crystal, the dislocation glides in the slip plane, perpendicular to its length.

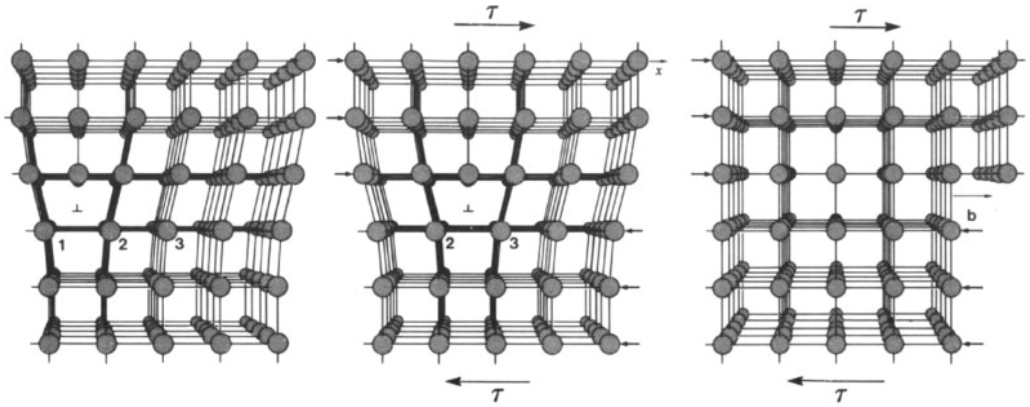

Figure 13: Movement of an edge dislocation along the slip plane. Obtained from Ohring 1995.

Edge dislocations may also climb by moving vertically, normal to the slip plane. This can happen if there is a lattice vacancy near the dislocation line, to where atoms can diffuse (Dieter 1988). Alternatively, a negative climb may take place, where an atom from the lattice planes around the extra plane is added to the dislocation spot. The climb phenomenon is diffusion controlled and is thus a slower process than gliding at low temperatures.

In screw dislocation, the crystal structure above the slip plane is dislocated along the slip plane parallel to the Burgers vector (Dieter 1988). In contrast to an edge dislocation, a screw dislocation does not have a preferred slip plane. This makes the motion of screw dislocations less limited.

Deformation by slip occurs most readily in the distinct slip planes, the crystallographic planes, along the closest-packed direction of atoms (Dieter 1988). The reason for this is the low resistance to slip due to the large distance between the high atomic density planes. The slip systems will then consist of both the slip planes and the slip directions. Few slip systems result in an extreme orientation dependence and thus low material ductility. This applies to hcp structures, for instance, containing only three slip systems. However, fcc crystal structures contain 12 possible slip systems, making crystal structures of Cu, Ni and Al more susceptible to slip. The bcc crystal contains in total 48 different slip systems,

but these structures do not have as closed-packed planes as the fcc structure, requiring increased shear stresses for a slip to take place. Because of the high symmetry of fcc crystals, and thus the wide range of available slip systems, the slip plane slip system requires minimal rotation before the resolved shear stress reaches a high level on an alternative {111}<110> slip system (Dieter 1988). Duplex slip occurs when the resolved shear stress on the primary slip system is equal to that of the conjugate slip system (-1-11)[001]. This phenomenon leads to a simultaneous deformation in both slip systems, and furthermore, a significant strain hardening due to the interactions between two slip system dislocations.

3.3 Strengthening mechanisms

The strength of a metal is governed by many factors. It is inversely related to the dislocation mobility, and dependent on the crystal structure, the stacking-fault energy, the dislocation density and lattice friction stress (Peierls stress). The strengthening mechanisms in a polycrystalline metal are given by Equation 10, assuming the different stress contributions can be added independently (Holmedal 2021). The different contributions are from grain boundaries (σ_{GB}), deformation hardening (σ_ρ), solid solution strengthening (σ_{SS}) and particle hardening (σ_P). A polycrystalline aggregate consists of individual grains, and these grains will influence each other by restraining effects, giving the material other properties than that for single crystals. It is challenging to do predictions of high precision on the material strength due to the high complexity of the contributions involved.

$$\sigma = \sigma_{GB} + \sigma_\rho + \sigma_{SS} + \sigma_P + ... \tag{10}$$

3.3.1 Grain boundaries

Grain boundaries are the region between neighbouring crystal lattices with misfits in the crystallographic orientation represented by a misorientation angle (Dieter 1988), and act like surface or area defects (Ohring 1995). Grain boundaries contain non-mobile dislocations, forming grain-boundary ledges, and acting as effective sources of dislocations. Due to their high surface energy, grain boundaries are preferred locations for solid-state reactions to take place, thus facilitating reactions such as the segregation of solute atoms. More slip systems are often active within a short distance from the grain boundaries, leading to higher hardness near the grain boundaries compared to the grain centre. Reducing the grain size will therefore increase the strain hardening and the overall strength of the polycrystalline material.

Hall and Petch deduced an equation for a general relationship between yield stress, σ_y, and grain diameter, D, given in Equation 11 (Dieter 1988). σ_0 is the friction stress or the total resistance for dislocation in the crystal lattice to move, while k is the relative hardening contribution of the grain boundaries. The Hall-Petch equation is based on the movement of slip dislocation inside each grain until they pile up by the grain boundary, working as a barrier the dislocations must exceed. The pile-up mechanism of dislocations is illustrated in Figure 14. This requires a certain critical shear stress.

$$\sigma_y = \sigma_0 + \frac{k_y}{\sqrt{D}} \tag{11}$$

In addition to high-angle grain boundaries, substructures also exist with low-angle boundaries (Dieter 1988). These have a misorientation of only a few degrees and have lower energies than ordinary grain boundaries. Arrays of edge dislocations are present in these boundaries due to the semi-correspondent crystal lattice. Crystal growth and phase transformation can both facilitate the formation of subgrains. It is observed that subboundary-containing steels have higher tensile strength than steels not containing subgrains, while the ductility almost is the same for both materials.

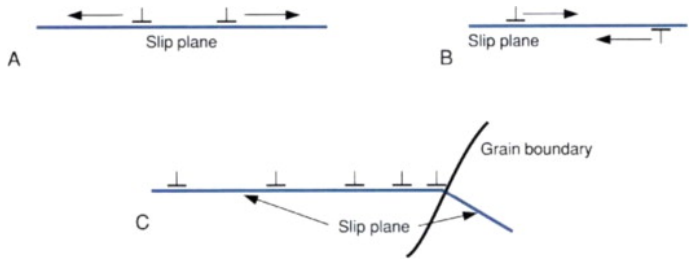

Figure 14: Dislocation pile-up mechanism by grain boundary. Obtained from Ohring 1995.

3.3.2 Deformation hardening

Deformation hardening or strain hardening is a mechanism in metals where the stress required to produce slip increases due to previous plastic deformation (Dieter 1988). Strain hardening is often observed during tensile testing and in many industrial processes. It is defined as the slope of the true stress-strain curve, $\frac{d\sigma}{d\varepsilon}$. The process causes a reorientation and elongation of grains in the direction of working, and the strain hardening of solid-solution is almost always higher than strain hardened pure metal. As the metal starts to deform plastically subsequent to the yield point, a nearly linear part of the stress-strain curve can be observed with a large slope. The stress contribution comes from slip on several slip systems, the formation of lattice irregularities and the pile-up of dislocations. After a certain amount of strain is performed, the strain hardening decreases, called dynamic recovery. At these stresses, the piled-up dislocations can be released and thus reduce the strain field created by cross slip, a process where a screw dislocation starts gliding on another slip plane with the same Burgers vector as the previous slip plane (Bonneville and Escaig 1979).

3.3.3 Solid solution strengthening

A solid solution is a solvent-atom lattice containing solute atoms, either substitutionally or interstitially. The former type is present when the solvent atoms occupy solvent atom sites, having almost the same atom size, while the latter type is caused by solute atoms, much smaller than the solvent atoms, occupying interstitial sites between the atoms in the solvent lattice. The chemical affinity between two metals determines whether the alloy forms a solid solution or not. A strong affinity will favour solid solution, while intermetallic compounds often form for low affinity-related metals. Another important factor is the relative valence between the metals. Copper, for instance, is less soluble in zinc than the opposite. Some metals are soluble in all compositions, e.g. Cu-Ni (Villars and Okamoto n.d.). Because of both the atom size differences and the electronic characters, there will be interactions between dislocations (Ohring 1995). The mismatch of a solute atom in the parent lattice will create a stress field, reducing the dislocation movement ability.

Dissolving solute atoms in a host metal to form a solid solution is therefore an effective way to strengthen the metal. However, other properties may be altered by this action. Strengthening Cu, for instance, will reduce the electrical and thermal conductivity and the trade-off value must therefore be considered for each application (Ohring 1995).

3.3.4 Particle hardening

Particle or precipitation hardening is a heat treatment technique which results in further strengthening of the alloy subsequent to forming (Ohring 1995). This requires a rapid increase in solid-state solubility limits with increasing temperature. By quenching an alloy from its high-temperature solid solution state, a single-phase region in the phase diagram, the solid solution will become super-saturated in which solute atoms are frozen. Subsequently, controlled nucleation and growth of rejected particles or precipitates can be attained. The strengthening distribution arises from the interaction between the precipitates and the dislocations present in the matrix. The interaction between an impenetrable particle and the edge dislocation can be of various types (Groh 2014). Figure 15 shows the simplest form of interaction is the Orowan mechanism, where a glide dislocation bypasses an impenetrable particle leaving behind a shear loop around the particles. These have Burgers vectors in the glide plane. In addition, prismatic deformation loops can form, with the Burgers vector not lying in the plane of the loop. It is reported from Munday et al. 2016 that the formation of prismatic deformation loops is the primary mechanism for void growth during plastic deformation. A high density of particles in the matrix will be an inhibitor to dislocation movement, as the dislocations behave as obstacles requiring higher stress for the dislocation to proceed, as illustrated in Figure 15. A shear stress τ is responsible for the dislocation motion through the interparticle spacing, l. Since the particles prevent the dislocation from easily moving forward, dislocation loops are formed. This requires additional stress resulting in shear stress inversely proportionally to the interparticle spacing.

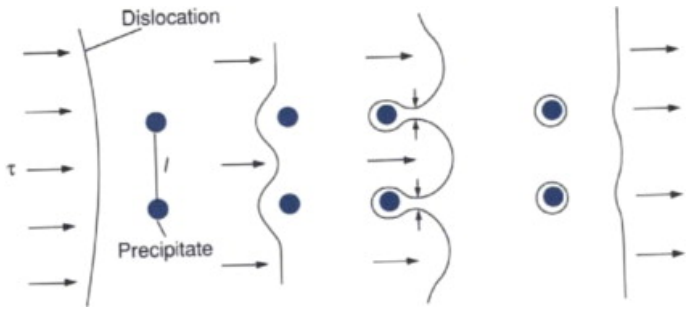

Figure 15: Particles as a strengthening mechanism, preventing dislocation movement. Obtained from Ohring 1995.

The extent of the precipitation hardening is also dependent on the precipitation size. Large second-phase particles often have low atomic matching, or coherency, with the matrix as the crystal structures do not relate, performing less resistance to dislocation motion. Small precipitates, however, have a high coherency with the matrix where a stress field is obtained around the particle, called Gunier-Preston (GP) zones (Ohring 1995). This will effectively retard the dislocation movement.

3.3.5 Twinning

Twinning is important in the understanding of the deformation of metals. Twinning occurs when a fraction of a crystal undergoes a coordinated shear displacement in the twin direction related to the orientation of the remaining untwinned lattice, forming a twinning plane (Ohring 1995). This relationship exhibits a definite and symmetrical pattern, and the twinning direction occurs in a specific crystallographic plane for each type of crystal structure (Dieter 1988). For fcc, the twin plane and the twin direction are (111) and [112], respectively. Two twinning planes divide the crystal with a twinned portion, seen as a mirror image of the original crystal. This is illustrated in Figure 16, where the lattice structure is oriented at an angle to the parent lattice (white dots). Black dots represent the real atom structure subject to twinning and it is seen from the figure that the atom movement from the original lattice increases with distance from the twinning plane. However, the distance does not exceed the inter-atom distance in the lattice (a). The orientation of the twinning plane is perpendicular to the paper, while the twin is oriented at an angle to the perfect lattice. The slip step is possible to polish away, but the twin planes cannot be eliminated due to the penetration in the bulk material (Ohring 1995). Since the lattice right to the twinning plane has a mismatch with the original plane, this region is said to be deformed. The twin obtains a different crystallographic orientation compared to the around lattice, thus making it possible to see the twin on a polished surface (Dieter 1988).

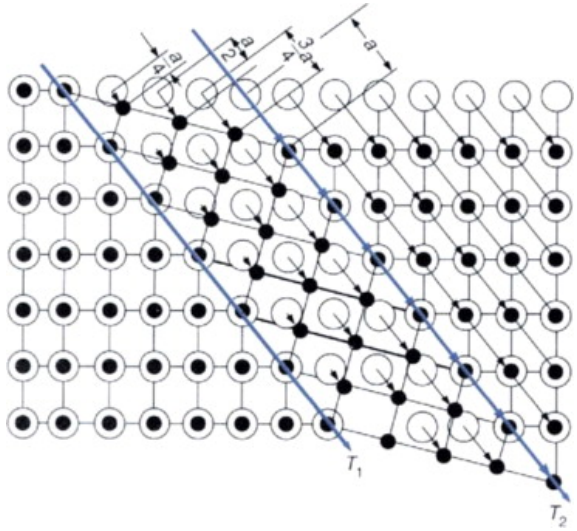

Figure 16: Twinning mechanism in crystal matrix. Obtained from Ohring 1995.

Slip dislocations are favoured by twinning because of the new slip systems created and thus the larger amounts of possible deformations with respect to the stress axis. However, the activation energy or the stress level for each mechanism determines the type of deformation the metal will be subjected to (Ohring 1995). The inherent properties such as crystal structure and number of independent slip systems, in addition to environmental factors like temperature and impurities, are all influencing which mechanism that activates. The twin boundary which separates the two crystallographic orientations can act as a barrier to dislocation movement across the boundary, impeding the dislocation motion as in Figure 14, and thus strengthening the metal through strain hardening and increasing the ductility (J. Wang and Zhang 2016). The time it takes for a slip band to form is reported to be several milliseconds, while twins can form just in a few microseconds. In

fcc crystal structures, mechanical twinning, produced by loading, is not very common due to the low stress required for a slip dislocation to occur, while both bcc and hcp favour mechanical twinning at low temperatures. Nevertheless, twins are observed in fcc metals such as copper and brass, not due to mechanical deformation, but from plastic deformation subsequent to heating or annealing (Dieter 1988; Ohring 1995). These twins are called annealing twins. Compared to mechanical twins, they are often wider with straighter sides and are often formed from mechanical twin nuclei prior to deformation.

3.4 Mechanical properties of AM materials

The microstructure in the as-deposited material controls the properties and the reliability of AM parts. An acceptable AM process in the industry would therefore be the production of a desired defect-free microstructure that satisfies the required service-oriented mechanical properties. Both microstructural and mechanical features need to be investigated and compared in order to approve the feasibility of a particular AM process.

3.4.1 Uniaxial tensile testing

The tensile test is a fundamental mechanical test method in material science and engineering, where the material is pulled at a constant pulling rate until failure. The test measures the force and the extension of the specimen. Often a stress-strain curve is plotted and gives an understanding of the response from the material during increased tension. The test is used for the determination of mechanical properties such as yield strength, ultimate tensile strength, fracture strain and reduction of area.

Stress and strain measurement
The stress and strain are measured using an extensometer which detects the distance between two points on the tensile specimen, as explained in Section 3.1.2. Figure 17 shows a characteristic stress-strain curve, both true (a) and nominal (b), for a typical engineering alloy. Point A represent the initiation of tension. The material behaves elastically between A and B (linear elastic region), but as point B is exceeded the material starts to deform plastically.

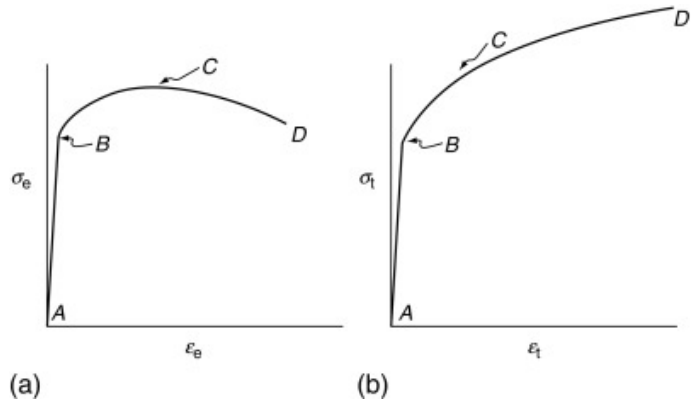

Figure 17: Characteristic a) nominal and b) true stress-strain curves. Obtained from Wright 2016.

Work hardening
Point B is referred to as the yield strength and is the same point for both true and nominal curves. The region between B and C is the strain hardening region where the material is plastically deformed. The maximum stress is the ultimate tensile stress represented by point C. As the cross-sectional area has decreased uniformly with strain up to point C, the true stress is longer equal to the nominal stress.

Necking
Between C and D, necking occurs. It initiates from a local cross-sectional area which is smaller than the uniform cross-sectional area, and as the stress concentration becomes higher in smaller areas the necking proceeds at an increasing rate. The strain hardening still continues at this stage, as seen from the true stress-strain curve (b), but the nominal stress-strain does not consider the local divergence in the cross-sectional area in the neck, thus the stress decreases rapidly. This is seen from Figure 18, where a large gauge length (L_0) results in low detected elongation from the extensometer and a small gauge length, i.e. in the neck, gives increased elongation.

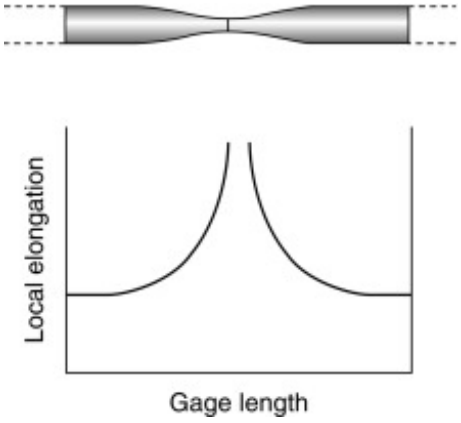

Figure 18: Measured elongation from different gauge lengths at necking. Obtained from Wright 2016.

Fracture
Necking ends up with a fracture. By measuring the fracture area both the fracture strain and the reduction of area can be calculated as described in Section 3.1.4.

3.4.2 Vickers Hardness Test

The hardness test is the most utilized mechanical test (Ohring 1995). Hardness is related to the strength of the forces in the interatomic bindings, where a high hardness indicates strong bonding. The property is useful in the estimation of the tensile strength, through the empirical relationship:

$$H \approx \frac{c}{s} \tag{12}$$

where s is the strength and c is the constant of proportionality. s can be either the yield strength or the ultimate tensile strength, dependent on the material properties and what relation one seeks. c is typical between 2 and 4 using s_u. There are several types of hardness tests, but in this thesis, only Vickers Hardness Test is used (Figure 19). This is performed by pressing a diamond indenter, a loaded and specifically dimensioned object,

into the surface of the material of interest over a given time interval (ISO 6507 2018; ASTM E384 2017).

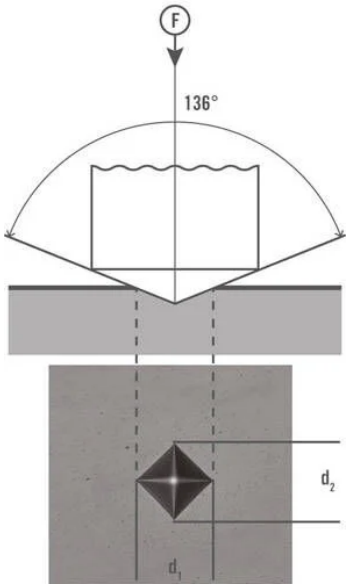

Figure 19: Illustration of Vickers hardness testing. The size of the indent is measured to calculate the HV value from Equation 13. Obtained from ZwickRoell 2023.

In the Vickers hardness test, the hardness is determined by measuring the average diagonal length of the impression left by the indenter, d, and the load, F:

$$HV = 0.102 \times \frac{2Fsin(\frac{136°}{2})}{d^2} \approx 0.1891 \times \frac{F}{d^2} \tag{13}$$

Furthermore, the microhardness test can be used to measure the hardness in small areas of the specimen surface, using the same principle as for the macrohardness test, only with smaller indenters and loads.

3.5 Material characterization

Material characterization is central for evaluating AM processes. In this thesis, the object was to analyse the interface properties in the multi-material deposition. Mechanical testing was performed in different areas of the material and intermetallic phases were examined.

3.5.1 Light optical microscopy (LOM)

A reflected light microscope, or metallurgical microscope, is a popular instrument among metallographers when examining metallic samples. Figure 20 illustrates the instrument and its interior with descriptions. The instrument is easy to use and provides several imaging techniques such as bright field, dark field and polarized light. A magnification range of, most commonly, 100x can be used, revealing details in the microscale. The focal length is limited, thus requiring the specimen surface facing the objective to be perfectly flat (Rottenfusser et al. 2022).

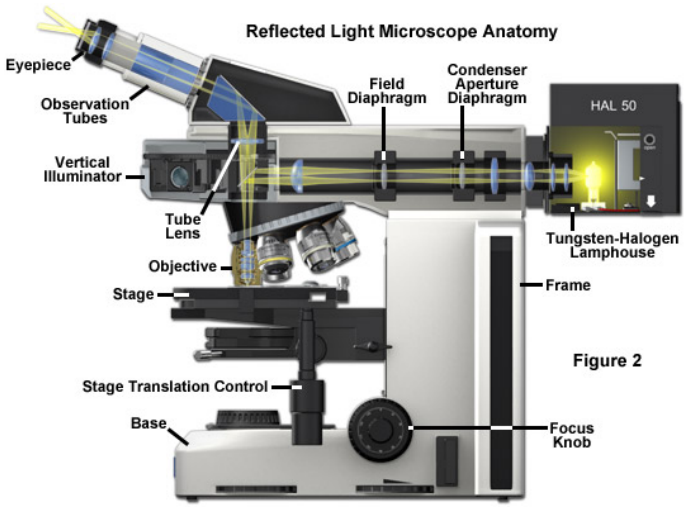

Figure 20: Anatomy of the reflected light optical microscope. Obtained from Rottenfusser et al. 2022).

3.5.2 Scanning Electron Microscopy (SEM)

In this thesis, SEM is used to do characterization regarding microstructural morphology and chemical composition in the interface region of the two alloys deposited by AM. SEM is known as one of the most versatile instruments available for investigation of this matter (Zhou et al. 2006). A typical SEM build-up is shown in Figure 21, together with the detectable signals from the sample. The specimen of investigation is mounted on a movable stage, where the specimen surface is subject to a focused electron beam emitted by an electron gun. Inside the electron column, there is a vacuum and several electromagnetic lenses guide the beam to form a controlled incident beam. An interaction volume is created when the electrons collide with the atoms on the sample surface, which generates various forms of detectable radiation. Those can be secondary electrons (SE), backscatter electrons (BSE) and other components such as X-rays and auger electrons. By analysing the different types of radiations separately, one can collect information about the material properties in the sample (Sutton et al. 2007).

Different radiation has different energy levels. Secondary electrons are electrons with low energy, resulting from high energy losses inside the specimen. They reappear from the sample surface containing information about the surface topography. Backscattered electrons, however, have an energy of 50eV or higher, and are defined as the high-energy electrons escaping from the material. The reason for the high energy is due to the elastic scattering of electrons by the atoms in the sample, thus the electrons have a low energy loss. In compositional contrast, or Z-contrast, the amount of BSE collected from the incident beam depends on the atomic number, Z, in the material. This is because of the different charging in the atoms, making it easier or harder for the incident electrons to be repelled or elastically scattered. Another type of contrast using BSE is known as orientation contrast. Due to differences in the crystallographic orientation of the grains, the channelling of electrons will vary. Thus, the signal received from each grain is dependent on the crystal structure (Sutton et al. 2007). As BSE also contains information about the topography of the sample surface, this signal is valuable in the analysis of chemical properties as well as surface features.

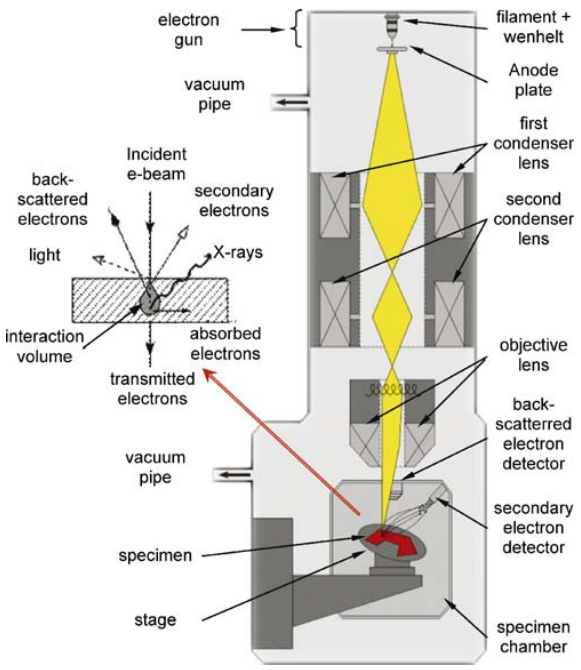

Figure 21: Schematic of a typical scanning electron microscope. The incident beam interferes with the sample interaction volume from which different signals are generated. From Sutton et al. 2007, copyright 2007 by Springer Nature.

Energy dispersive spectroscopy

Energy-dispersive spectroscopy (EDS) detects X-rays radiated from the sample material and is used to perform chemical characterization or elemental analysis of materials. When the electron beam hits the sample, the high-energy electrons interact with the atoms in the material, transferring energy (Hjelen 1986). Some of the energy is absorbed by displacing electrons from their respective shells, thus exciting the atoms. This results in the formation of voids in the electron shells. The electrons from higher energy levels will subsequently travel closer to the atom nucleus to fill the voids for the atoms to retrieve to the ground state. Photons with energies equal to the distance to the lower level shell will then be emitted, maintaining the energy balance in the atom. This is shown in Figure 22.

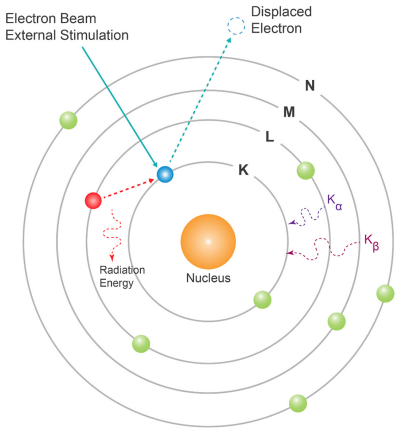

Figure 22: Schematic of an excited atom. Emitted X-rays can be detected to reveal the chemical composition of the specimen. Obtained from Particle Technology Labs 2023.

Different atoms have distinct energy levels, and hence characteristic photons are emitted, which makes it possible to discover the chemistry of the sample using EDS (Hjelen 1986). The method assembles an intensity spectre with intensity peaks, from which the identification of the elements present, known as qualitative analysis, can be performed.

Quantitative analysis can also be performed using the ZAF method in EDS (Hjelen 1986). This method relies on a comparison between the sample and a standard, where the ratio of the element concentration of the two specimens is equal to the ratio between the measured intensity of the element from the two specimens. If the standard is a pure element ($C_{(i)} = 100\%$), then

$$C_i = C_{(i)} \frac{I_i}{I_{(i)}} = (ZAF)_i \frac{I_i}{I_{(i)}} \tag{14}$$

$I_{(i)}$ is the measured intensity from the element in the reference, and I_i is the measured intensity from the element in the sample. Three correction factors are implemented to improve the accuracy. Z is the atomic number factor, A is the absorption factor, and F is the fluorescence factor (Hjelen 1986). The quantitative analysis is implemented in the software used for EDS and is subsequently calculated automatically.

Electron backscatter diffraction pattern

Electron backscatter diffraction pattern (EBSD) is a method used to measure the orientation of single grains in a polycrystalline material (Gottstein 2004. The microtexture can only be measured by inspecting very small areas, and for this, SEM with advanced EBSD equipment and software are used. Furthermore, EBSD offers orientation imaging microscopy (OIM), from which orientation maps can be obtained.

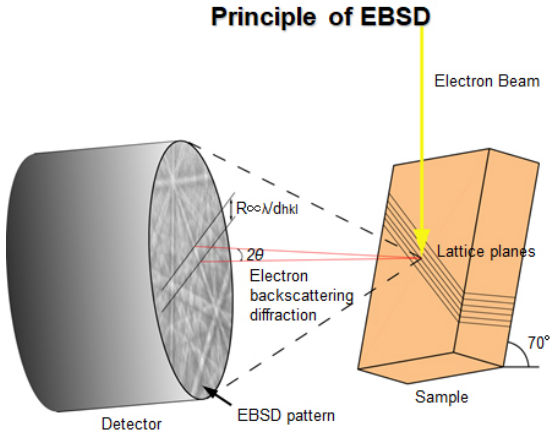

Figure 23: Illustration of the EBSD technique. The incident beam interacts with the lattice planes in the 70° tilted specimen, forming a diffraction pattern on the EBSD detector. Obtained from Toray Research Center 2023.

The principal of EBSD is shown in Figure 23. When the incident electron beam hits the 70° tilted sample inside the SEM vacuum chamber, some of the electrons will be elastically scattered as backscattered electrons. As they leave the sample surface, they will interact with the crystallographic planes satisfying Bragg's law (Gottstein 2004) and create Kikuchi bands on the phosphor screen, which convert the electron signal to light. The bands represent the lattice planes in the respective crystal structure, while the width of the bands has a Bragg's law relation. With this information in hand, it is possible to uncover the orientation of the crystal.

3.6 Summary of the essentials from the author's project work

In the aim to obtain defect-free AM parts, a suitable parameter set is required in the deposition of each distinct alloy. Due to the challenges involved in achieving this, thorough experimental work has to be done starting from single-bead deposition on the substrate and proceeding to multi-layer depositions. In the author's project work (Aas 2022), a series of different parameter configurations were looked at in order to find the optimal parameter combination in the deposition of IN718. The parameters to be investigated were traverse speed, v_t, laser power, P, wire feed rate, v_w, and hot-wire power, P_w. Also, laser focal position, Z, hatch spacing, d, and activation of base plate cooling were alternated to produce the best possible deposition part. Due to the accumulation of heat with increasing building height, both laser power and wire feed rate were adjusted to lower values during manufacturing as the as-deposited part became higher. This resulted in a clean deposition with few defects, seen from the bulk deposition material in Figure 24. The conclusion on the suitable parameter settings for IN718 from the parametric study is shown in Table 8. The microstructural features of the as-deposited part were also investigated using scanning electron microscopy (SEM), shown in Figure 25. An alignment of dendritic structure in IN718 was observed, including intermetallic regions in the interdendritic zones, indicating anisotropic mechanical properties.

Table 8: Optimized process parameter combinations for a 30-layered IN718 deposition with active base plate cooling from author's project work (Aas 2022).

Layer	P[W]	v_t[mm/s]	v_w[mm/s]	P_w[W]	Z[mm]	d[mm]
1-4	1100	10	12	250	-0.5	1.2
5-12	900	10	12	250	-0.5	1.2
12-16	800	10	11	250	-0.5	1.2
16-30	700	10	10	250	-0.5	1.2

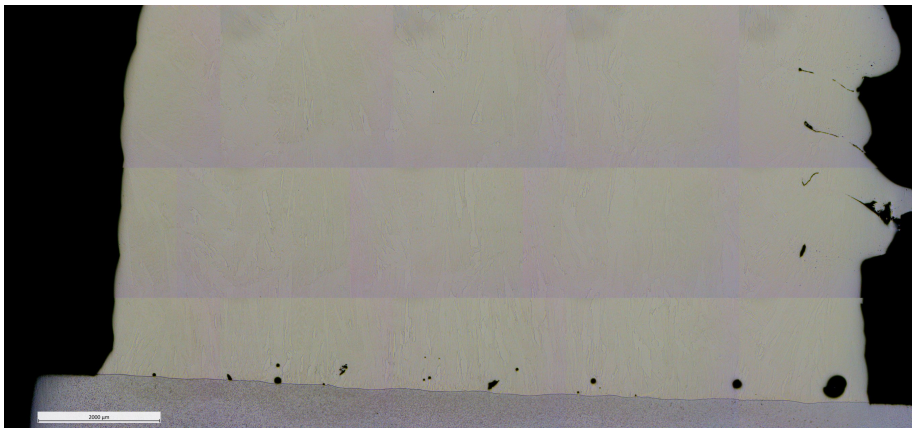

Figure 24: LOM image of IN718 deposited on a carbon steel substrate. Obtained from author's project work (Aas 2022).

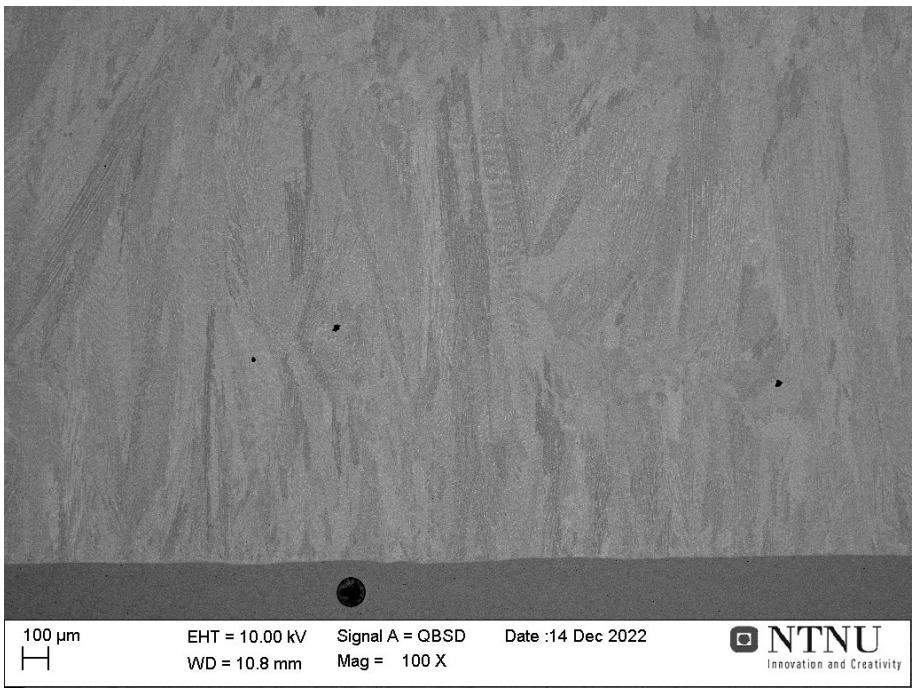

Figure 25: BSE image of IN718 deposited on a carbon steel substrate. Obtained from author's project work (Aas 2022).

In further work, the report suggests performing tensile testing of the single-material and the multi-material for addressing material properties such as tensile strength, ductility and strain hardening characteristics. Hardness testing could be done across the interface of substrate material and deposition material, in addition to heat treatment experiments for increased material strength. Furthermore, the report states the relevance of investigating multi-material depositions of aluminium bronze alloys and IN718, beneficial for aerospace components combining the material properties of high thermal conductivity and high strength, toughness and resistance to high-temperature fatigue. Some experiments were done in the project of cladding an aluminium bronze single-layer on top of IN718, apparently with success. However, challenges were experienced in the deposition of multiple layers of aluminium bronze due to poor fusion, and other parameter settings needed to be tested.

4 Materials and experimental methods

The experimental work is a continuation of the author's project thesis from the autumn of 2022. Further work proposed in the author's project work, it was suggested to perform mechanical testing, such as tensile tests and hardness tests, to reveal certain mechanical properties. Essential properties to investigate are strength, ductility and strain-hardening characteristics. With multi-material deposition, it is important to have an understanding of the developed microstructure, the phases arising from the mixing of two metals and how these features influence the material properties.

4.1 3D printer

The samples in this project were manufactured by a co-axial Wire-Laser Metal 3D printer, which utilizes LMD with wire as the additive manufacturing method. The range of the laser power is a maximum of 1.2kW, produced by six 200W direct diodes. The 976nm-wavelength lasers form a circular beam with a focal point on or near the sample surface, causing a blending of the substrate and the wire feedstock. The 3D printer is equipped with a hot-wire system, and a programmable power supply using resistance heating that preheats the wire inside the feeding mechanism before it is introduced to the melt pool. An active water-cooled chiller is integrated beneath the printing stage, acting as a heat sink to the substrate and the as-deposited material. The possible wire diameter to be used spans from 0.8mm to 1.2mm, but in this experiment, only 1.2mm wire diameter was used. To prevent high-temperature oxidation of the 3D printed material, a shielding gas of argon with a flow rate of 8 l/min was applied. For AM of multi-material deposition, the instrument also provides a dual-wire system, enabling automatic switching of two different wires without cross-contamination during printing.

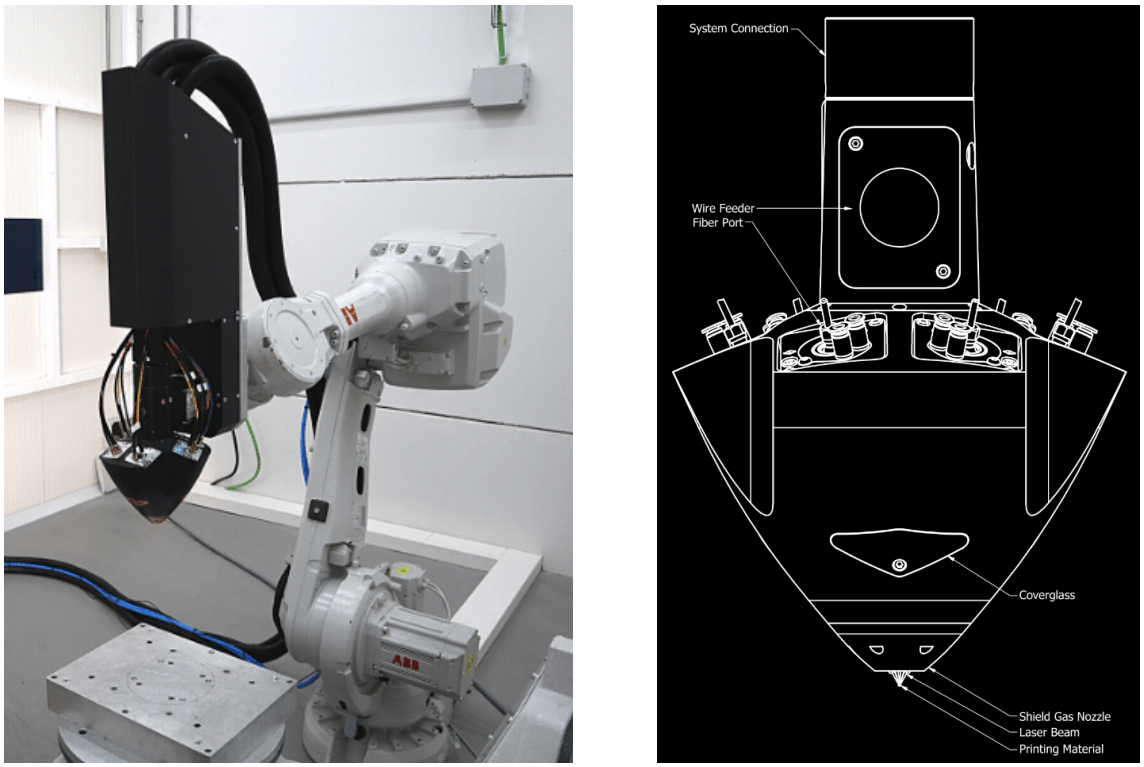

(a) (b)

Figure 26: An illustration of a) the robotic integration of the Meltio metal 3D printing solution and b) the Meltio multi-laser metal deposition head descriptions. Obtained from Meltio 2022a.

4.2 Materials

IN718 and CuAl7 were used to compose a bi-material part, combining both high strength and corrosion resistance at elevated temperatures, and high thermal conductivity. IN718 is the same material as used in the author's project work, with the chemical composition given in Table 9. The other material is the aluminium bronze alloy CuAl7, with the chemical composition shown in Table 6.

Table 9: Chemical composition of IN718 in percent by weight [wt%] used in the experiments (Meltio 2022b).

Ni	**Fe**	**Cr**	**Nb+Ta**	**Mo**	**Ti**	**Al**	**Si**	**Mn**	**C**
Base	20	19	5.2	3	0.9	0.5	0.2	0.2	0.05

Table 10: Chemical composition of CuAl7 in per cent by weight [wt%] used in the experiments.

Cu	**Al**	**Fe**	**Mn**	**Ni**
Base	8.0	< 0.5	< 0.5	< 0.5

4.3 Specimen multi-layer manufacturing

The additive manufacturing was performed in cooperation with SINTEF Manufacturing. The process parameters used for the deposition of IN718 were based on the author's project work, although subsequent improvements were performed by SINTEF. The parameters used for CuAl7 have been developed by SINTEF. The processing variables were chosen carefully to minimize the presence of defects such as pores and lack of fusion, in addition to optimizing the interlayer binding and especially the binding in the interface between the two materials. The parameters used are listed in Table 11.

Table 11: Process parameters used in the discrete layers for specimen manufacturing by LMWD. P is the laser power, v_t is the traverse speed, v_w represents the wire feed rate and P_w is the hot-wire power, while Z and d are the laser beam focal position and the hatch spacing, respectively.

Material	**Layer**	$P[W]$	$v_t[mm/s]$	$v_w[mm/s]$	$P_w[W]$	$Z[mm]$	$d[mm]$
IN718	1-2	1100	10	12	250	0	1.2
IN718	3-12	900	10	11-12	250	0	1.2
IN718	13-30	900	10	13	250	0	1.2
CuAl7	31-60	1200	10	11	250	-0.4	1.3

A cuboid-shaped sample with dimensions of 18x50mm was produced by applying the multi-layer deposition path strategy shown in Figure 27. The manufactured part is pictured in Figure 28. The deposition head was programmed to apply the material in a snake-like pattern, with a given hatch spacing between each bead. The adjacent layers were then added with a 90 degrees alternating build direction. As substrate material, a blasted carbon steel plate was used to first print multi-layers of IN718. CuAl7 was then deposited on top of IN718. In additive manufacturing of the part in Figure 28 the laser head had a small damage resulting in a non-vertical wire feed into the melt pool. The small angle difference made the wire move outside the part geometry on one side of the cuboid, seen from Figure 28b. This did, however, not affect the sample volume of interest around the interface.

In addition to the part described above, some selected tests were performed on a second specimen (Sample no. 2) manufactured in the same way as specimen number 1, only with a few deviations in the parameter settings (see Appendix A).

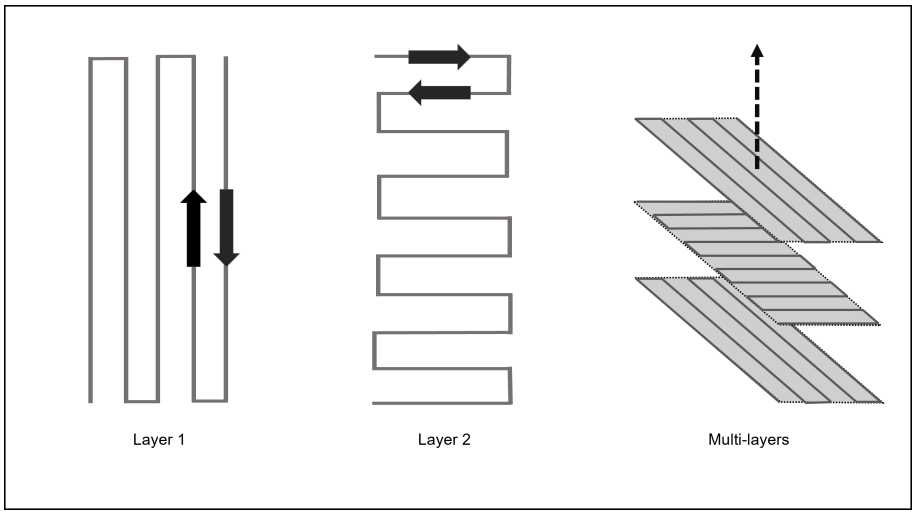

Figure 27: Multi-layer deposition path strategy with an alternating 90° orientation between each layer.

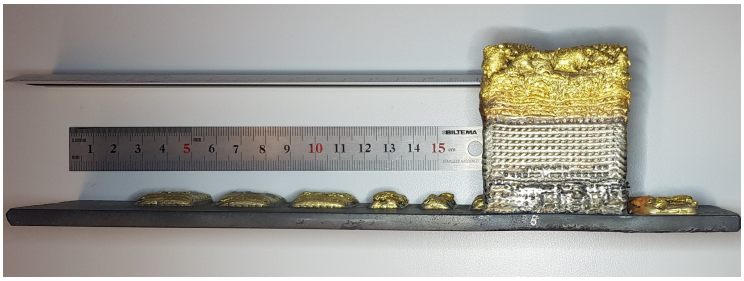

(a)

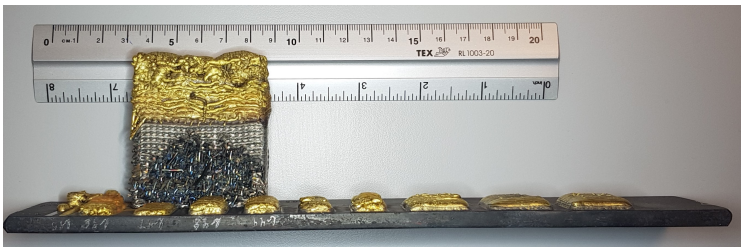

(b)

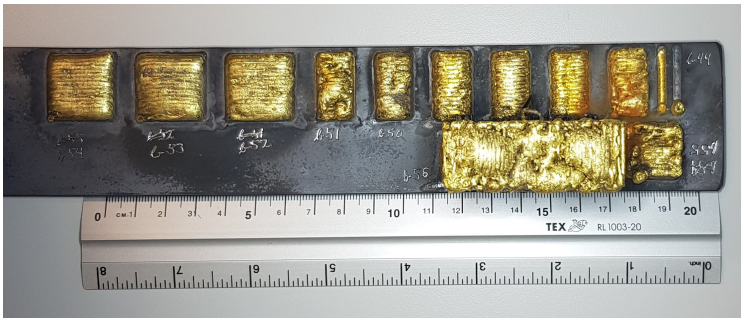

(c)

Figure 28: Macropictures of the as-deposited sample taken from different angles.

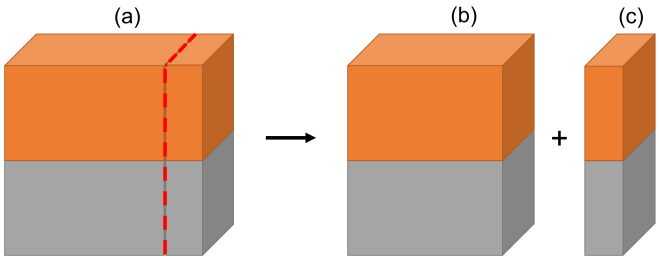

Figure 29: Sketch of the as-deposited sample (a) transversely cross-sectioned into samples (b) and (c). (b) was carried out to obtain tensile specimens and (c) was needed for investigation in LOM and SEM.

4.4 Mechanical testing

4.4.1 Tensile test

For tensile testing, the additively manufactured material was cut into micro specimens because of the limited material volumes. A zwickiLine 2.5 kN universal testing machine by ZwickRoell with micro specimen grips was used, including a laserXtens 1-15 HP extensometer. The instrument, seen in Figure 32, offered the high resolution needed to measure the elongations for samples with a minimum gauge length of 3mm. The speed used in the tensile tests was 0.5mm/min. The tensile test setup and sample mounting are shown in Appendix C, including a picture of a sample after fracture. Two to five test specimens were obtained from each part of the 3D printed material, depending on the volumes of non-defective material available.

The distance between the interface and $CuAl7_h(2)$ was approximately 5.5mm, and the distance between the interface and $CuAl7_h(1)$ was approximately 15mm. For $IN718_h$, the distance from the interface was 3.5mm and 13mm. The specimen positions are shown in Figure 30 where a minimum of 4 of each type (a, b, c) were obtained to have a larger basis of results. In addition, two horizontal specimens (d) were obtained in the interface with approximately 50% IN718 and 50% CuAl7.

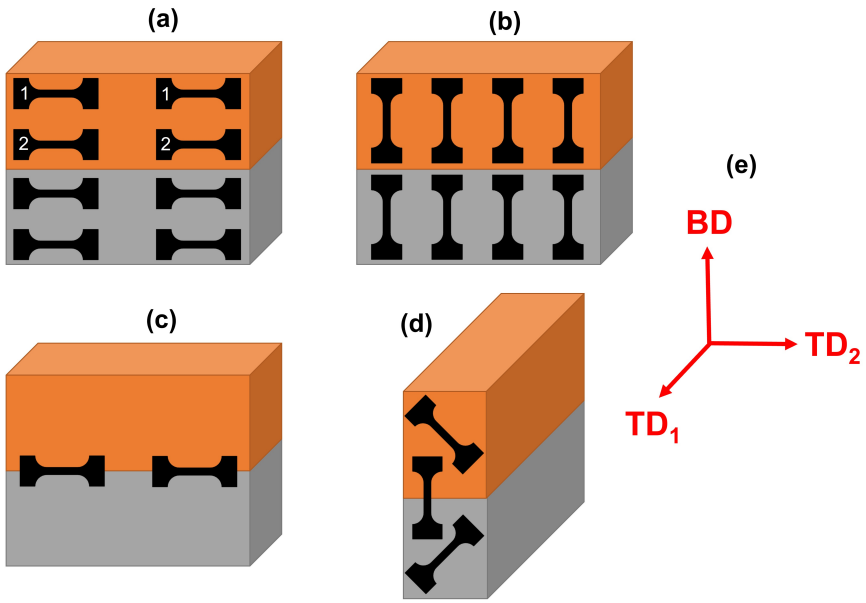

Figure 30: Sketch of the positions where the tensile specimens were obtained from the as-deposited material. (a) and (b) represents the horizontal (h) and the vertical (v) specimens in each material, while (c) represents the horizontal specimens parallel to the interface. (d) illustrates the vertical specimen over the interface and the tilted specimens in both IN718 and CuAl7 and (e) shows the building direction (BD) and the two alternating traverse directions (TD).

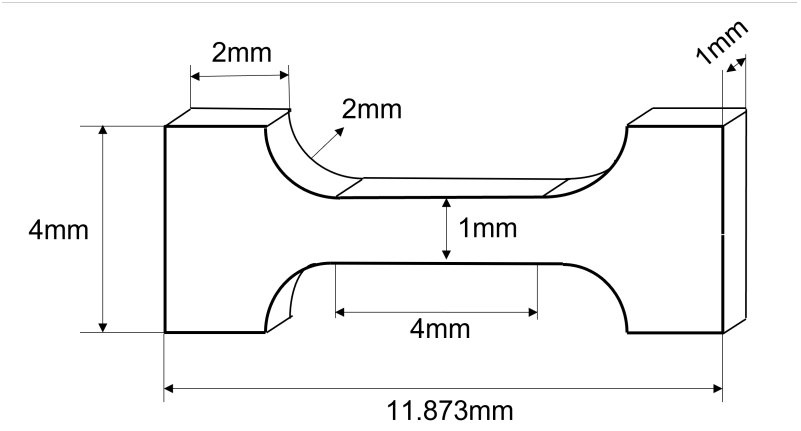

Figure 31: Sketch of the tensile specimen dimensions.

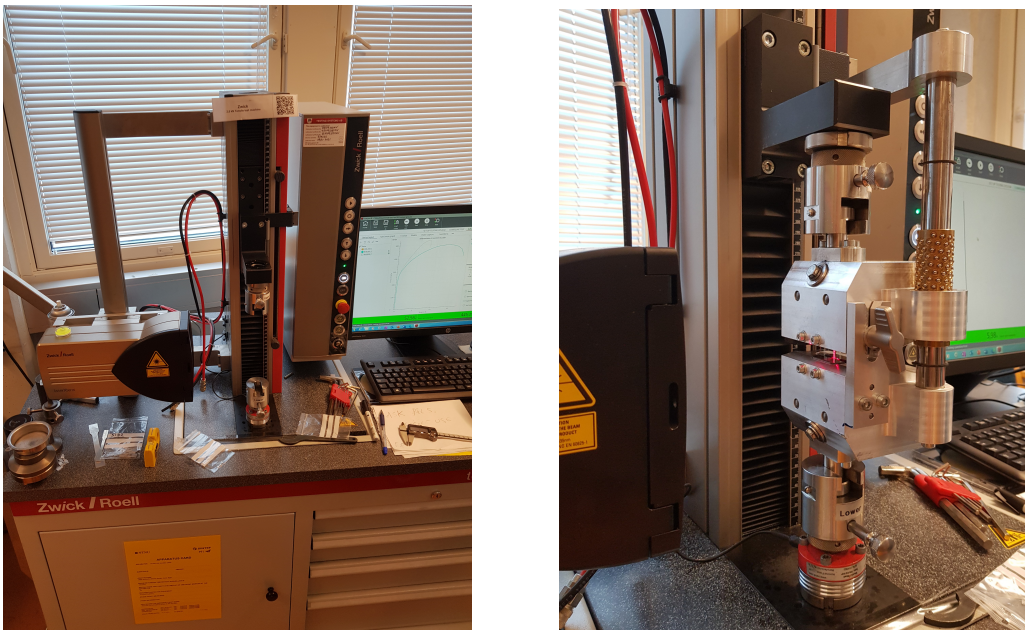

(a) (b)

Figure 32: Pictures of the tensile testing machine and setup. a) includes the laser extensometer and the tensile machine and b) shows a close-up of a mounted sample during testing.

4.4.2 Vickers Hardness Test

Innovatest Vickers hardness testing machine was utilized for Vickers hardness testing across the dual-metal interface. Leica Vickers Micro hardness testing machine was used to take small indents a shorter distance across the interface, with the possibility to measure the hardness with a weight of a minimum of 1g. The microhardness testing was performed according to ASTM E-384.

4.5 Light optical microscopy

To investigate the presence of defects and sufficient interlayer bonding in the AM material, a bulk material examination was necessary. For this, a section from the sample was carried out and examined in LOM.

4.5.1 Sample preparation

The sample was cross-sectioned with a fine-cutting machine and mounted in epoxy or PolyFast for grinding and polishing. In the grinding step, SiC foils with increasing fineness were used and subsequent polishing with $9\mu m$, $3\mu m$ and $1\mu m$ diamond suspension was carried out. The sample preparation steps are shown in Table 12. Between each grinding and polishing step, the samples were washed with water and soap, following rinsing with ethanol for drying. From step 3, between each step, an ultrasonic bath was used to remove particles on the material surface and inside voids, preventing the particles from scratching

the polished area. For this, a beaker with the respective sample immersed in ethanol was inserted in a bath for 5min. After this, a detailed investigation of the specimen in LOM could be performed. Figure 34 shows the sample subsequent to the preparation process.

Table 12: Manual grinding (steps 1-4) and polishing (steps 5-7) procedure in the specimen preparation. The table gives an overview of the surface, abrasive type, speed, preparation direction relative to the foil surface and time used for each step.

Step	**Surface**	**Abrasive type**	**Speed**[rpm]	**Dir.**	**Time**[s]
1	SiC foil	SiC #220	150	-	60
2	SiC foil	SiC #500	150	-	60
3	SiC foil	SiC #1200	150	-	60
4	MD-Allegro	DiaPro Allegro/Largo 9μm	150	Counter	180
5	MD-Dac	DiaPro Dac 3μm	150	Counter	180
6	MD-Nap	DiaPro Nap B 1μm	150	Counter	180

(a) Struers Accutom-5.

(b) Manual grinding machine.

(c) Manual polishing machine.

(d) Struers Tegramin-30.

Figure 33: The cutting (a), grinding (b, d) and polishing (c, d) machines used for sample preparation.

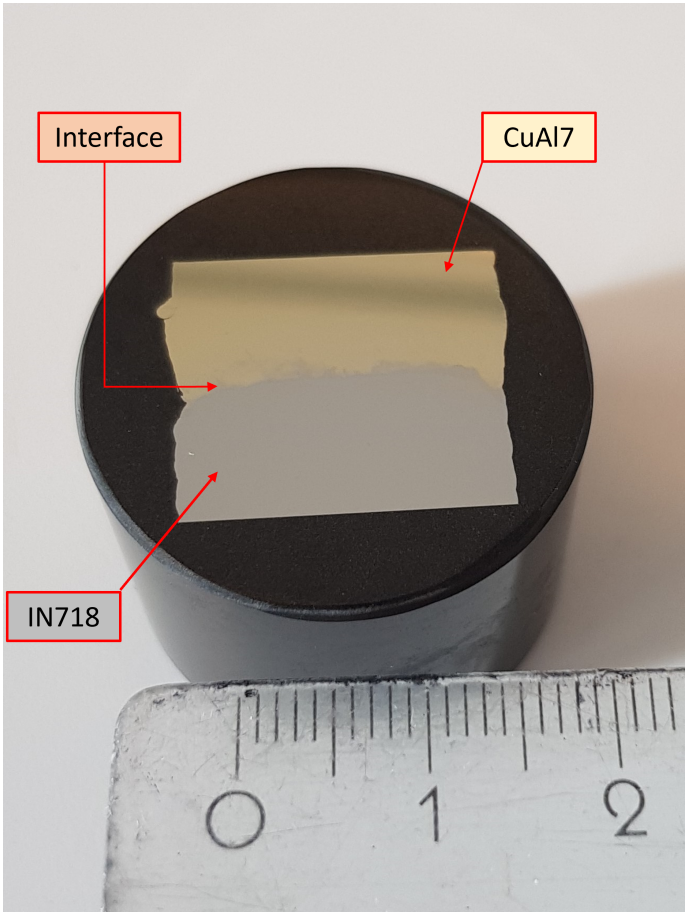

Figure 34: Prepared sample for characterization in SEM.

4.5.2 Characterization

For light optical microscopy, Zeiss Axio Vert.A1 Inverted light microscope was utilized in the examination and characterization of the sample cross-sectional area. The objectives available were 2.5X, 5X, 10X, 20X, 50X and 100X. An AxioCam 105 colour microscope camera with 5 Megapixels was installed in the instrument and the Zen Core software was used for picture taking and processing.

Figure 35: Zeiss Axio Vert.A1 Inverted light microscope.

4.6 Scanning electron microscopy

4.6.1 Sample preparation

For the purpose of microstructural investigation in scanning electron microscope (SEM), an additional polishing step was carried out after the preparation steps used for LOM. The sample was vibration, and chemo-mechanically, polished, using a VibroMet 2 Vibratory Polisher (Figure 36) and a MasterMet™ 2 Colloidal Silica suspension. It was set to 1 hour at a frequency of 60-70 Hz without any additional weight. The polishing step was performed to remove any minor deformations remaining, preparing the sample for different SEM applications, including EBSD, where a high-quality surface is crucial for obtaining any result.

Figure 36: VibroMet 2 Vibratory Polisher.

4.6.2 Characterization

Zeiss Ultra 55 SEM, equipped with a field emission electron gun (FEG), was used for further sample characterization. It was installed with a high-efficiency in-lens detector, a secondary electron detector (Everhart-Thornley) and a retractable backscatter electron detector. In addition, it had an EDS detector by Bruker (XFlash) and a NORDIF UF-1100 EBSD detector. Secondary electron imaging was primarily used to examine the fracture surfaces of tensile tests, while backscatter electron imaging was exercised to do chemical characterization and to investigate microstructural features. Energy dispersive spectroscopy was used to do chemical analysis, and electron backscatter diffraction imaging was utilized to reveal to map different phases and grain orientations in the material.

5 Results

5.1 Prediction of equilibrium phases

From Thermo-Calc, a diagram of the volume fraction of phases with respect to temperature was obtained for each of the two alloys used in the experiments (Figure 37 and Figure 38). In addition, the same type of diagram with 50% IN718 and 50% CuAl7 was produced (Figure 39). Although this only applies to equilibrium conditions, this could give a pointer on which phases one can predict in the bimetallic additive manufacturing of the two materials. The same modelling study of IN718 was performed by Caliari et al. 2013 with some differences in chemical composition. The diagram obtained in this project, showing the fraction of phases versus temperature, is presented in Figure 37a. At temperatures around 1320℃, IN718 starts to solidify to the fcc matrix phase (blue) from the liquid (purple). The phases forming between 500 and 1200℃can be identified by zooming in. From Figure 37b it is seen that no. 1 is the liquid phase. The phases of considerable volume fractions are phases no. 3-7. Phase 3 is Ni_3Nb (D0a), phase 4 is σ (D8b), phase 5 is fcc (L12), phase 6 is Laves (C14) and phase 7 is bcc (A2).

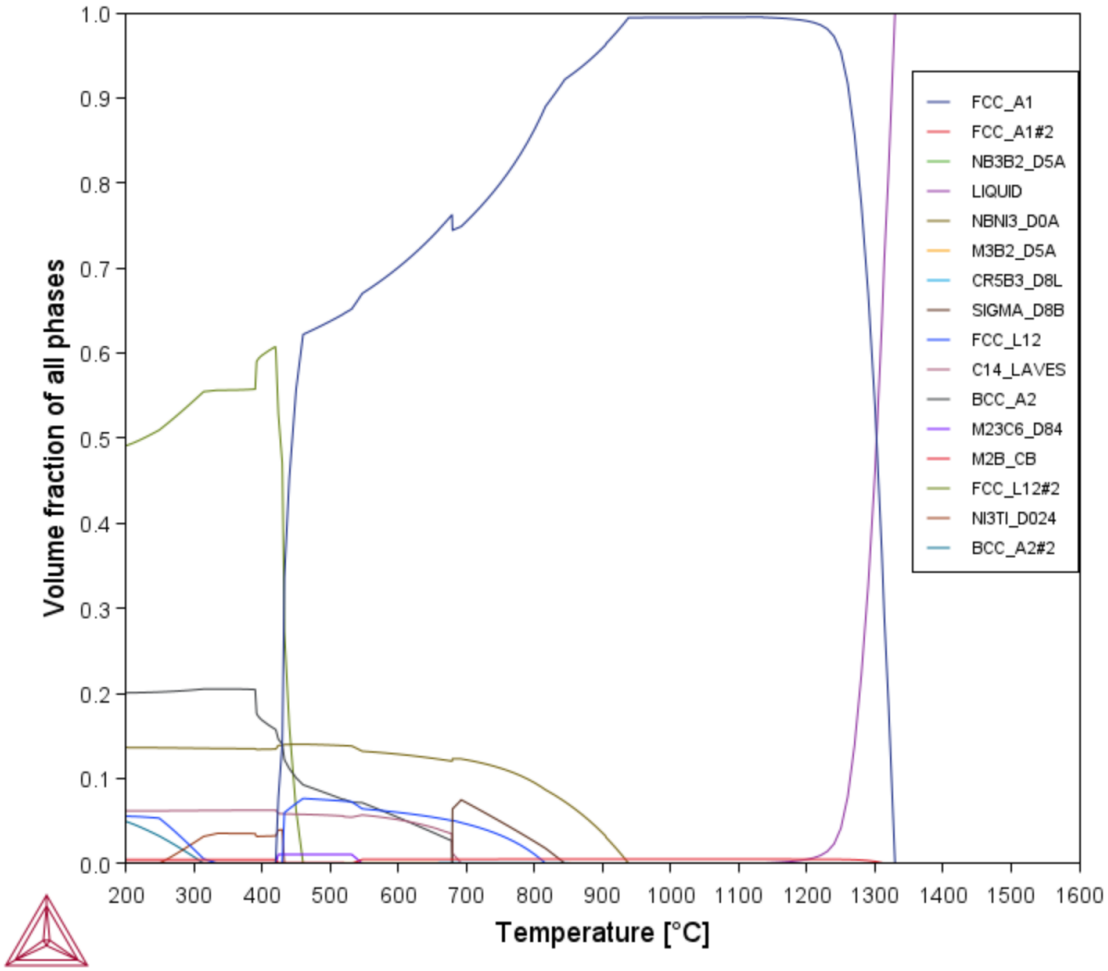

(a)

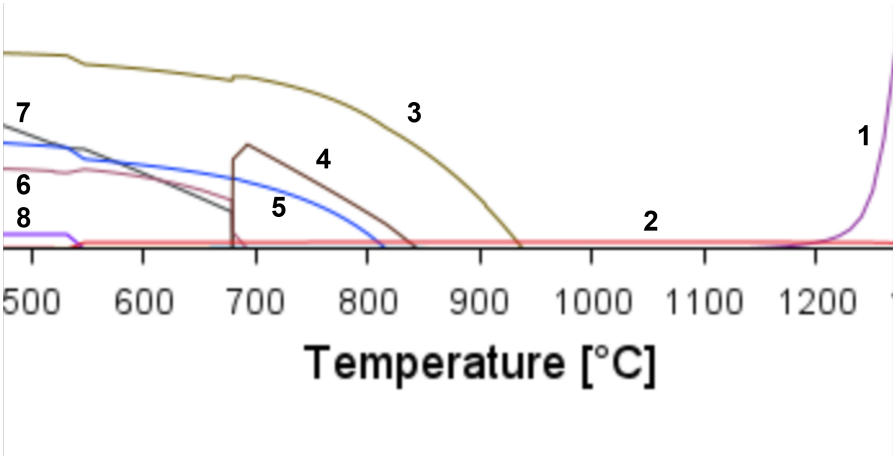

(b)

Figure 37: Modelling of phases in IN718 with the chemical composition given in Table 9 using Thermo-Calc. The figure shows the volume fraction of phases on the y-axis and the temperature on the x-axis. Figure (a) is a zoomed-in section of (b).

In Figure 39, CuAl7 was considered with the chemical composition given in Section 4.2. This aluminium bronze has a lower melting point than IN718 at approximately 1030℃. It solidifies to around 60% fcc (A1) and 40% bcc (A2). During cooling, the bcc transforms to fcc. At approximately 740℃, the bcc (A2) transforms to both fcc and bcc (B2). From the phase diagram in Figure 10, the same observation can be made with a solidification to α phase and β phase from the liquid state, with further promotion of α phase upon cooling.

A mixing of 50% IN718 and 50% CuAl7 at equilibrium conditions was modelled in Thermo-Calc and the result is shown in Figure 39. The complex diagram contains a lot of different phases, where the majority are IN718 phases. The first phase to form during cooling is the Laves phase (C14) at 1260℃, seen from the green line. Then, fcc (A1) forms given by a yellow line. At around 1130℃, σ (D8b) forms and at 1030℃ the remaining liquid solidifies into mostly fcc (A1). At the same temperature, the σ phase is apparently set to transform into bcc (A2). Between 800 and 900℃ the fcc (L12) starts to form, in addition to the CuAl7 phase bcc (B2). Around 600℃, the phases transform into a lot of other phases. However, many of them have fcc structure, in addition to Ni_3Nb and another Laves phase.

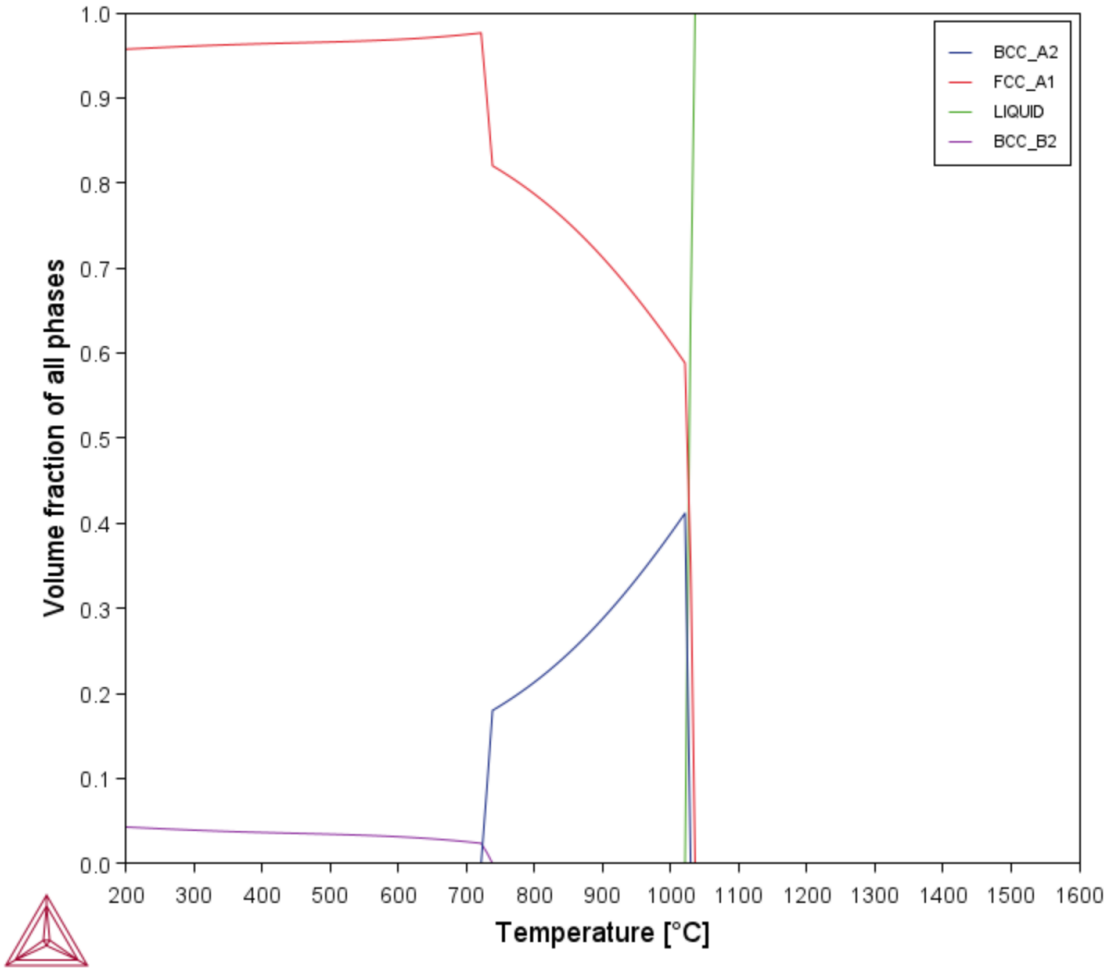

Figure 38: Modelling of phases in CuAl7 with the chemical composition given in Table 10 using Thermo-Calc. The figure shows the volume fraction of phases on the y-axis and the temperature on the x-axis.

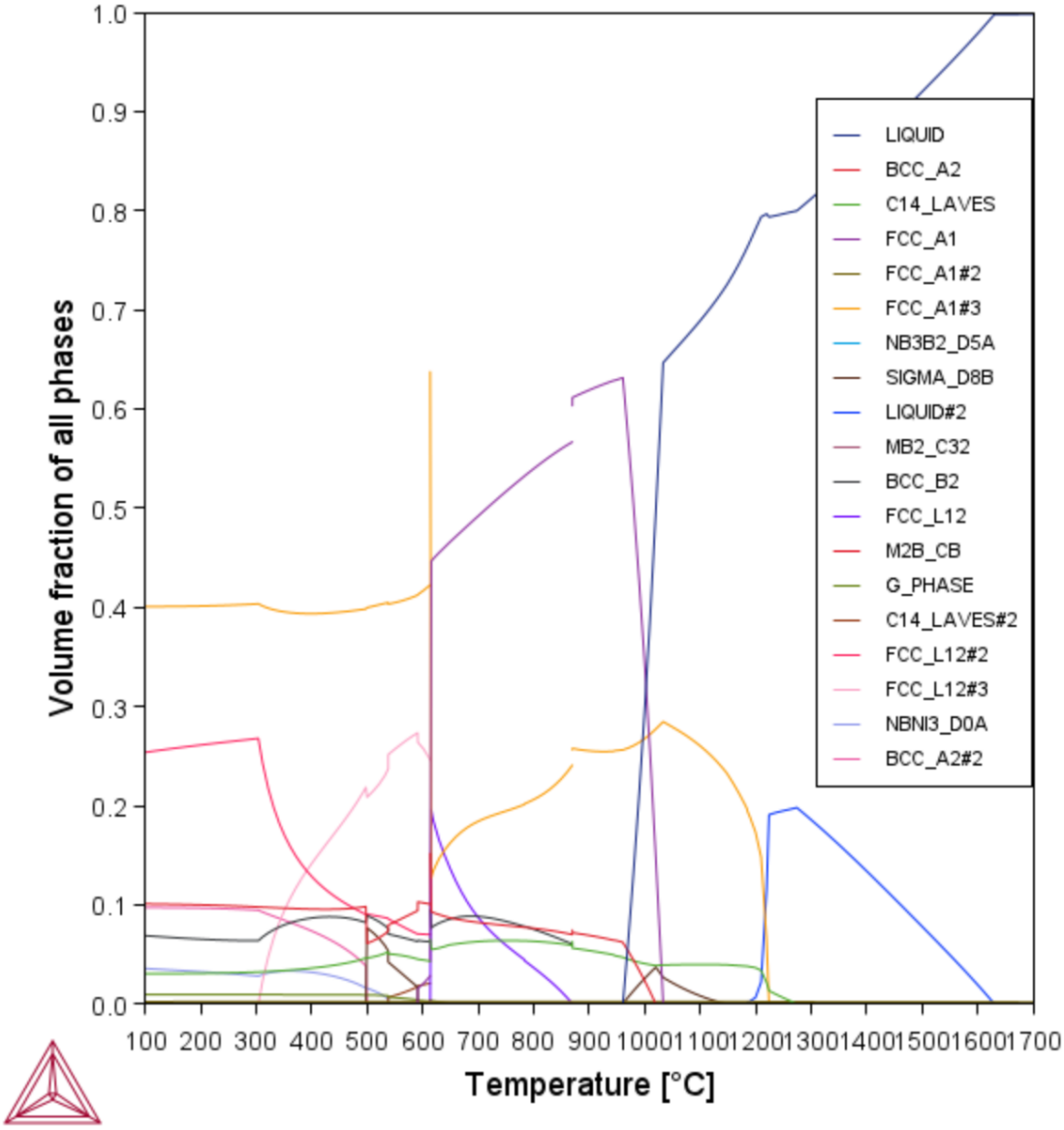

Figure 39: Modelling of phases in 50% IN718 and 50% CuAl7 using Thermo-Calc. The figure shows the volume fraction of phases on the y-axis and the temperature on the x-axis.

5.2 Images from LOM

Figure 40a shows the interface between IN718 and CuAl7. An interface with good fusion is obtained, containing no visible defects in terms of large pores or lack of fusion. Also, both the Ni-based superalloy and the aluminium bronze showed high-quality performance in interlayer fusion (Figure 40b and Figure 40c). In the blending zone between the two alloys, a dark cloud in the Al bronze is observed in various portions and distances from the interface. Small grains are visible in this zone. Further up, the cloud vanishes and the Al bronze becomes more particle-free, where larger grains were developed.

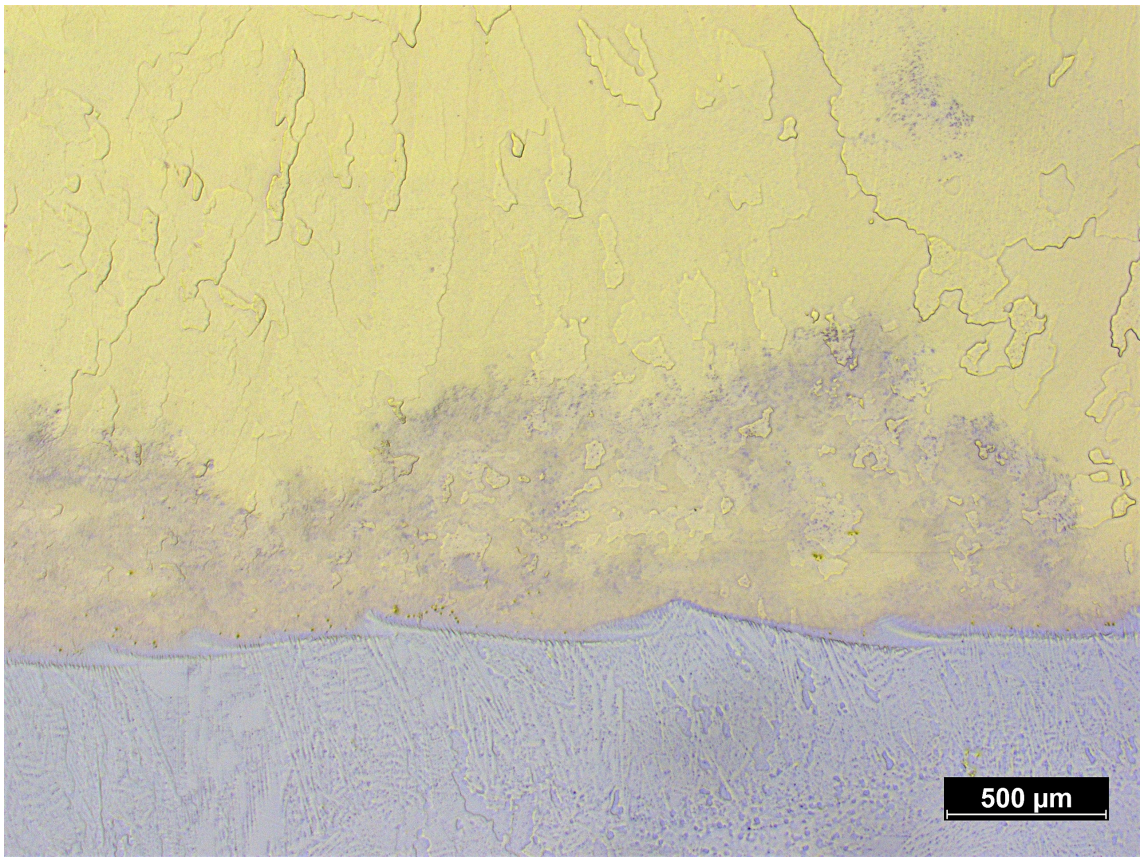

(a)

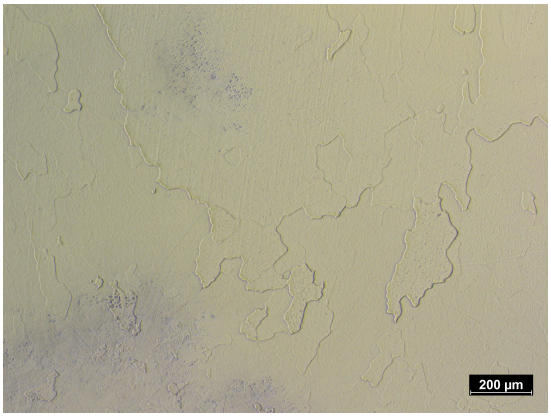

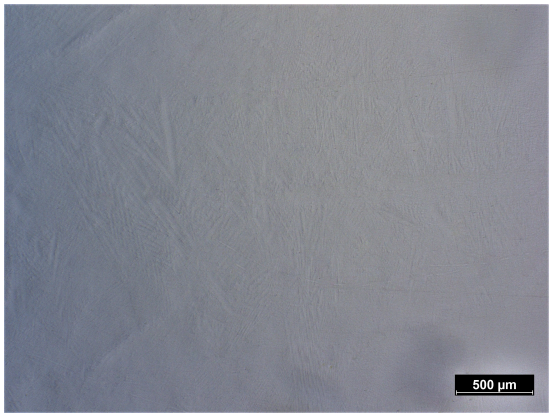

(b) (c)

Figure 40: LOM images of interface (a), CuAl7 (b) and IN718 (c).

In Figure 41a and b, a more refined structure is revealed, showing fine directional dendrites grown from the IN718 surface. Lots of particles are formed in the Al-bronze-rich structure, terminating the directional growth from Inconel. A belt of equiaxed dendrites is seen a small distance from the interface, while various particles dominate further up in the material.

(a)

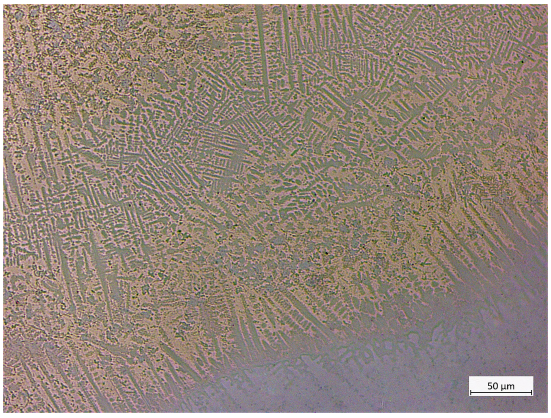

(b)

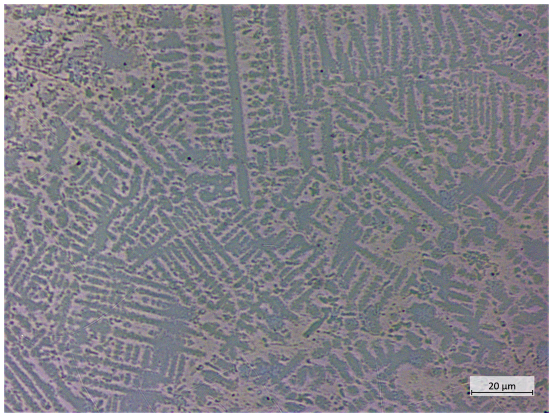

(c)

Figure 41: Detailed LOM images of the interface.

5.3 Microstructural analysis

Figure 42 shows a backscatter electron image of the interface. An aligned dendrite structure is seen with continued growth into the deposition of CuAl7. The heavy dendrite-based structure within IN718 converts to an equiaxed grain zone, including clouds of particles. EDS analysis was performed on the same areas as several of the BSE imaged areas obtained in this section. Later in the report, Figure 43d, Figure 46d, Figure 46f and Figure 47d will therefore be referred to as zone 1, 2, 3 and 4, respectively. Figure 43 shows a step-

by-step zoom of the interface zone. In Figure 43a, and more pronounced in Figure 44, the grains in IN718 are clearly visible. At a distance of around $400\mu m$ from the interface, an equiaxed grain zone is observed in a nearly horizontal line. Above this zone, columnar grains have formed stretching all the way to the IN718 surface. In the zoomed-in image in Figure 43b, the white interdendritic zones become clear. As in the LOM images, the equiaxed zone in the CuAl7 is present a short distance from the interface. Figure 43a and b show light rosette-formed particles in the interfacial zone, including small dark particles with an apparent 90° orientation preference relative to each other.

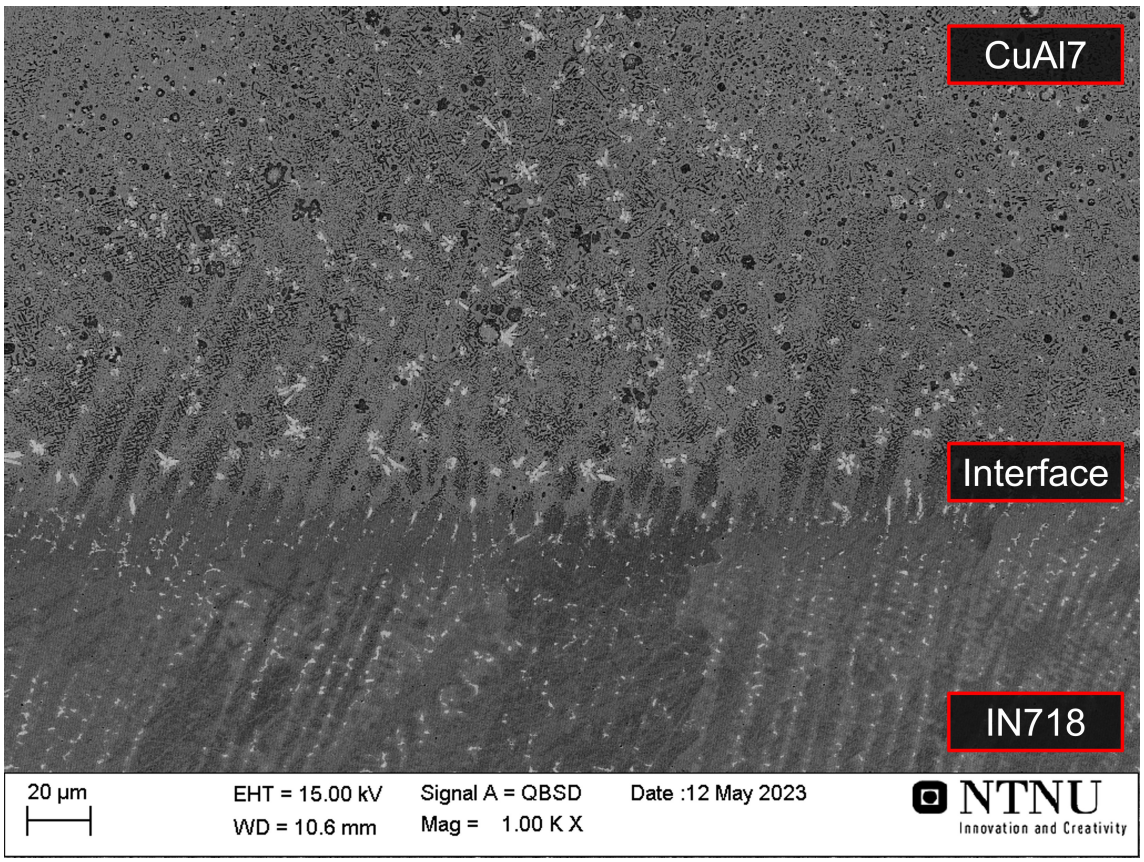

Figure 42: BSE image of the interface. IN718 dendrites are seen to have grown into CuAL7 and diverse particles are seen in the interfacial zone.

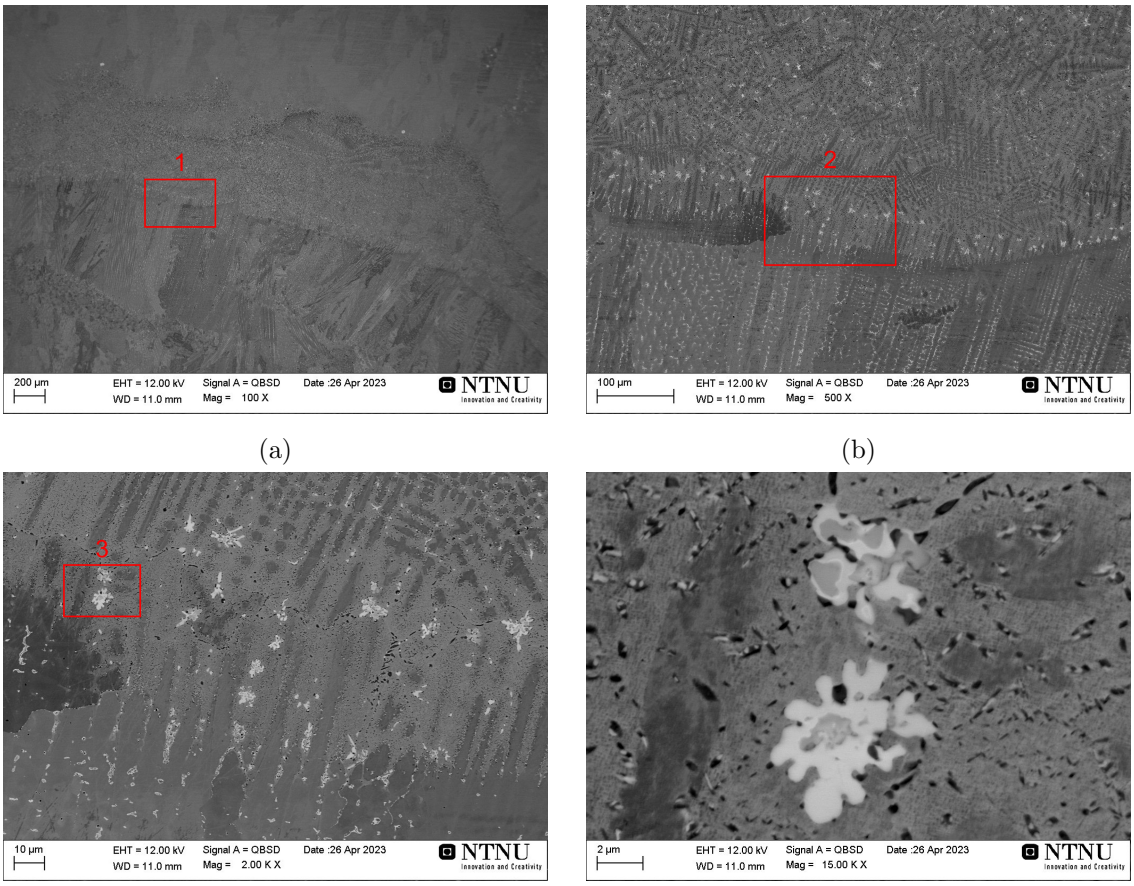

(a) (b)

(c) (d)

Figure 43: Zoomed-in BSE images of dendrites and bright particles in the interface. The sample area d) is referred to as zone 1.

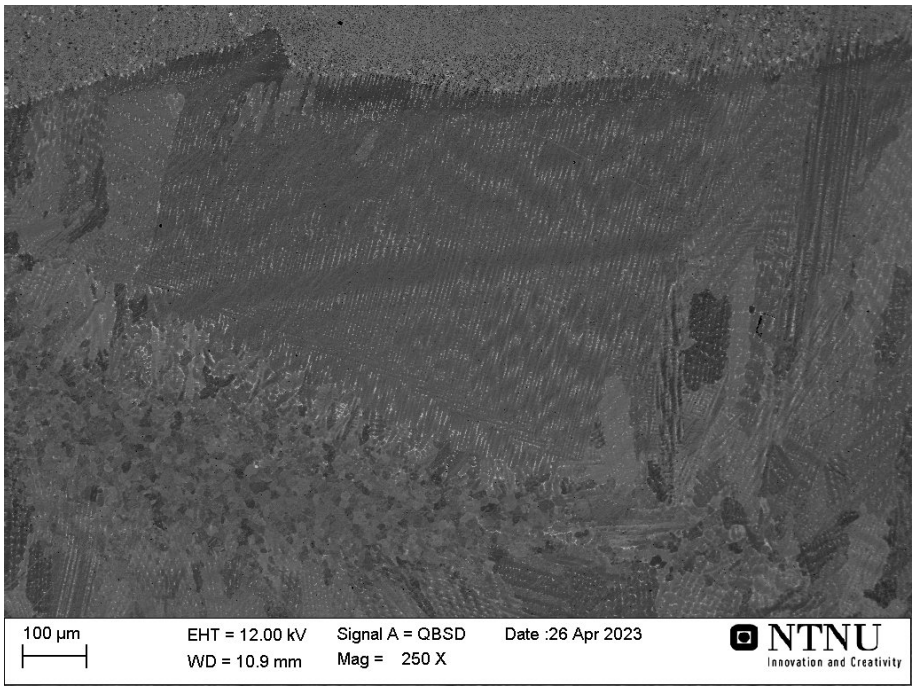

Figure 44: BSE image of microstructure in IN718.

The same examination was done at a larger distance from the interface, shown in Figure 46. Figure 46a is the same image as Figure 43a but with another area of interest. As the distance from the interface becomes larger, the equiaxed grains get smaller and more diffuse. The transition is seen from Figure 45 where the bottom part of the image contains a well-defined equiaxed structure, while the dendrites in the top region have become coarser containing small plate-like particles. From Figure 46d, it is seen that these particles lie in a semi-organized manner, alternating with an angle between them. In Figure 46e, at the upper part of the particle cloud, more fine-dispersed particles are observed. The light rosette-shaped particles are seen in this area too. Also, larger dark spherical particles are present in addition to aligned fine particles between the coarse dendrite arms.

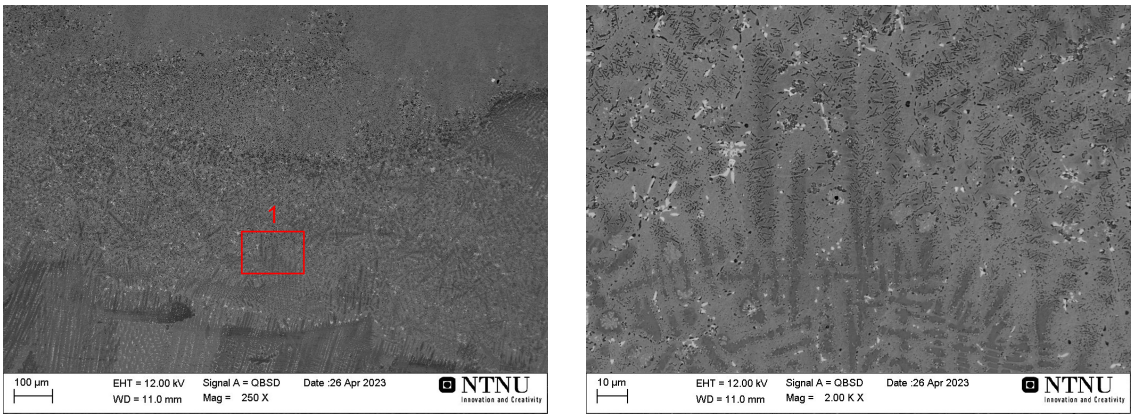

(a) (b)

Figure 45: Zoomed-in BSE images of equiaxed dendrites in the interface.

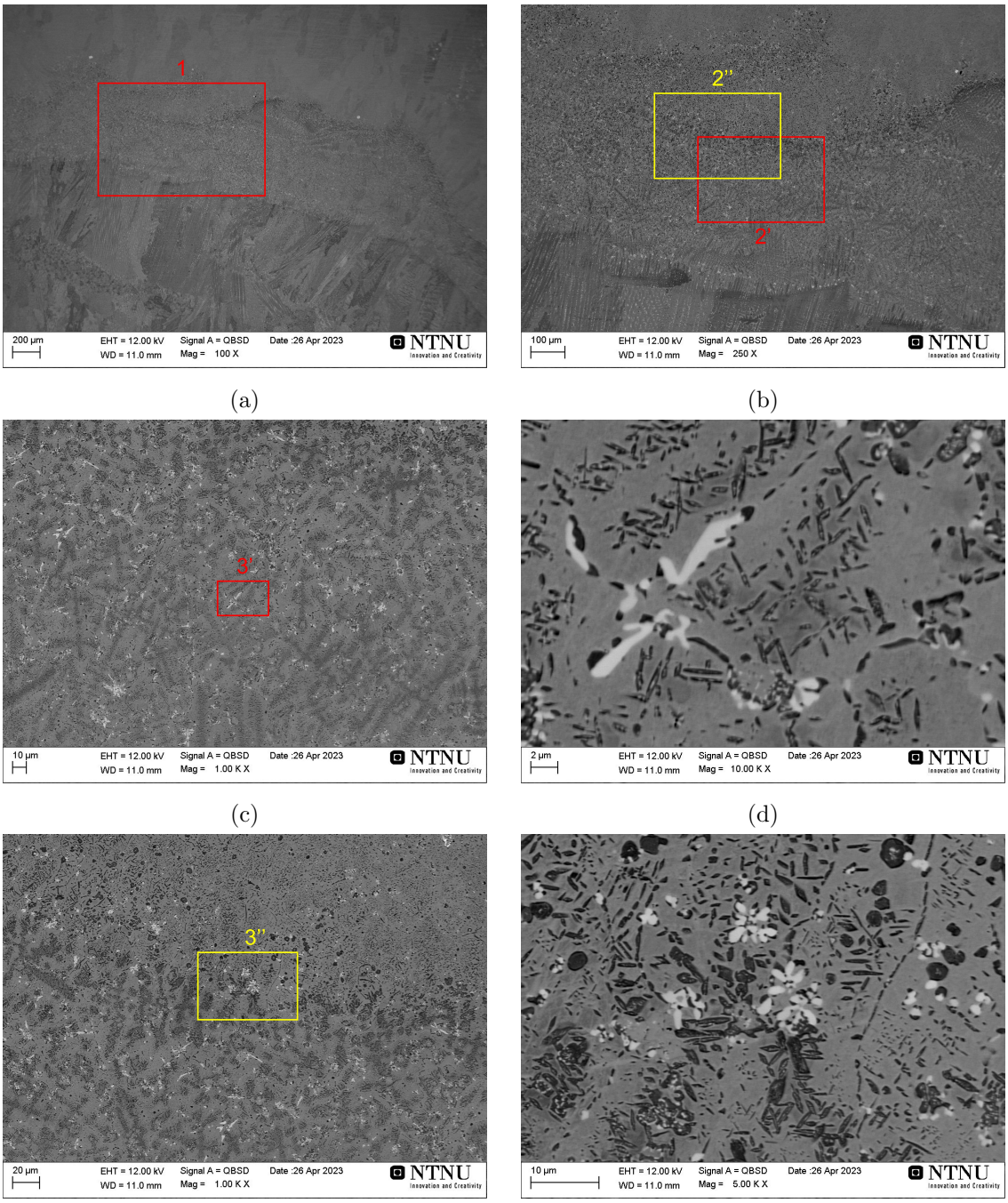

Figure 46: Zoomed-in BSE images of various particles and coarse dendrites in the interface. The sample areas d) and f) are referred to as zone 2 and 3, respectively.

From Figure 47, the light rosette-shaped particles are observed to be present to a smaller extent and with a decreased size. The dark plate-like particles have a coarser nature at this distance from the interface than at a shorter distance, and what was the diffuse presence of dark dendrites (Figure 45) is now perished. The dark spherical particles have increased in size, with many of them having a lighter core. Also, the aligned particles along what seems to be a grain boundary are more clearly seen in Figure 47 than in Figure 43.

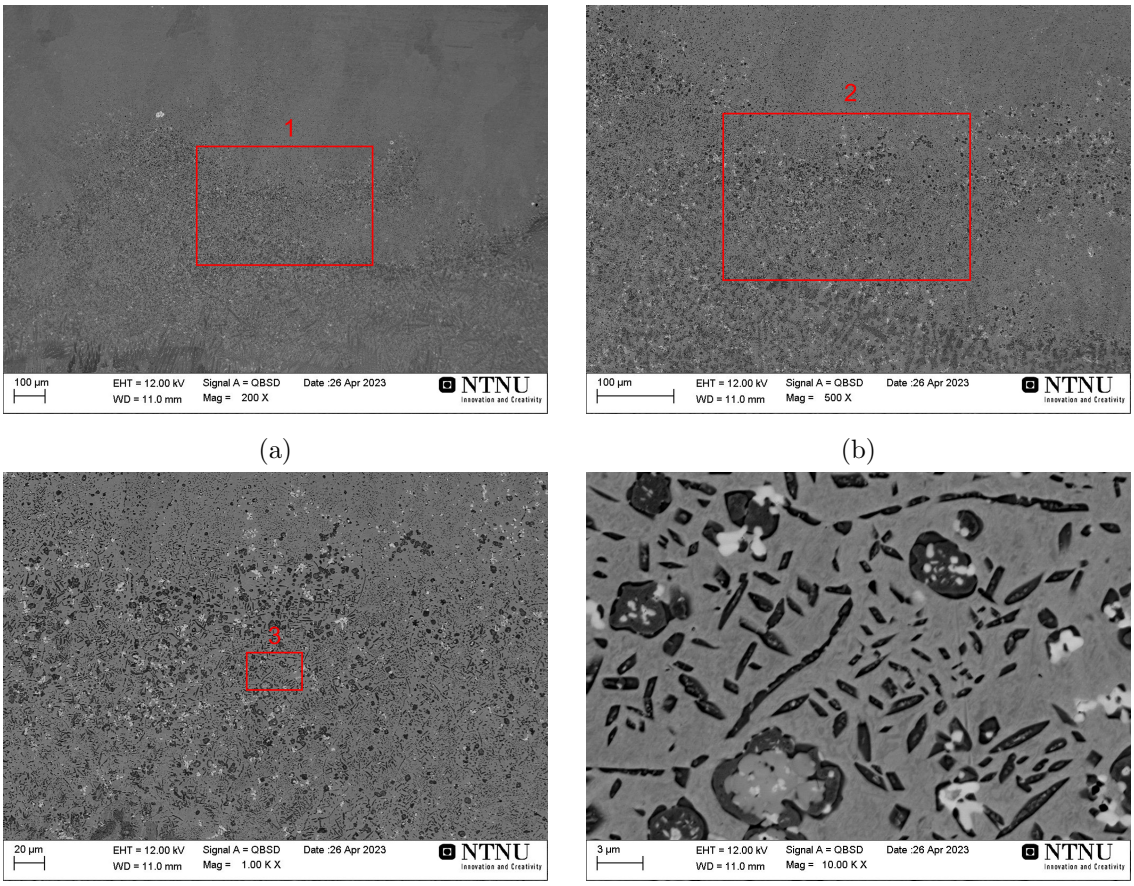

Figure 47: Zoomed-in BSE images of various particles around grain boundaries in the interface. The sample area d) is referred to as zone 4.

5.4 Chemical analysis of microstructure

EDS was used to analyse the elements present in different phases examined in Section 5.3 in the as-deposited multi-material. Carbon was not considered in the EDS analysis because a sample surface exposed to air will always be contaminated by carbon, thus making it difficult to know whether the carbon signal comes from the material or the contamination. The resulting chemical compositions were obtained from the raw EDS data presented in Section B.1. Figure 48 represents the bulk IN718 with its white-shaded interdendritic phases. The element with the largest difference in composition between bulk IN718 and the interdendritic phase is Nb. The white-shaded regions contain over 20wt% Nb and have a higher concentration of both Mo and Ti. The bulk material is richer in Ni, Fe, Cr, Al and Mn.

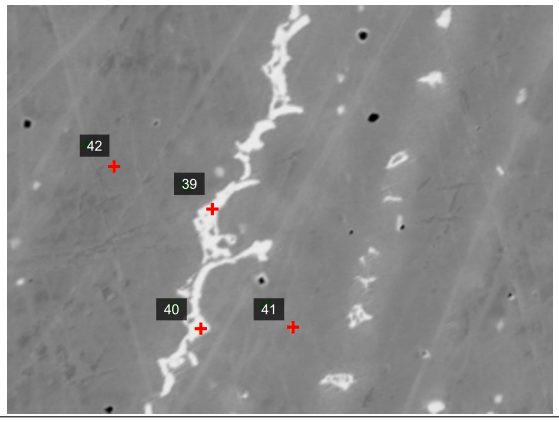

Element	Cu	Ni	Cr	Fe	Al	Nb	Si	Mo	Mn	Ti
39	0.0	39.8	13.3	15.6	0.2	22.8	0.4	6.3	0.6	1.2
40	0.0	36.4	13.7	15.8	0.1	25.5	0.4	6.3	0.6	1.1
41	0.0	54.2	16.9	20.4	0.5	3.7	0.1	2.5	1.0	0.8
42	0.0	55.1	17.2	22.0	0.5	1.7	0.1	2.0	1.0	0.4

Figure 48: EDS of microstructure in IN718 given in [wt%].

The near-interface microstructure from Figure 49 obtains relatively large white particles. These (samples no. 6 and 11) contain a high fraction of Nb and Mo compared to other phases, and they have almost the same concentration of all elements. Samples no. 7 and 8 are taken from the bulk material (not particles), where the former covers a dendrite that originated from the IN718 bulk (Figure 43) and the latter is obtained from the matrix in the blending zone. The dendrite is observed to have higher concentrations of Ni, Cr, Fe, Nb, Mo, Mn and Ti but a lower Cu, Al and Si content, compared to the blending zone bulk. The dark particles in the BSE images were also examined. However, large variations in the chemical compositions between them were obtained.

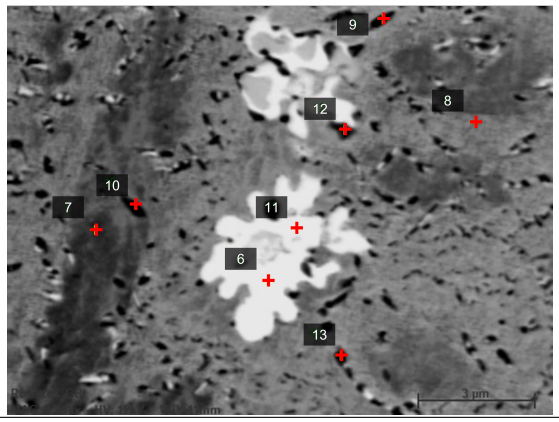

Element	Cu	Ni	Cr	Fe	Al	Nb	Si	Mo	Mn	Ti
6	0.3	19.0	20.8	21.1	0.6	23.2	0.5	13.3	0.8	0.5
7	27.0	37.6	9.2	16.3	4.7	1.7	0.6	1.5	0.8	0.6
8	53.5	28.9	1.6	5.7	5.9	0.8	2.0	0.9	0.3	0.3
9	41.0	35.6	4.5	6.0	8.9	0.8	1.3	1.0	0.6	0.4
10	11.3	13.0	49.7	16.2	2.2	1.5	0.1	2.6	2.9	0.5
11	0.9	16.7	26.0	21.6	0.6	17.9	0.4	14.5	1.2	0.4
12	34.3	31.4	14.5	8.4	7.1	0.5	0.7	1.7	1.1	0.3
13	27.2	16.5	32.2	13.4	3.8	3.0	0.4	0.9	2.6	0.2

Figure 49: EDS of microstructure in the interface (zone 1) given in [wt%].

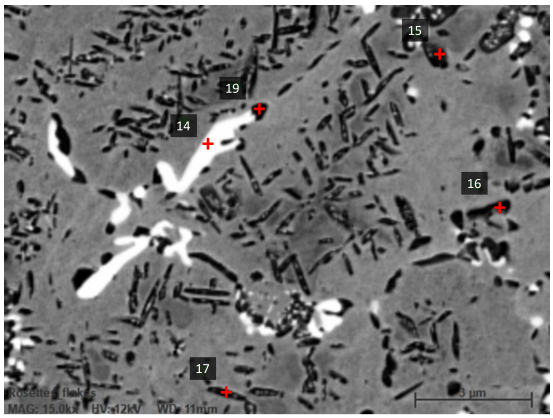

Element	Cu	Ni	Cr	Fe	Al	Nb	Si	Mo	Mn	Ti
14	0.4	19.9	19.2	22.5	0.8	30.6	0.7	4.4	1.0	0.6
15	20.3	28.6	23.8	16.2	7.5	0.3	0.4	0.9	1.7	0.3
16	41.2	35.5	4.5	7.0	8.8	0.4	1.1	0.9	0.5	0.3
17	30.1	19.8	25.7	15.2	4.5	1.6	0.4	0.8	1.9	0.1
19	11.1	5.9	61.7	14.9	1.5	0.4	0.1	0.3	3.8	0.1

Figure 50: EDS of microstructure in the interface (zone 2) given in [wt%]

A high Nb content in the white particles in Figure 50 was again obtained, with a slightly lower wt% of Mo. Dark particles were again investigated, resulting in differences in com-

position. The plate-like particle (no. 17) is experienced to contain much Cr, Ni and Fe, with also a high EDS signal from Cu. Sample no. 19 showed an extraordinarily high concentration of Cr with over 60wt%. In contrast, sample no. 16 contains very little Cr and also Fe, while no. 15 is shown to contain the same Cr fraction as no. 17. The Al content is the highest for sample no. 15 and 16.

Figure 51, representing the area of interest in Figure 46f, have a bulk material with approximately 65wt% Cu, 6wt% Al, 20wt% Ni and 5wt% Fe thus holding a high concentration of CuAl7. Compared to the bulk material sample no. 8 in Figure 49, this sample contains a slightly higher concentration of CuAl7 elements. Also in this region, the white-shaded particles contain a high fraction of Nb and Mo and almost no Cu. The spherical dark particles (no. 20 and 21) contain mostly Cr and Fe, around 13wt% Ni, but also considerable amounts of Mo and Mn. Sample no. 25 represents a dark-shaded particle in the dendritic structure in the blending zone. This is set to contain a high fraction of Ni, over 10wt% Al, and some Fe and Cu in addition to a fraction of heavier elements (Nb and Mo).

The last sample area showed high Al concentrations in most of the dark-shaded particles. Compared to the matrix (no. 37), sample no. 29 contains higher fractions of Ni, Cr, Fe, Al, Nb, Mn, and Ti. The two multi-coloured particles (no. 30, 31, 33, 34, 35) give the same indication of higher fractions of Cr, Fe, Nb and Mo in the bight regions and domination of Ni and Al in the dark part of the particles. Furthermore, the mono-coloured dark particle no. 38 contains only about 10wt% Ni but in return about 50wt% Cr and a nearly 30wt% of Fe.

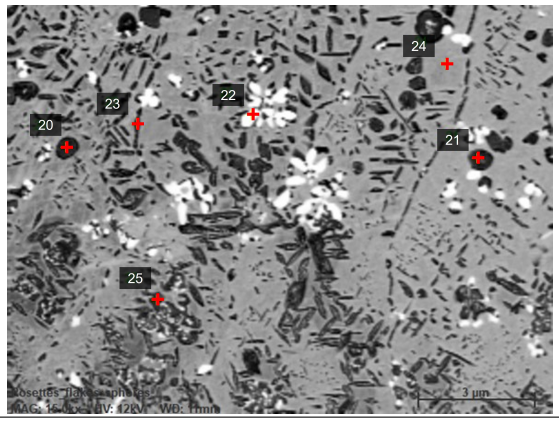

Element	Cu	Ni	Cr	Fe	Al	Nb	Si	Mo	Mn	Ti
20	4.9	13.3	45.7	25.0	2.5	1.6	0.1	4.2	2.4	0.3
21	4.2	13.1	45.8	26.3	2.7	1.4	0.2	3.7	2.3	0.3
22	0.3	14.2	19.9	25.7	0.6	21.1	0.5	16.7	0.7	0.4
23	19.6	29.5	21.4	16.8	8.9	0.5	0.5	0.7	1.7	0.5
24	63.7	18.3	1.1	4.8	6.4	0.8	2.8	1.4	0.5	0.2
25	12.3	51.2	6.7	11.2	12.5	1.9	0.8	2.0	0.6	0.8

Figure 51: EDS of microstructure in the interface (zone 3) given in [wt%].

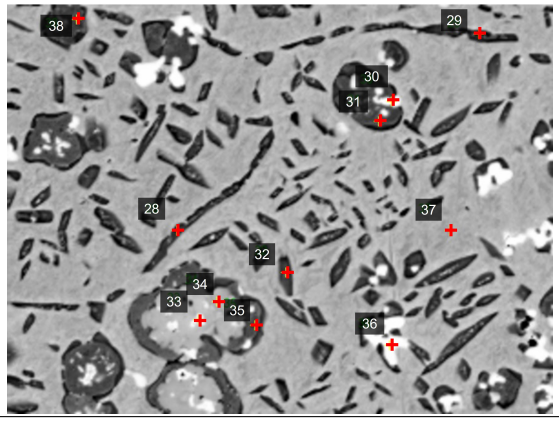

Element	Cu	Ni	Cr	Fe	Al	Nb	Si	Mo	Mn	Ti
28	54.0	26.1	0.5	3.9	10.6	1.0	2.3	1.5	0.0	0.1
29	14.5	35.4	16.8	17.4	10.6	2.0	0.5	0.8	1.3	0.8
30	8.5	11.4	28.5	28.8	2.7	12.4	0.3	5.3	1.5	0.7
31	12.3	33.9	24.2	16.0	8.5	0.9	0.4	1.8	1.6	0.6
32	38.5	37.1	1.6	6.1	11.6	1.1	1.7	1.5	0.3	0.6
33	4.1	10.5	35.3	30.3	0.8	5.0	0.2	12.1	1.6	0.3
34	7.0	10.2	37.1	30.5	0.9	2.2	0.1	10.2	1.8	0.2
35	13.6	37.7	17.9	15.2	10.8	0.5	0.4	2.0	1.2	0.7
37	64.3	17.7	1.1	4.8	6.3	0.8	2.8	1.4	0.5	0.2
38	5.1	11.2	47.0	27.7	4.0	0.3	0.2	1.7	2.5	0.4

Figure 52: EDS of microstructure in the interface (zone 4) given in [wt%]

5.5 Microstructural characterization with EBSD

EBSD analysis was carried out from a selected area on the interface of the prepared sample. Figure 53 shows two image quality (IQ) maps with different magnifications of the same area of interest. The colour on the grey scale inFigure 53b, or the contrast, provides useful information on the microstructure as the contrast represents the quality of the detected EBSD signals from the sample. The white regions are easy to detect while in the black areas, there is too much noise for any orientation to be detected. It is seen that IN718 gives the best quality where signals are easily detected. The equiaxed dendrites in the blending zone also have relatively decent quality. These can be seen both close to the interface and at larger distances, with darker regions in between.

(a)

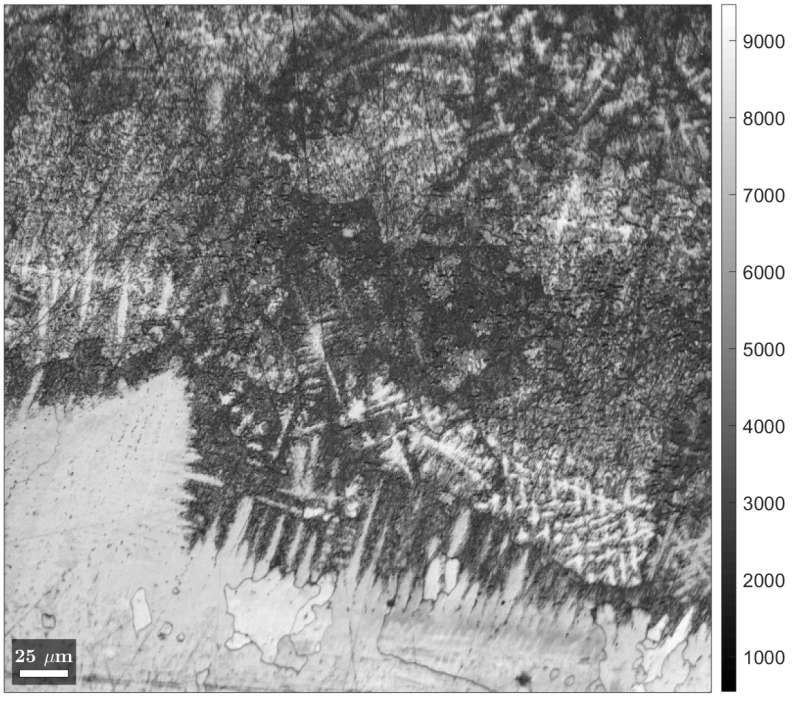

(b)

Figure 53: Image quality (IQ) maps of a part of the interface (IN718 on top of CuAl7). A good signal is obtained from IN718, but CuAl7 phases appear as dark areas indicating a poor surface finish. EBSD data processed by Håkon Linga.

Figure 54 and Figure 55 show the same areas pictured in the IQ maps as inverse pole figure maps. In the latter figure, the grains have been highlighted. The projection axis is parallel to the building direction for both images. The grain sizes are seen to be of a high variety, with large grains in IN718 to smaller grains above the interface. The equiaxed grains from Figure 53 are observed to be a part of larger grains, i.e. having the same orientation, including the interdendritic zones.

(a)

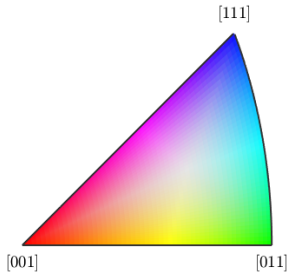

(b)

Figure 54: IPF map of a part of the interface (IN718 on top of CuAl7) with projection axis parallel to the building direction. EBSD data processed by Håkon Linga.

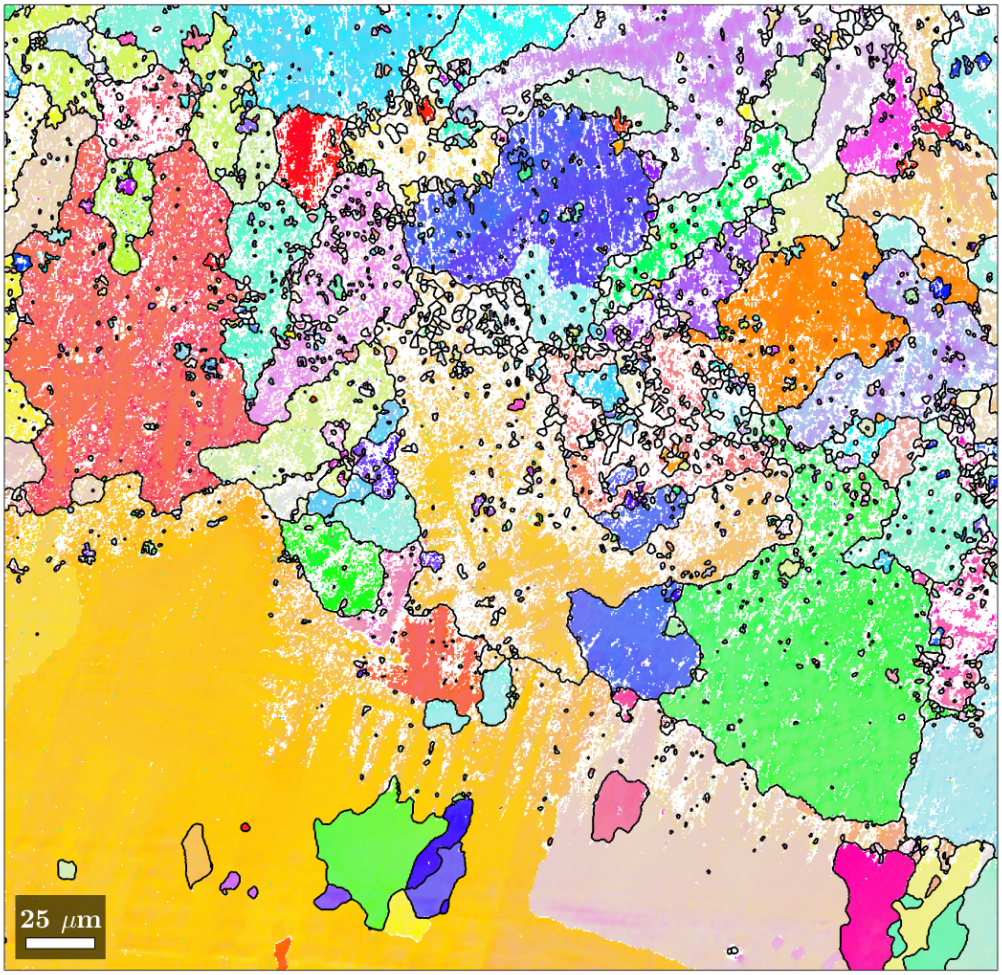

(a)

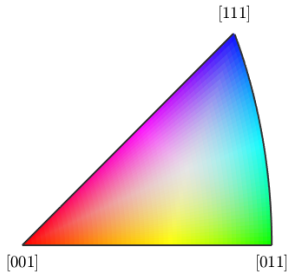

(b)

Figure 55: IPF map of a part of the interface (IN718 on top of CuAl7) with highlighted grain boundaries and projection axis parallel to the building direction. EBSD data processed by Håkon Linga.

A phase map was obtained for the highest magnified image, presented in Figure 55. The high-signal phases, both below and above the interface, have fcc structure. The dark areas from the IQ map have in this image a white colour, resulting from the low detection of Kikuchi patterns. As seen from the small orange and rosette-shaped regions, bcc phases are also present on the CuAl7 side of the interface.

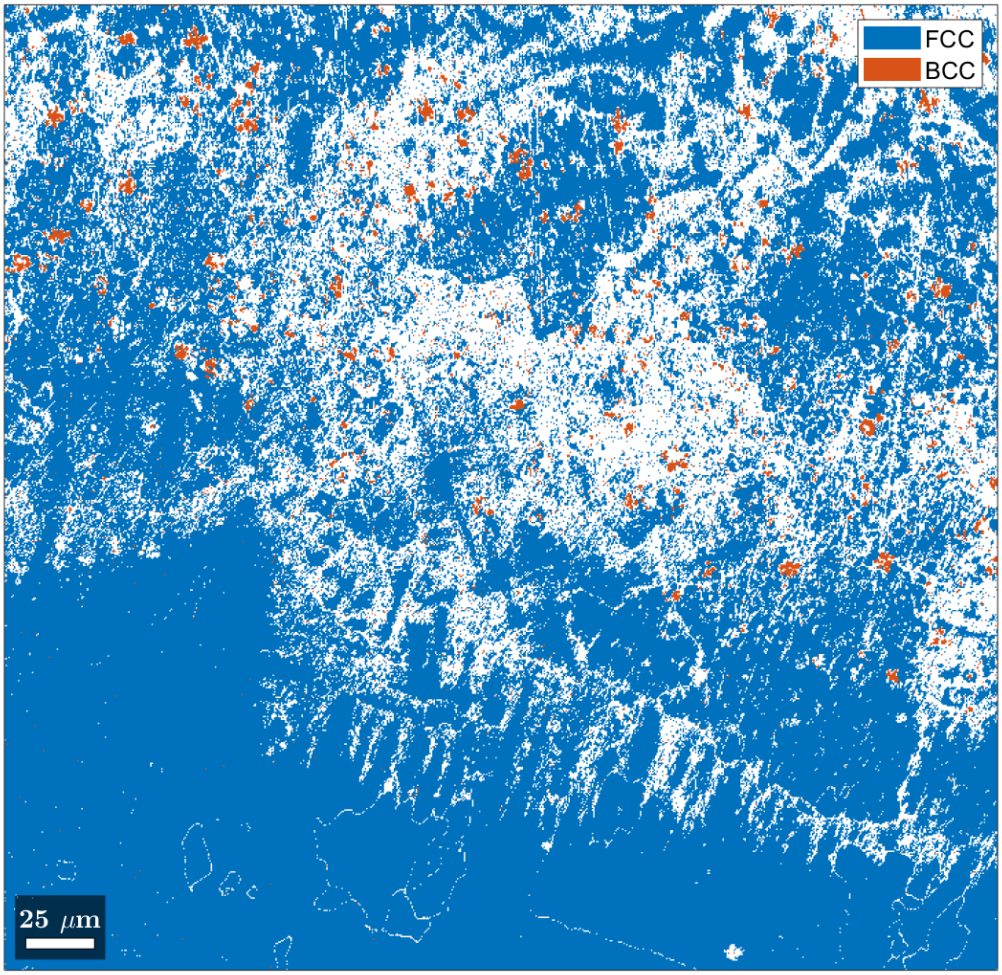

Figure 56: Phase maps showing fcc and bcc in an interface section (IN718 on top of CuAl7). EBSD data processed by Håkon Linga.

5.6 Tensile testing

In this section, the micro-tensile test results are presented and show the nominal stress-strain behaviour. Figure 57, Figure 58 and Figure 59 represent the tensile test response in IN718, CuAl7 and the interface region, respectively, with different orientations of the specimens from the as-deposited material. Names with a subscript h refer to the horizontally aligned specimens, v represents the vertical specimens and a is a 45° between horizontal and vertical alignment.

The deposition of IN718 showed a yield strength of between 650MPa and 750MPa for all specimens. The precision of the series was high, resulting in ultimate tensile strengths between 1000 and 1200MPa. The s_u was around 1100MPa for $IN718_v$, between 1000 and 1100MPa for $IN718_h$ and between 1100 and 1200MPa for $IN718_a$. Some of the samples fractured before the ultimate tensile strength. However, the yield strengths and the strain hardening curves were very similar to those which experienced necking. The strain hardening resulted in an approximately 50% increase in strength.

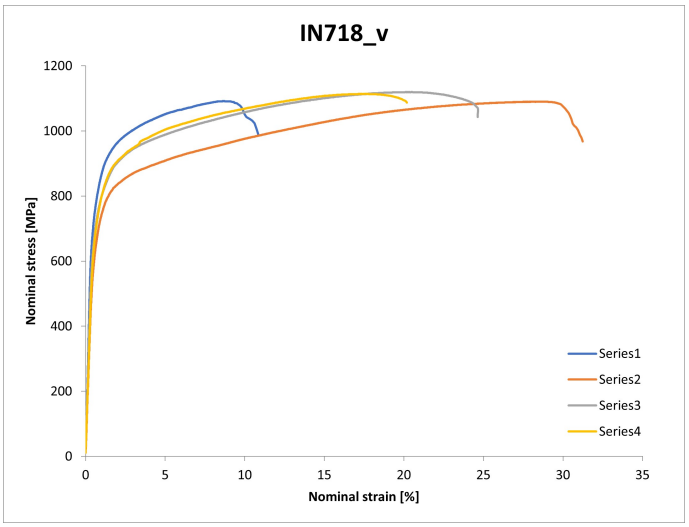

(a)

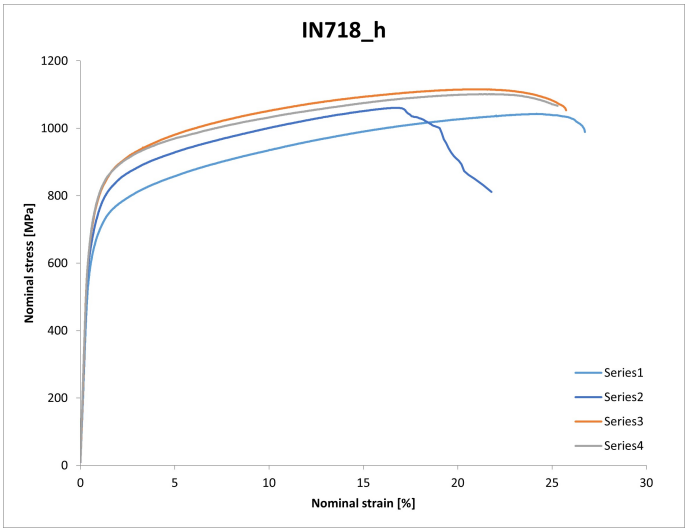

(b)

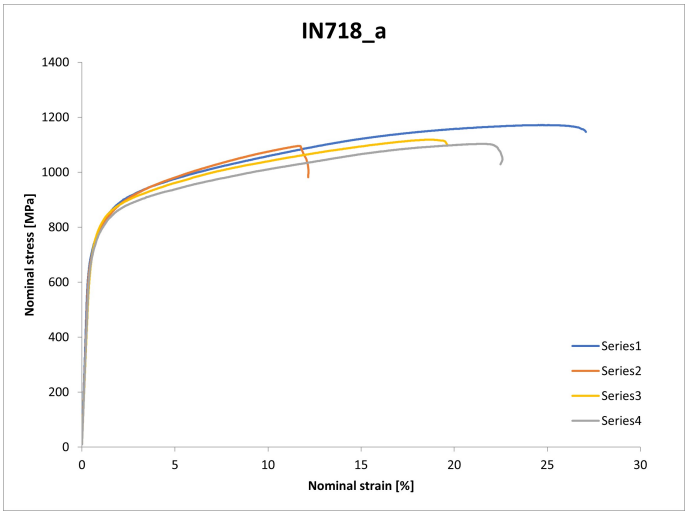

(c)

Figure 57: Nominal stress-strain curves for horizontally, vertically and angularly oriented micro-tensile specimens from IN718.

The tensile test results obtained from CuAl7 are presented in Figure 58. A lower precision was seen from these curves compared to those for IN718. In Figure 58b) and c), yield strengths of between 150 and 200MPa are obtained. Furthermore, an extraordinary strain hardening is achieved up to elongations of 50-60%. This gives an almost 100% strength increase. The $CuAl7_v$ in sample no. 2 (Figure 60 showed higher strength values and lower elongations. The specimens were not taken far from the interface, containing IN718 at one of the specimen ends. However, the gauge length was above the interface and contained only CuAl7 (including impurities from blending with IN718). The tilted specimens have a slightly higher strain than the vertical specimens, but the ultimate tensile strengths are roughly the same.

When it comes to $CuAl7_h$, a large variation in strength and ductility is obtained. Two groups can be identified, a high strength-low ductility group (Series3, Series4, 2_1, 2_2) and a low strength-high ductility group (Series1, Series2, 1_1, 1_2). The location in the specimen is known for the tests represented with dotted lines in Figure 58a but not tracked for the solid line specimens. In Section B.2 in Appendix B, EDS was performed on the samples with both known positions and unknown positions to validate their original position in the as-deposited material. It is seen that those with the highest strength contain the highest concentrations of main elements in IN718 such as Ni, Cr and Fe. The result indicates that Series1 and Series2 are the purest CuAl7 samples and are obtained far away from the interface and that Series3 and Series4 are taken closer to the IN718. See figure Figure 30 from Section 4.4.1. The tensile strength for the more Inconel-rich aluminium bronze is seen to exceed that for all the CuAl7 specimens, possessing only half of the elongation capability.

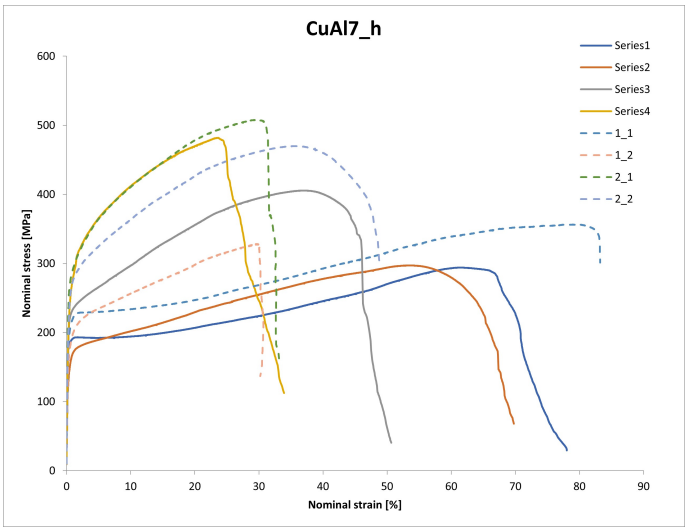

(a)

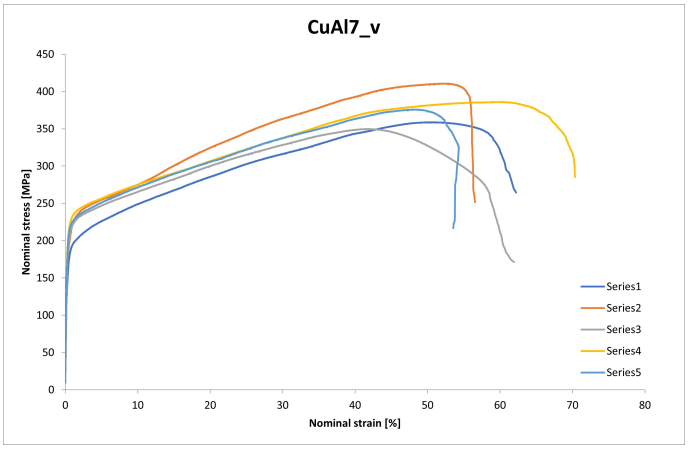

(b)

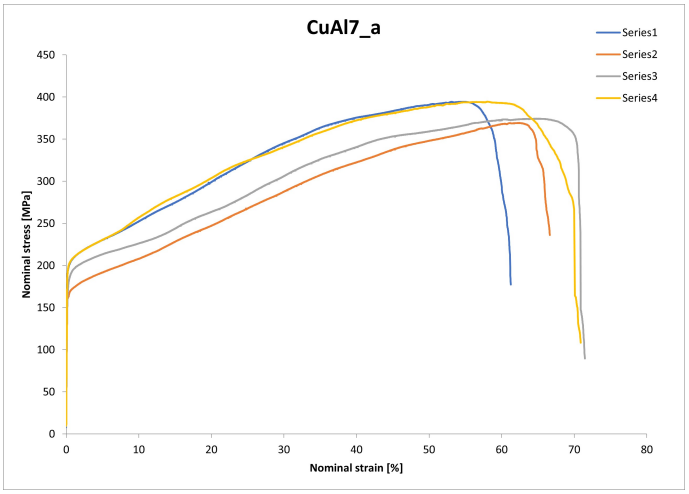

(c)

Figure 58: Nominal stress-strain curves for horizontally, vertically and angularly oriented micro-tensile specimens for CuAl7.

Tensile specimens of the interface were also obtained, having both a horizontal orientation

and a vertical orientation to the interface. Figure 59 shows the resulting stress-strain curves. In addition, vertical tensile properties of the interface in sample no. 2 were tested (Figure 60). Here, Sample2 contained more from the CuAl7 than from IN718, seen in the figure as longer elongations. It is also seen that the values for both sample no. 1 and sample no. 2 are very similar with average ultimate strengths of around 500MPa and uniform strains of 10%. Figure 59a has large variations in both strength and ductility, where the values lie between those of IN718 and CuAl7. Two horizontal specimens were also tested, giving two curves with some differences in strength and ductility. Both achieved a strain hardening of approximately 50% and a rapid reduction in strength during necking.

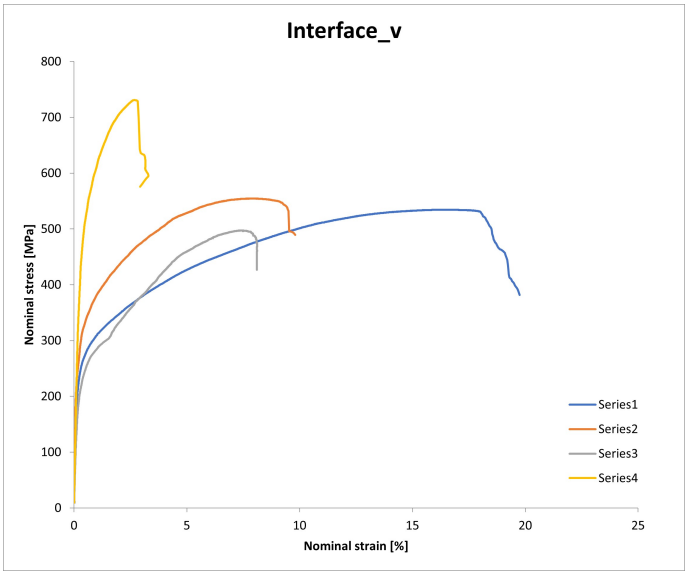

(a)

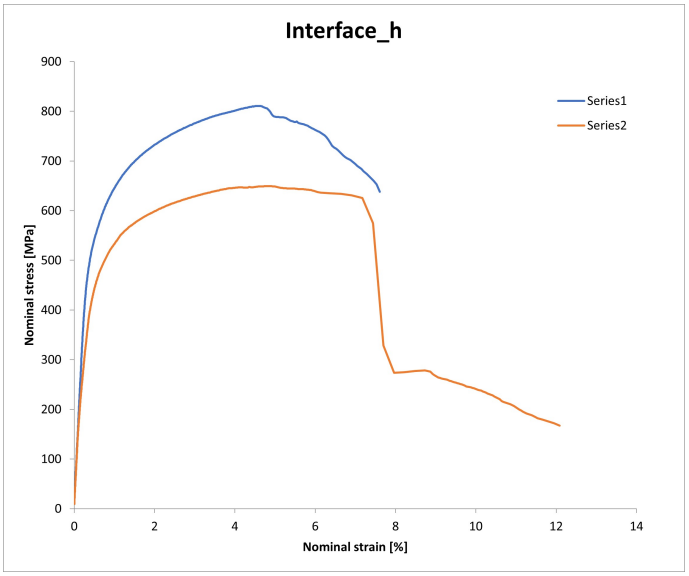

(b)

Figure 59: Nominal stress-strain curves for vertically and horizontally oriented micro-tensile specimens for the interface between IN718 and CuAl7.

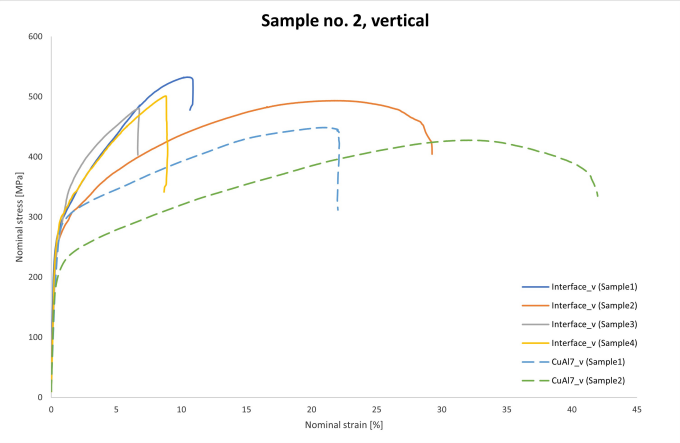

Figure 60: Nominal stress-strain curves for vertically oriented micro-tensile specimens for the interface between IN718 and CuAl7 and pure CuAl7 with vertical orientation in sample no. 2.

5.7 Fracture strain by fraction area

The fractures were examined in SEM to measure the fracture areas which furthermore gives an indication of the fracture strain value and the area reduction of the tensile specimen. Images of the fracture surfaces of selected specimens are presented in Appendix D. The fracture areas were measured using the image processing software ImageJ.

From Table 14, the measured areas are seen, including the area reduction value and the uniform strain given in per cent. As q is a measure of ductility it can be observed that the CuAl7 is the most ductile having the highest values of q with an area reduction of between 60 and 70%. $CuAl7_{h(1)}$, the specimen taken the largest distance from the interface, is observed to experience the highest decrease in area. The horizontal sample taken close to the interface, $CuAl7_{h(2)}$, has the lowest q value of the CuAl7 tests. The same tendency is seen for ε_f in Table 13. In IN718 the values range from 26 to 35%, with the tilted sample having the lowest value.

The two e_u values were obtained from calculating the stress-strain curves and measuring the uniformly deformed cross-section of the tensile specimen with a calliper in subsequent to testing. The CuAl7 specimens showed large deformations on the sides of the surface area, making it challenging to measure the exact cross-sectional area with the calliper.

Table 13: Mechanical properties in different directions of various regions of the as-built sample. v indicates vertical direction (building direction), h is the horizontal direction and a is an angle of 45°.

	Name	s_u[MPa]	e_u[%]	σ_u[MPa]	ε_u[%]
$IN718_v$	Series3	1119.9	19.8	1341.8	18.1
$IN718_h$	Series3	1115.7	20.1	1339.7	18.3
$IN718_a$	Series3	1118.4	18.1	1320.9	16.6
$CuAl7_v$	Series1	358.7	50.6	540.3	41.0
$CuAl7_{h(1)}$	1_1	356.4	78.0	634.3	57.6
$CuAl7_{h(2)}$	2_2	469.9	35.3	636.0	30.3
$CuAl7_a$	Series3	374.3	64.6	616.2	49.9
$Interface_{v(1)}$	Series2	554.5	7.5	596.2	7.3
$Interface_{v(2)}$	Series4	730.8	2.3	747.5	2.3
$Interface_h$	Series2	649.4	4.4	677.9	4.3

Table 14: Measured values for initial area, A_0, area in the uniformly deformed specimen, A_u, and the area of fracture, A_f, with calculated values for uniform nominal strain, e_u, true fracture strain,ε_f and reduction area, q.

	Name	A_0[mm^2]	A_u[mm^2]	A_f[mm^2]	e_u[%]	ε_f[%]	q[%]
$IN718_v$	Series3	1.06	0.90	0.69	17.6	43.2	35.1
$IN718_h$	Series3	1.04	0.81	0.69	28.5	40.5	33.3
$IN718_a$	Series3	1.00	0.87	0.74	14.4	30.3	26.1
$CuAl7_v$	Series1	1.02	0.71	0.36	43.1	104.5	64.8
$CuAl7_{h(1)}$	1_1	1.07	0.67	0.32	58.9	121.3	70.3
$CuAl7_{h(2)}$	2_2	1.04	0.77	0.40	35.7	96.4	61.8
$CuAl7_a$	Series3	1.03	0.71	0.46	45.7	80.8	55.4
$Interface_{v(1)}$	Series2	1.00	0.85	0.61	16.7	49.0	38.7
$Interface_{v(2)}$	Series4	0.96	0.94	0.83	2.1	14.5	13.5
$Interface_h$	Series2	1.40	1.04	0.76	34.2	61.0	45.7

5.8 Fracture surfaces

The fracture surfaces were examined with SEM using higher magnification. Dimples were observed in CuAl7. In IN718, both small dimples and more brittle material were detected. The vertical specimen showed a fracture surface with dimples oriented in a random manner. Some pore formation was also seen. Inside the dimples, a different phase was observed. In the horizontal and angular oriented specimens a strong pattern-like structure was found. The dimples were aligned in a given direction. The other phase was also seen between the dimple structure. Figure 61a, b and c show the fracture surfaces of some of the horizontal tensile specimens from IN718, CuAl7 and the interface, respectively. All fracture surfaces

are presented in Appendix D together with magnified images of their characteristic surface morphology.

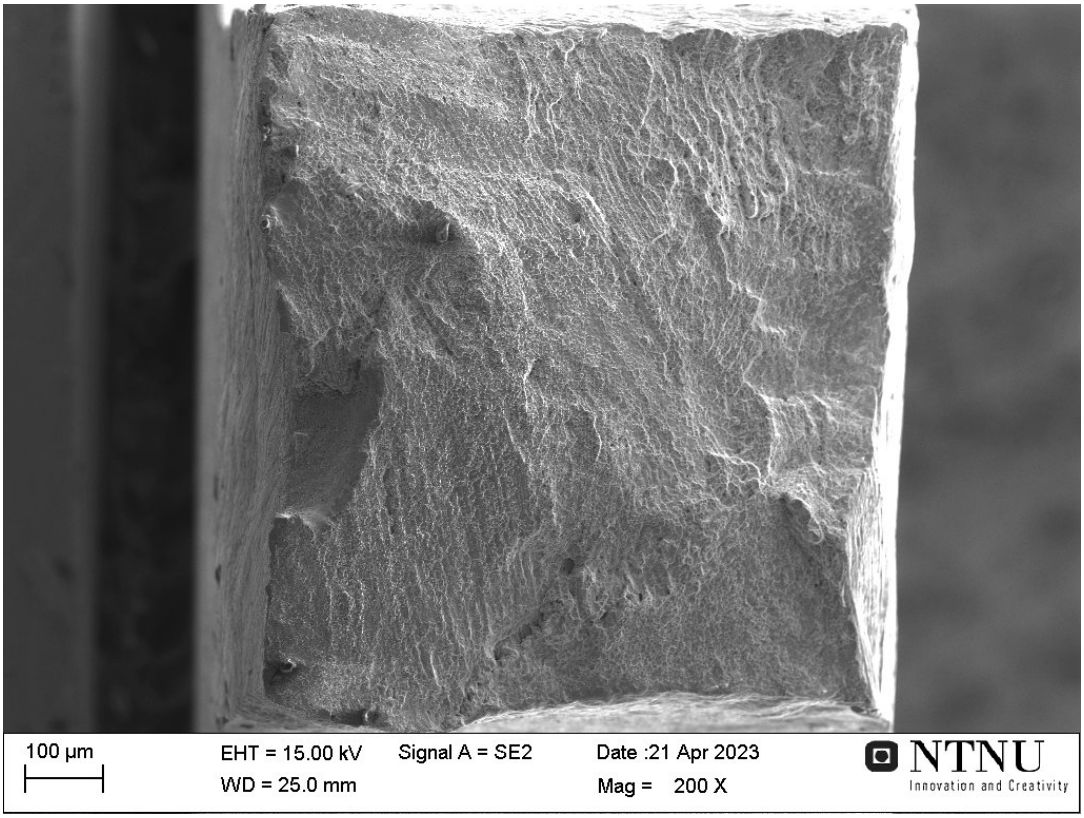

(a) $IN718_h$.

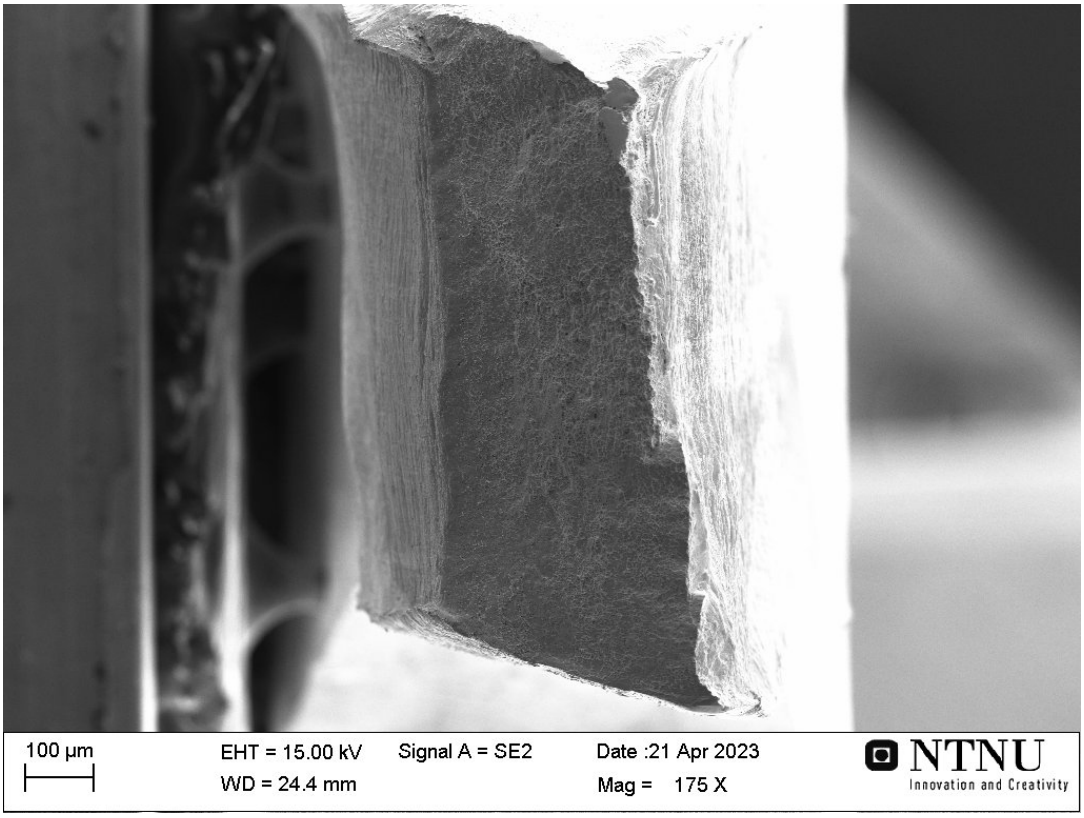

(b) $CuAl7_h$.

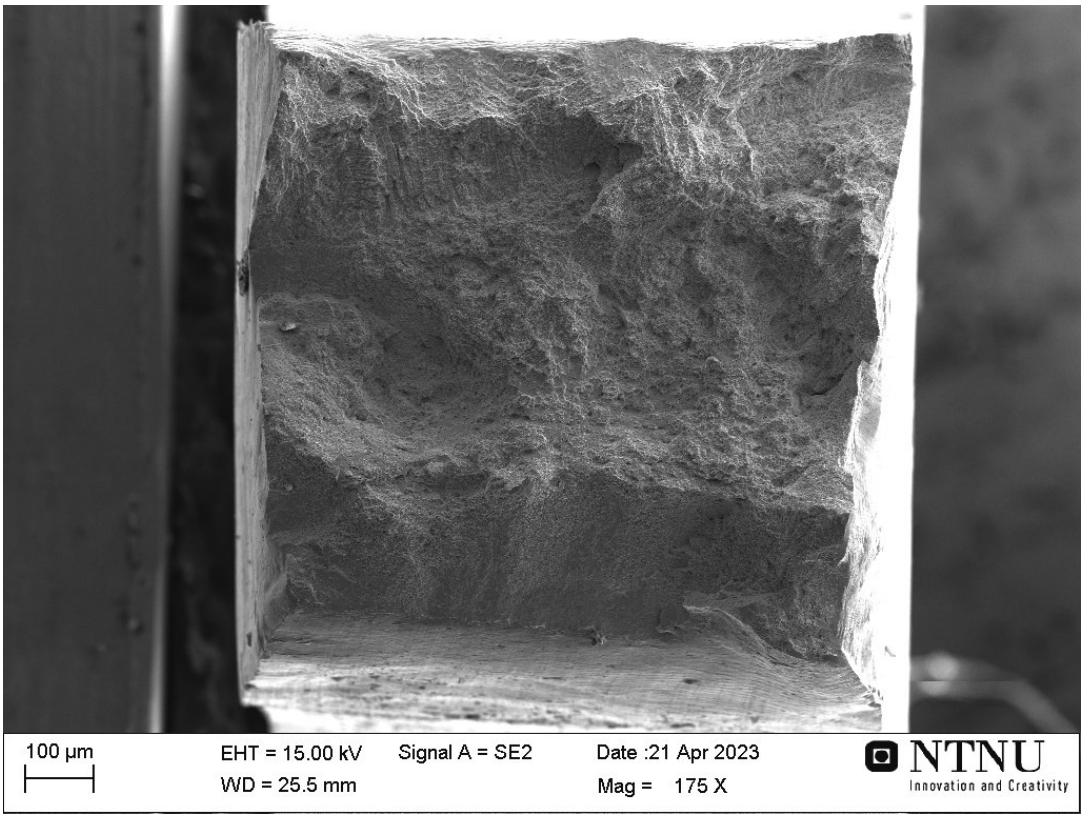

(c) $IN718/CuAl7_h$ (interface).

Figure 61: SE images of the fracture surface from selected samples.

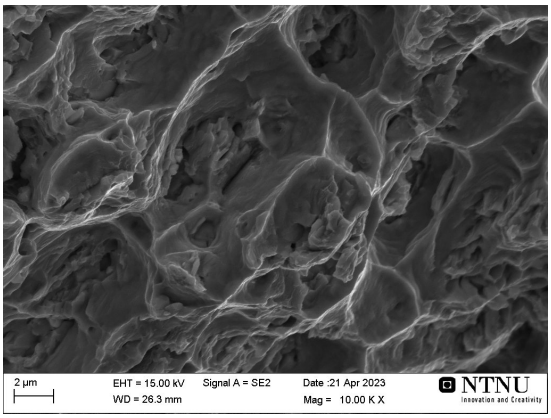

(a) $IN718_a$.

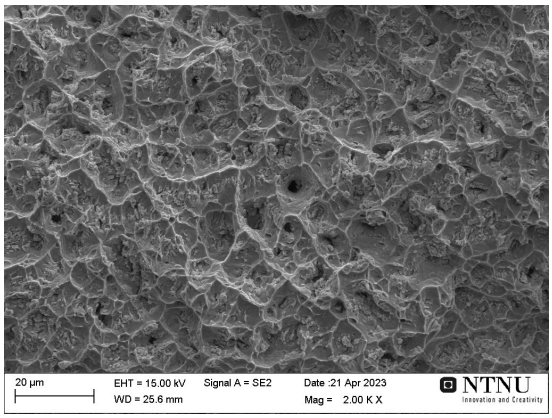

(b) $IN718_v$.

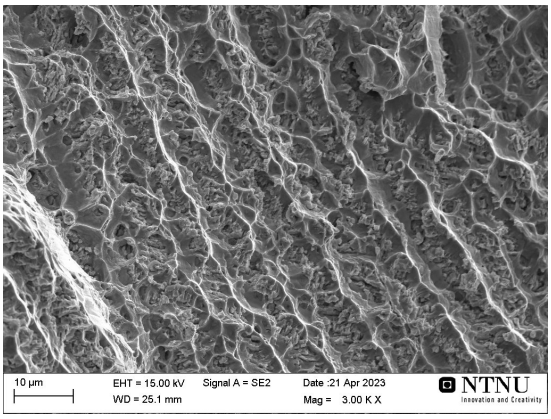

(c) $IN718_h$.

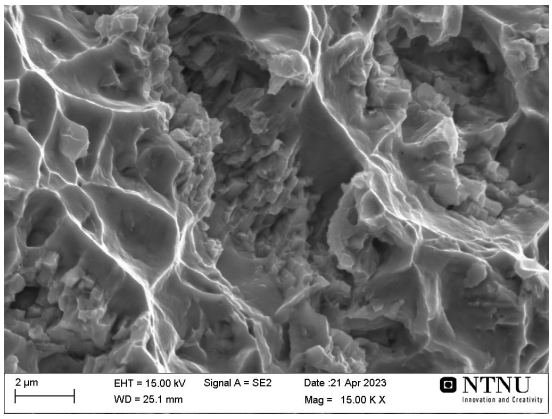

(d) $IN718_h$.

Figure 62: SE images zoomed in on the fracture surfaces from the IN718 specimens with different orientations.

5.9 Hardness testing

Vickers hardness tests were performed on the cross-sectioned polished sample. Figure 63 shows the hardness profile across the bimetallic interface, with IN718 on the negative side of the interface and CuAl7 on the positive side of the interface. HV0.5 was used to do macro indentation with distances shown in Appendix E, satisfying the standards for testing (ISO 6507 2018). In addition, microhardness tests were carried out a short distance from the interface. Both HV0.1 and HV0.05 were used to measure the hardness values in these regions. As seen from the figure, the two materials have a large difference in hardness. IN718 has values around 300 HV0.5, while CuAL7 is measured to be around 100 HV0.5. In the interface, a leap up to approximately 400 HV0.5 is obtained, having large variations in the values so close to the interface. The hardness decreases rapidly towards CuAl7, but the slope becomes lower with larger distances.

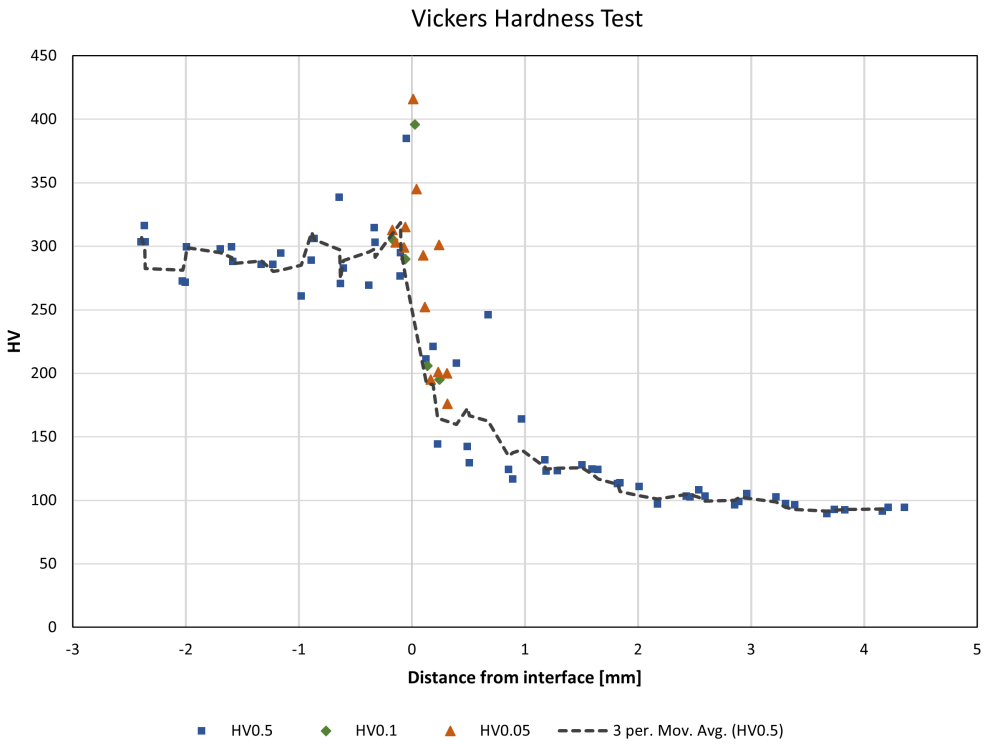

Figure 63: Measured Vickers hardness across the interface.

As hardness indicates the strength of the material, given by Equation 12, this relationship can be investigated in the different materials in the as-deposited part. In Table 15 gives a rough indication of the proportionality constant from the equation based on approximate values of the hardness, the yield strength (σ_0) and the ultimate tensile strength (s_u).

Table 15: Calculations of the constant of proportionality relating hardness and strength (Equation 12).

	HV0.5	**HV**[MPa]	σ_0	s_u	**H**/σ_0	**H**/s_u
CuAl_v	90	883	200	400	4.4	2.2
IN718_v	300	2942	700	1100	4.2	2.7
interface_h	380	3727	500	750	7.5	5.0

5.10 EDS linescan across interface

Figure 64 illustrates a line-scan over the interface, from IN718 to CuAl7. It is seen that the interface between the two alloys is highly distinctive, where the regions experience a rapid change in element content from one side to the other. However, looking at Cu in Figure 64b and Al, Ni, Fe, Cr and Nb in Figure 64c, a slight transition is experienced from the Inconel interface and through the aluminium bronze.

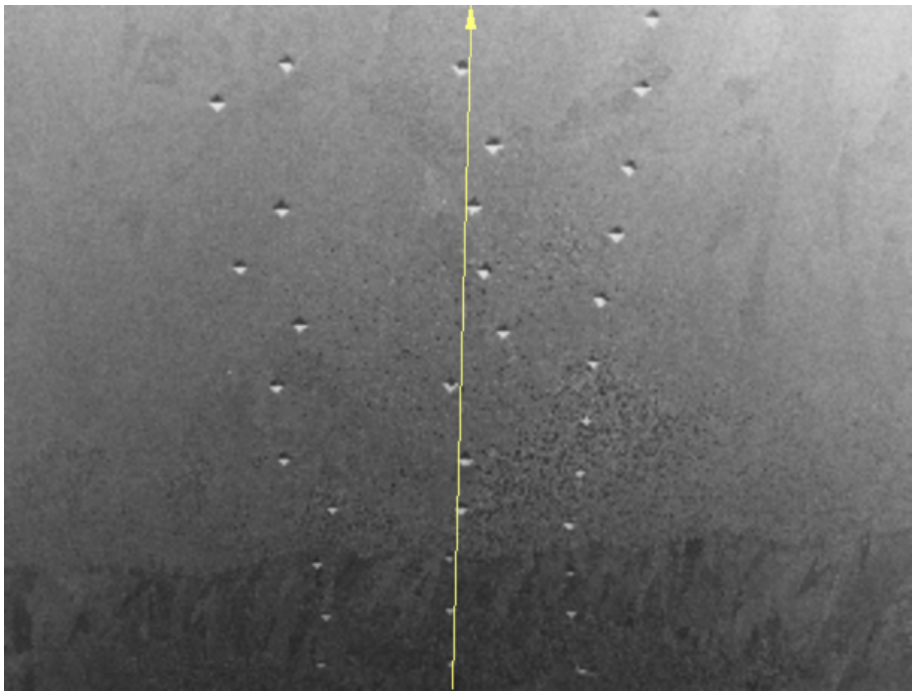

(a)

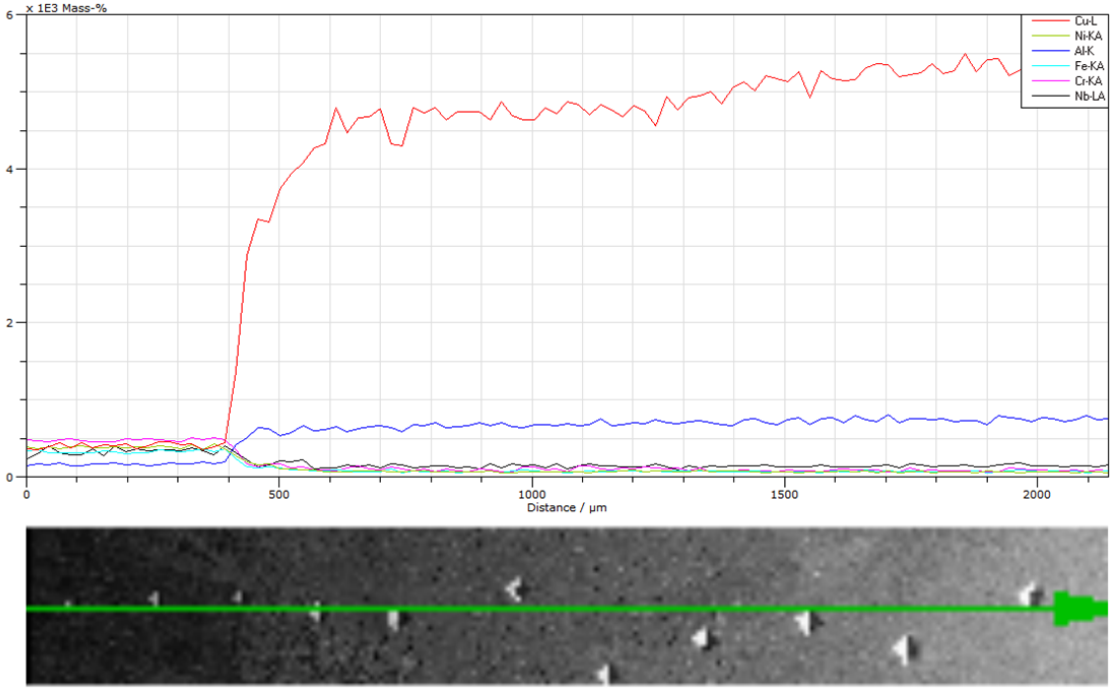
x 1E3 Mass-%
6
4
2
0
0
500
1000
1500
2000
Distance / µm
Cu-L
Ni-KA
Al-K
Fe-KA
Cr-KA
Nb-LA

(b)

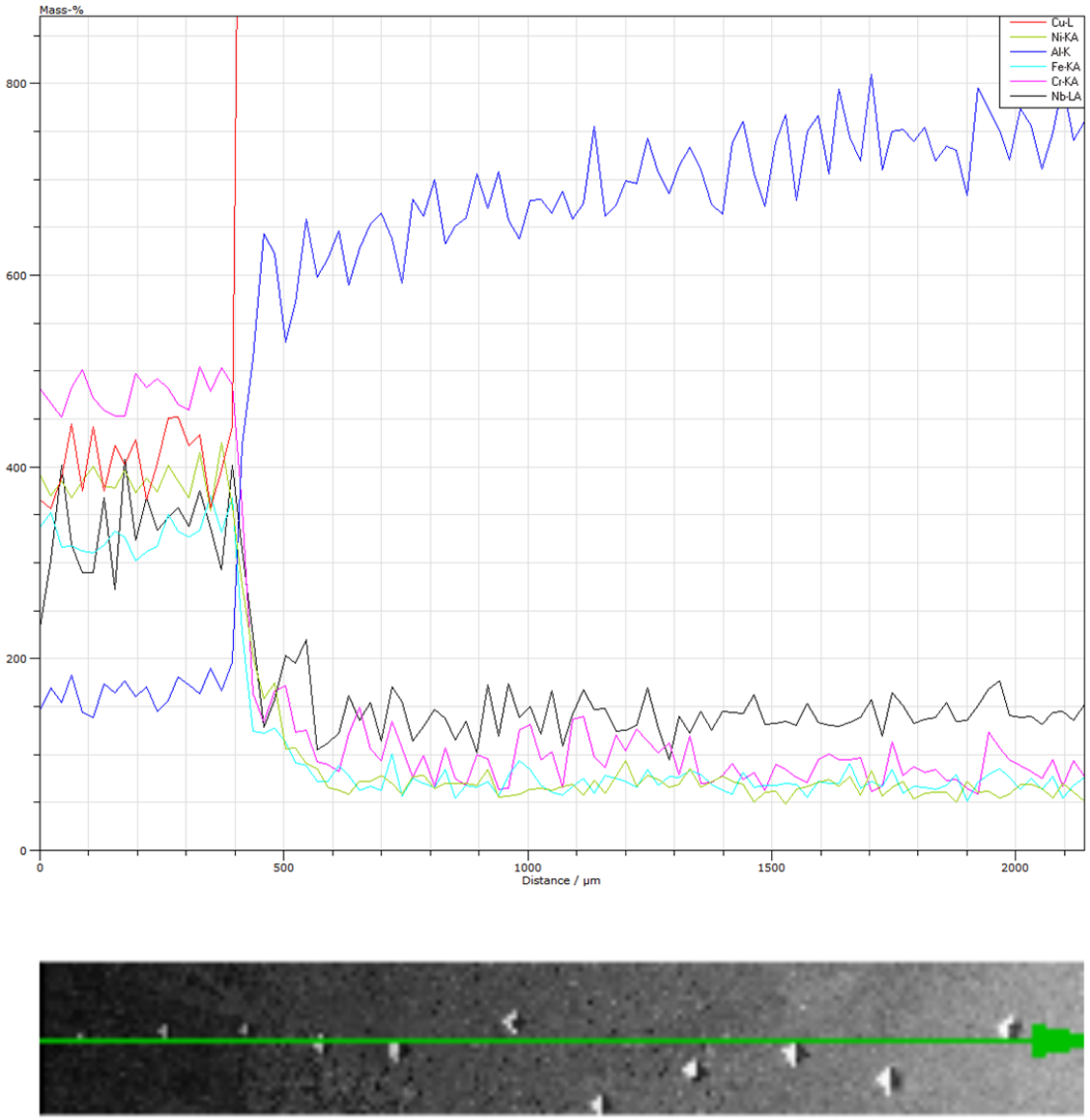

(c)

Figure 64: Line scan across the interface obtained from EDS. a) shows a picture of the sample area and the scanning line, b) shows the EDS signals over the surface and c) is a zoomed-in region of the plot in b).

6 Discussion

Blending between IN718 and CuAl7

Bimetallic additive manufacturing of CuAl7 on top of a multi-layered part of IN718 resulted in adequate fusion between the two alloys, where strong metallurgical bonds have been formed. This was also reported in A. Marques et al. 2022. Both have fcc structure which improves the compatibility between the two materials. This results in a smooth interface. The LOM images in Section 5.2 showed no form of macroscopic defects in terms of lack of fusion or pores. The interfacial area in the images indicated the presence of a large fusion zone, with dark particles present at several millimetres above the interface. From the LOM images (Figure 40), no defects were seen in the pure alloys either. This means that the chosen process parameters provide a successful multi-layer deposition of CuAl7 on IN718. However, as seen from the raw material part in Figure 28, a high surface finish is not obtained for CuAl7 with many layers. This may be due to the formation of unstable melt pools and can further be explained by the high cooling rates present which results in poor adhesion to the previously deposited layers. The heat will not be accumulated in the same way as in IN718, since the heat conductivity is much higher in aluminium bronze. As a result, the air around the deposited part will behave as a heat sink and increase the cooling rate in and around the melt pool. Also, a high reflection of the laser beam from the aluminium bronze is experienced, making it challenging to supply sufficient heat input to the melt pool. Preheating the material before the deposition was therefore necessary in addition to a high hot-wire power.

Mechanical properties based on tensile testing and hardness testing

The results obtained from the mechanical testing indicate a strong bonding between the IN718 and CuAl7 from the LMWD process performed in these experiments. In Section 2.5.1 the mechanical properties of as-built IN718 were presented. The material was reported to have yield strength of around 540MPa, a tensile strength of approximately 830MPa and an elongation of 25%. In the micro-tensile testing carried out in this project, a yield strength of more than 600MPa and a tensile strength of over 1100MPa were registered. The elongation was measured to be between 20 and 25% by the tensile test machine. The stress-strain results in Figure 57 show high precision. A minority of the samples fractured before reaching the ultimate tensile stress. This indicates the presence of some defects inside the tested material or an unsuccessful mounting of the sample. The hardness values obtained in Figure 63 represented the same tendency as the tensile tests, with IN718 showing a three times higher Vickers hardness value than CuAl7. In IN718, the average value was stable around values of 300 HV0.5, with some local variations. These variations may originate from strengthening mechanisms such as intermetallic phases or grain size differences. Furthermore, in Section 2.4.2 reports of texture influencing the mechanical properties were presented. Figure 7 showed the stress-strain behaviour in both the transversal (horizontal) direction and the longitudinal (vertical) direction. In the experiments carried out, this tendency was not clearly seen. The fracture strain was obtained to be somewhat higher for the vertical specimen, having an orientation parallel to the building direction, with about the same ultimate tensile strength. The error given for the tensile strength in Table 2 seems to apply also for increased strengths achieved in these experiments. The differences in the series for the respective sample orientations could, however, lead to other results, as the sample amount should be higher in order to

arrive at a final conclusion.

Tensile behaviour dependent on distance from interface

In the tensile test for CuAl7, a wide range of ductility and strength was discovered in the horizontally oriented specimens, while a common tendency was seen in the horizontal and tilted specimens. The horizontal specimens were achieved from two different distances to the interface, as described in Section 4.4.1, resulting in different concentrations of elements found in IN718. The difference in strength and strain may be caused by the difference in chemical composition, including other factors such as grain size, phases, texture and particles, resulting in strengthening mechanisms described in Section 3.3. From the EDS line scan in Figure 64 the concentration in the Al bronze is analysed up to a distance of $1500\mu m$ from the interface. It is seen that elements from IN718 have been transferred into CuAl7 with a relatively stable concentration of Ni, Cr, Fe, and Nb. Mo is also present but was not included in the analysis. It is also seen that the Cu concentration is increasing up to this distance.

The tensile tests most affected by the distance from IN718 are the horizontally oriented specimens. Strengths ranging from 300MPa to 500MPa and nominal uniform elongations from 25% to 80% were seen in these tests. The EDS analysis of $CuAl7_h$ obtained from both a known position and an unknown position in the as-deposited material is presented in Section B.2. As described in Section 5.6, the samples contained differences in especially Ni, Fe, and Cr. In the samples with known positions, the two furthest away from the interface ($CuAl7_{h(1)}$) contained low concentrations of these elements, while the other two ($CuAl7_{h(2)}$) had higher concentrations. The $CuAl7$ samples with unknown positions showed the same effect as described. The EDS analysis of Series1 and Series2 indicates they are taken from a larger distance from the interface, containing more Cu and Al and less Ni, Cr and Fe. From the stress-strain curves (Figure 58a), Series1, Series2 and $CuAl7_{h(1)}$ (1_1 and 1_2) are seen to have lower strength and higher ductility than the other four $CuAl7_h$ samples. Furthermore, $CuAl7_{h(1)}$ (1_2) has properties of a place between the two groups, which also can be explained by its higher Ni than the other CuAl-rich samples. The hardness profile from Figure 63 showed the same tendency, with a decreasing hardness further away from the interface.

From Section 4.4 it was stated that $CuAl7_{h(2)}$ was taken only 3.5mm away from the interface. The hardness at this distance is shown to be around 100 HV0.5. Unfortunately, no further testing was performed inside CuAl7, but the tensile tests showed a clear relationship between the strength and the distance from the interface. It is therefore likely that the hardness values also decrease further inside CuAl7. The differences in tensile strength for the horizontal specimens may be due to the solid solution strengthening (interstitial or substitutional atoms) as elements from the IN718 could travel along the building direction as new CuAl7 layers are being deposited. The impurity atoms will then create stress fields in the matrix lattice, thus increasing the material strength in the absence of other strengthening mechanisms except for twinning and strain hardening. Another marking is the difference in hardness when comparing the aluminium bronze value with the value from the producer (126HV) (UTP Maintenance 2023). The manufacturing procedure is not stated in the classification papers, and it is likely the processing of the materials was different, making the values non-comparable. It still gives an indication of the hardness of the material.

The tensile tests from the interface were presented in Figure 59 (sample no. 1) and

Figure 60 (sample no. 2). Ideally, the vertical specimens should contain equal amounts of IN718 and CuAl7 in the parallel gauge length in which the strength was measured. However, due to the challenges regarding cutting and an interface being not completely parallel, in addition to different amounts of IN718 elements in the CuAl7 part, the tensile tests exhibited various strengths and elongations. Since CuAl7 has been shown to be the weakest material, the fractures took place at the CuAl7 end of the tensile specimen. This made it difficult for the laser extensometer to place the two digital marks (fixing the gauge length) on each side of the fracture without encountering the area outside the parallel area (i.e. in the radius of the tensile specimen). Since the material in the radius has a larger cross-section area the strain values will differ from the real values. $Interface_v$ Series2 had the fracture area outside the test length, missing the necking strains. This was not the case for the other specimens. The elongation results from the vertical interface tests are therefore not accurate. However, the stress measured is still valid as this value only depends on the stress response from the material. Series 4 has a much higher strength than the other tests. It was observed that the IN718 region in the sample was a few millimetres longer than that of CuAl7, suppressing the properties of aluminium bronze. As the strengths of the vertical specimen lie between 500MPa and 730MPa, the close-to-interface CuAl7 shares properties with IN718, making it a stronger but less ductile material. Furthermore, the two horizontal specimens show a similar tendency. The strain hardening is, however, not as dominating as that for the vertically aligned specimens due to fractures in both IN718 and CuAl7 instead of in only CuAl7. It was challenging to obtain the same amount of the two materials in the parallel area of the samples due to topographic differences in the interface. This implies that the test specimens probably are more susceptible to local chemical variations. The strains are much lower than for both pure IN718 and CuAl7, indicating a more brittle material. Comparing the e_u for all the tests, it is clear that the interface exhibit lower strains. Step-like curves are seen in Figure 59b, especially for Series2. The fracture did not go outside the extensometer, which means that the instrument detected stress in the material after the first stress reduction. An explanation of this can be that IN718 fractured before CuAl7 and that CuAl7 continued to strain after the fracture of IN718.

The tensile tests of CuAl7 revealed an extraordinary strain hardening behaviour. This was also reported by the manufacturer (UTP Maintenance 2023) in Table 5. The values were shown to be quite accurate compared to these experiments, with a strain hardening of around 100%. In fcc metals, twinning is commonly seen as an essential strengthening mechanism, as described in Section 3.3.5. In LMWD and other additive manufacturing techniques, the material is heated, making it susceptible to the formation of annealing twins. As the material is subjected to mechanical deformation after undergoing complex thermal cycles during manufacturing, these twins are likely to form. Deformation hardening is dependent on lattice irregularities, causing a pile-up of dislocations which contribute to the increased strength. Since there are no particles forming in the homogeneous *alpha* region, theoretically, there will be no strengthening contribution from this mechanism. Solid solution strengthening is present, but this will only reduce the dislocation motion to a limited extent. However, the strengthening mechanism from the boundaries in the lattice will have a notable effect. The grain size in the CuAl7 from Section 5.2 is shown to be several hundred micrometres in size, which indicate a low Hall-Petch effect from Equation 11 in Section 3.3. However, twinning boundaries will have a considerable Hall-Petch effect as they inhibit dislocation movement prior to plastic deformation.

The investigation of the fracture areas and tensile properties in Section 5.7 yielded a large variety of strengths and ductility values. For high-purity CuAl7, true fracture strains of more than 100% were observed. The large grains and the lack of strong strengthening

mechanisms are thought to be the reasons for this. The fracture areas were dominated by small dimples, which strongly indicate ductile fractures, seen from Appendix D. Small voids were seen inside the dimples, the initiation point of void growth. In the fracture surfaces from the vertical interface tensile tests, small dimples were present as in CuAl7. However, some parts of the surface revealed flat areas. The ductility in these areas is therefore lower, indicating the presence of strengthened phases. The size of the areas is almost the same as the Ni-rich dendrite arms seen in the Cu-rich matrix (Figure 45), which could imply that these areas are equiaxed IN718-rich dendrites reducing the ductility of the phase. In the fracture surface of the horizontal interface specimen, a clear transition is seen between the upper part of the (IN718) and the lower part (CuAl7) (Figure 61c and Figure D.1). In the IN718-rich part, coarse and aligned dimples are seen and finer dimples are observed in the CuAl7-rich part, indicating the differences in ductility. An uneven fracture surface is also obtained due to the strength difference between the two materials. A more bent area in CuAl7 indicates that the aluminium bronze has experienced higher strains than IN718. This is also seen from the stress-strain curves (Figure 59b).

Phases in as-deposited material based on microstructure imaging and EDS results

The interface region was shown to contain multiple types of dendrites and phases or particles with different chemical compositions. In IN718, a strong alignment of dendrites was observed, growing from equiaxed grain zones in the bulk material. The equiaxed grains may arise from the reheating of previous layers by activating the hot-wire system, as reported in Bombach et al. 2018 (see Section 2.2.1). The direction of the dendritic structure was along the building direction (upwards in Figure 42 and Figure 44) meaning the dendrites follow the maximum heat flow direction. Columnar grains, a common observation in AM materials, are then present. Some deviations in orientation were observed, leading to non-parallel dendrites. This indicates various maximum heat flow directions and easy growth directions determined by the behaviour of the melt pool, and competitive grain growth has developed. Between the dendrites, in the interdendritic zones, a bright phase is observed in the backscatter electron images, meaning it consists of heavy elements. As the EDS results also indicate, this phase is governed by elements having a high atomic number, such as Nb and Mo. The Ti content is also higher in this phase compared to the dendrite composition. This indicates the presence of Laves phase. Laves was described as a common phase observed in Inconel alloys, and it is widely reported in additive manufacturing of IN718 (Section 2.5.2). In the analysis of fracture surfaces, aligned structures were seen in the IN718 tensile specimens (Figure 62). Adjacent layers of two different phases are observed for the horizontal tensile specimens, with a distance of a few micrometres between each phase. The BSE images in Figure 42 indicate that these layers arise from the columnar dendritic structure in IN718. The fracture surface reveals dimples in one phase and another phase of brittle nature in the other. The latter phase is most likely the Laves phase, as this phase is known for its often undesired brittleness. As Ni exhibit high ductility, the dimpled phase will be the IN718 γ dendrites. This, however, did not show any considerable worsening of the tensile behaviour.

In the interface region, IN718 dendritic structures were seen across the bimetallic boundary (Figure 41, Figure 42 and Figure 53). From the EBSD results in Section 5.5, the IQ map and the IPF maps showed weak signals from the aluminium bronze regions. This may be due to the challenges involving the preparation of the material. Many preparation techniques were tested, but due to the material property differences in IN718 and CuAl7,

a well-polished surface in the aluminium bronze was difficult to obtain. However, this emphasizes both the IN718-rich areas and the CuAl7-rich areas. The equiaxed dendrites are then seen near the interface but also several hundred micrometres away from the bimetallic boundary. These were shown to contain a high fraction of elements in IN718 such as Ni, Fe, Cr, Nb, and Mo but also a high concentration of Cu was detected in addition to some Al (Figure 49). The secondary dendrite arms are very visible in both the LOM pictures and the images obtained by SEM. The EDS samples from a coarse equiaxed dendrite in the blending zone showed the same result as for the IN718 dendrites, indicating IN718-rich equiaxed dendrites. Since IN718 has a higher melting point than CuAl7 (Figure 37 and Figure 38), IN718-rich dendrites will then form in the bimetallic liquid prior to the solidification of the Cu-rich melt.

In the periphery of the equiaxed dendrites, micrometre-scale particles could be observed encircling the dendrites. This was seen between the columnar dendrites and the equiaxed dendrites in Figure 43c) and d). It was also observed further up in the aluminium bronze (Figure 46c) and d)). The EBSD pole figures in Section 5.5 showed grains being identified on both sides of the bimetallic boundary. The equiaxed dendrites from the IQ maps (Figure 53) were identified as part of a larger grain, containing both the dendrites and the surrounding Cu-rich matrix. As the IPF with highlighted grain boundaries (Figure 55) includes both equiaxed dendrites and the inter-dendritic regions in the same grains, it indicates that the Cu-rich matrix around the dendrites has the same crystallographic structure as the dendrite. This is possible because both Ni and Cu have fcc structures and are completely miscible, seen from Figure 56. The small particles surrounding the dendrites are thought to be present on the grain boundaries. The EDS analysis showed varying results, and due to the small dimensions of the particles, the signals from the surrounding matrix and particles underneath the surface would influence the quantitative results. Therefore, the EDS values will be utilized as a more qualitative analysis tool. Sample 9, 28 and 29 from Section 5.4 all indicated a high Al content, larger than the initial alloy content. They also had high concentration values in Ni. The Cu content was very different, but can be explained by the varying depth of the particles. Also, the Cr and Fe values were not showing the same tendency. The plate-like structure of the particles and their chemical nature indicates the presence of NiAl κ_{III}/κ_V.

The observed white particles have a high concentration of elements with a high atomic number. The results from the EDS showed a high content of Nb and Mo, and it is easy to believe this is the Laves phase, as observed in IN718. Both Ni, Cr and Fe are highly represented, which implies the formation of $(Ni, Fe, Cr)_2(Nb, Mo, Ti)$. Comparing backscatter electron images and the phase map shown in Figure 56, the particles are observed to match the positions of the bcc grains. As Laves has a complex crystal structure, it is difficult to arrive at any conclusion whether it is the Laves phase or any other phase having the bcc structure. Furthermore, dark globular particles were observed in the upper region of the blending zone (Figure 46 and Figure 47). These consisted of mostly Cr, Fe, and Ni. The particles may remind of κ_{II} but they are not reported to contain Cr, especially not in such high concentrations. Another feature to be investigated is the coarsening of the equiaxed dendrites in the compositional layer, as presented in Figure 45. From a few hundred micrometres from the interface, the dendrites transformed from being smooth to having a coarser structure, as seen from Figure 46. This phenomenon can be explained by a reheating of the material after the solidification of the equiaxed dendrites. The particles formed are observed to have grown in a specific orientation. The EDS results indicated high concentrations of Ni, Al, and Cu. From Orzolek et al. 2022 it was reported that the concentrations of the κ phases also contained considerable amounts of Cu (between 13 and 26%, depending on the phase). This could indicate that the sharp plate-like particles

observed in the IN718 dendrites are a κ phase, growing from the Cu-rich matrix into the IN718 dendrite. The presence of the κ_{IV} has been reported in additive manufacturing of NAB (Orzolek et al. 2022), but these were not seen in this experiment. As they grow inside α grains and are seen on the nano-scale in AM, this phase may only be seen with the transmission electron microscope (TEM).

Influence from the microstructural features on the mechanical properties of the interface

The interface proved to exhibit high hardness values. There are many strengthening mechanisms that may contribute to this. The Hall-Petch effect is definitely a contributor, as the blending zone has a chaotic structure with many small grains of only a few tens of micrometres (Figure 55). In the CuAl7 bronze, on the other hand, it was observed grains of several hundreds of micrometres. Particle strengthening is also contributing to the high hardness. The wide range of particle sizes, including possible nano-scale particles inside the grains, strengthens the material by retarding the motion of dislocations during plastic deformation as described in Section 3.3.4. As additive manufacturing implies high cooling rates and non-equilibrium conditions, it is likely that some degree of super-saturated solid solution is present in the material. As this creates a stress field around interstitial or substitutions atoms in the crystal lattice, dislocation motion will be inhibited. In the Cu-rich matrix, Ni atoms will behave substitutionally, while small atoms such as Al will take up interstitial sites in the matrix. Annealing twins may also be present in the interfacial zone, increasing the Hall-Petch effect. All these contributions are the main reason for the high-strength interface between IN718 and CuAl7. The hardness values are also seen to have large differences over very short distances. The reason is probably local differences in the microstructure. Grains and particles of various sizes were seen, which give different strength contributions and also hardness values.

7 Conclusion

The main objective of the project was to characterize the microstructure, the chemical composition and the intermetallic phases present in, and at a short distance from, the bi-metallic interface of additively manufactured CuAl7 on top of IN718. LOM was used to address material defects, while SEM was used for microstructure analysis with BSE imaging, EDS and EBSD. Furthermore, the mechanical properties such as hardness and tensile strength and ductility of the as-deposited material were investigated. The following conclusion can be drawn on the basis of the obtained result:

- A well-blended interface with strong metallurgical bonding between IN718 and CuAl7 was achieved.
- Equiaxed dendrites in the Cu-rich melt were obtained, containing mostly elements from IN718. Fcc grains were seen in the blending zone, consisting of equiaxed dendrites and CuAl7-rich matrix. A good compatibility between the two materials was therefore obtained.
- Columnar dendrite growth in the building direction and intermetallic Laves phase were observed in IN718, with continued growth into the deposition of CuAl7. The anisotropic structure was not shown to influence the tensile properties in any significant amount.
- CuAl7 exhibited large uniform elongations resulting in a high strain hardening response. The effect is thought to be possible mainly due to annealing twins formed during AM.
- Small grains were observed in the blending zone while larger grains were seen in the pure alloys. This was shown to have a strengthening effect on the interface region with obtained hardness values of 400 HV0.5.
- A diverse multitude of particles were obtained in the blending zone. The Rosette-like Laves phase particles were frequently observed at various distances from the surface. Several κ phases were also seen. These particles are also thought to have a strengthening effect on the bimetallic boundary.

Further work

Based on the results and the discussion of this thesis, some further work needs to be performed to fully understand the mechanisms regarding the strengthening and the formation of the different phases observed. Atom probe tomography and transmission electron microscopy can be used to do characterizations of nano-scale particles and different phases. In addition, more research is needed in the field of CuAl7 deposition onto different substrates as the heat conductivity can be advantageous in other applications. Some initial experiments were performed during this project in LMWD of CuAl7 on a carbon steel substrate. The results are shown in Appendix F. Furthermore, heat treatment of the additive-produced materials is needed for optimizing their properties in terms of removing detrimental phases, releasing residual stress and forming new desired phases.

Bibliography

Aas, Magnus Lydvo (2022). 'A parametric study of Inconel 718 formed by laser metal wire deposition'. In: *Specialization project (unpublished work)*.

Abioye, T., J. Folkes and A. Clare (2013). 'A parametric study of Inconel 625 wire laser deposition'. In: *Materials Processing Technology* 213, pp. 2145–2151.

Abioye, T., A. Medrano-Tellez et al. (2017). 'Laser metal deposition of multi-track walls of 308LSi stainless steel'. In: *Materials and Manufacturing Processes* 32, pp. 1660–1666.

Appleyard, David (2015). 'Powering up on powder technology'. In: *Metal Powder Report* 70.6, pp. 285–289. ISSN: 0026-0657. DOI: https://doi.org/10.1016/j.mprp.2015.08.075. URL: https://www.sciencedirect.com/science/article/pii/S0026065715005184.

ASTM E384 (2017). *Standard Test Method for Microindentation Hardness of Materials*. URL: https://compass.astm.org/document/?contentCode=ASTM%5C%7CE0384-17%5C%7Cen-US&proxycl=https%5C%3A%5C%2F%5C%2Fsecure.astm.org&fromLogin=true (visited on 28th May 2023).

Bandyopadhyay, Amit, Yanning Zhang and Bonny Onuike (2022). 'Additive manufacturing of bimetallic structures'. In: *Virtual and Physical Prototyping* 17(2), pp. 256–294.

Bombach, M. et al. (2018). 'Comparison of laser metal deposition of Inconel 718 from powder, hot and cold wire'. In: *Procedia CIRP* 74.

Bonneville, J and B Escaig (1979). 'Cross-slipping process and the stress-orientation dependence in pure copper'. In: *Acta Metallurgica* 27, pp. 1477–1486. ISSN: 0001-6160. DOI: https://doi.org/10.1016/0001-6160(79)90170-6. URL: https://www.sciencedirect.com/science/article/pii/0001616079901706.

Bourell, David L. (2016). 'Perspectives on Additive Manufacturing'. In: *Annual Review of Materials Research* 46.1, pp. 1–18. DOI: 10.1146/annurev-matsci-070115-031606.

Cai, Xiang et al. (2022). 'Advanced mechanical properties of nickel-aluminum bronze/steel composite structure prepared by wire-arc additive manufacturing'. In: *Materials Design* 221, p. 110969. ISSN: 0264-1275. DOI: https://doi.org/10.1016/j.matdes.2022.110969. URL: https://www.sciencedirect.com/science/article/pii/S0264127522005913.

Caliari, F. R. et al. (2013). 'Study of the Secondary Phases in Inconel 718 Aged Superalloy Using Thermodynamics Modeling'. In: *Key Engineering Materials* 553, pp. 23–28. DOI: 10.4028.

Dass, Adrita and Atieh Moridi (2019). 'State of the Art in Directed Energy Deposition: From Additive Manufacturing to Materials Design'. In: *Coatings* 9.

DebRoy, T. et al. (2017). 'Additive manufacturing of metallic components – Process, structure and properties'. In: *Progress in Materials Science* 92, pp. 112–224.

Dharmendra, C. et al. (2021). 'Atom probe tomography study of κ-phases in additively manufactured nickel aluminum bronze in as-built and heat-treated conditions'. In: *Materials and Design* 202.

Dieter, George E. (1988). *Mechanical Metallurgy*. McGraw-Hili Inc.

Engineering ToolBox (2022). *Metals, Metallic Elements and Alloys - Thermal Conductivities*. URL: https://www.engineeringtoolbox.com/thermal-conductivity-metals-d_858.html (visited on 20th Dec. 2022).

Gottstein, Günter (2004). *Physical Foundations of Material Science*. Springer.

Groh, Sébastien (2014). 'Transformation of shear loop into prismatic loops during bypass of an array of impenetrable particles by edge dislocations'. In: *Materials Science and Engineering: A* 618, pp. 29–36. ISSN: 0921-5093. DOI: https://doi.org/10.1016/j.msea.2014.08.079. URL: https://www.sciencedirect.com/science/article/pii/S0921509314010880.

Hájek, J. et al. (2016). 'Effect of heat treatment on microstructural changes in aluminium bronze'. In: *Archives of Metallurgy and Materials* 61.

Herzog, D. et al. (2016). 'Additive manufacturing of metals'. In: *Acta Materialia* 117, pp. 371–392.

Hjelen, Jarle (1986). *Scanning elektron-mikroskopi*. SINTEF.

Holmedal, Bjørn (2021). 'Lecture notes'. In: *TMT4222 Mechanical Properties of Metals*.

Hosseini, E. and V.A. Popovich (2019). 'A review of mechanical properties of additively manufactured Inconel 718'. In: *Additive Manufacturing* 30.

Hou, Wentao et al. (2021). 'Enhancing metallurgical and mechanical properties of friction stir butt welded joints of Al–Cu via cold sprayed Ni interlayer'. In: *Materials Science and Engineering: A* 809, p. 140992. ISSN: 0921-5093. DOI: https://doi.org/10.1016/j.msea.2021.140992. URL: https://www.sciencedirect.com/science/article/pii/S0921509321002616.

ISO 24373 (2018). *Welding consumables — Solid wires and rods for fusion welding of copper and copper alloys — Classification*. URL: https://www.iso.org/standard/72420.html (visited on 1st June 2023).

ISO 6507 (2018). *Metallic materials — Vickers hardness test*. URL: https://www.iso.org/obp/ui/#iso:std:iso:6507:-1:ed-4:v1:en (visited on 28th May 2023).

ISO/ASTM (2021). *Additive manufacturing — General principles — Terminology (52900)*. URL: https://www.iso.org/standard/74514.html (visited on 23rd May 2023).

Kah, Paul et al. (2015). 'Factors Influencing Al-Cu Weld Properties by Intermetallic Compound Formation'. In: *International Journal of Mechanical and Materials Engineering* 10. DOI: 10.1186/s40712-015-0037-8.

Kainuma, R. et al. (2013). 'Miscibility gap of B2 phase in NiAl to Cu3Al section of the Cu–Al–Ni system'. In: *Intermetallics* 13, pp. 23–28. DOI: 10.1016.

Lewandowski, John J. and Mohsen Seif (2016). 'Metal Additive Manufacturing: A Review of Mechanical Properties'. In: *The Annual Review of Materials Research* 46.

Li, Y. et al. (2018). 'Enhanced beads overlapping model for wire and arc additive manufacturing of multi-layer multi-bead metallic parts'. In: *Journal of Materials Processing Technology* 252, pp. 838–848.

Liu, Fencheng et al. (2020). 'Laves phase control of inconel 718 superalloy fabricated by laser direct energy deposition via delta aging and solution treatment'. In: *The Journal of Materials Research and Technology* 9(5), pp. 9753–9765.

Manvatkar, V., A. De and T. DebRoy (2014). 'Heat transfer and material flow during laser assisted multi-layer additive manufacturing'. In: *Journal of Applied Physics* 116.12. DOI: 10.1063/1.4896751. eprint: https://pubs.aip.org/aip/jap/article-pdf/doi/10.1063/1.4896751/15151984/124905_1_online.pdf. URL: https://doi.org/10.1063/1.4896751.

Marques, A. et al. (2022). 'Inconel 718–copper parts fabricated by 3D multi-material laser powder bed fusion: a novel technological and designing approach for rocket engine'. In: *The International Journal of Advanced Manufacturing Technology* 122, pp. 2113–2123.

Marques, Ana et al. (2022). 'Multi-Material Inconel 718 Parts with Highly Conductive Copper Cooling Channels for Aerospace Applications'. In: *Advanced Engineering Materials*. DOI: 10.1002/adem.202201349.

Meltio (2022a). *Laser metal deposition*. URL: https://meltio3d.com/technology/ (visited on 10th Oct. 2022).

— (2022b). *Meltio Nickel 718*. URL: https://meltio3d.com/wp-content/uploads/2022/10/Meltio-Nickel-718_Material_Datasheet.pdf (visited on 10th Oct. 2022).

Motta, M., A. G. Demir and B. Previtali (2018). 'High-speed imaging and process characterization of coaxial laser metal wire deposition'. In: *Additive Manufacturing* 22, pp. 497–507.

Munday, Lynn B., Joshua C. Crone and Jaroslaw Knap (2016). 'Prismatic and helical dislocation loop generation from defects'. In: *Acta Materialia* 103, pp. 217–228. ISSN: 1359-6454. DOI: https://doi.org/10.1016/j.actamat.2015.09.056. URL: https://www.sciencedirect.com/science/article/pii/S1359645415007454.

Murr, Lawrence E. et al. (2012). 'Metal Fabrication by Additive Manufacturing Using Laser and Electron Beam Melting Technologies'. In: *Journal of Materials Science Technology* 28.1, pp. 1–14. ISSN: 1005-0302. DOI: https://doi.org/10.1016/S1005-0302(12)60016-4. URL: https://www.sciencedirect.com/science/article/pii/S1005030212600164.

Ni, Mang et al. (2017). 'Anisotropic tensile behavior of in situ precipitation strengthened Inconel 718 fabricated by additive manufacturing'. In: *Materials Science & Engineering A* 701, pp. 344–351.

Ohring, Milton (1995). *Engineering materials science*. Department of Materials Science and Engineering, Stevens Institute of Technology.

Oliari, S. H., A. S. C. M. D'Oliveira and M. Schulz (2017). 'Additive Manufacturing of H11 with Wire-Based Laser Metal Deposition'. In: *Soldagem & Inspecao* 22, pp. 466–479.

Onuike, Bonny, Bryan Heer and Amit Bandyopadhyay (2018). 'Additive manufacturing of Inconel 718—Copper alloy bimetallic structure using laser engineered net shaping (LENS™)'. In: *Additive Manufacturing* 21, pp. 133–140. ISSN: 2214-8604. DOI: https://doi.org/10.1016/j.addma.2018.02.007. URL: https://www.sciencedirect.com/science/article/pii/S2214860417305055.

Orzolek, Sean M., Jennifer K. Semple and Charles R. Fisher (2022). 'Influence of processing on the microstructure of nickel aluminum bronze (NAB)'. In: *Additive Manufacturing* 56.

Particle Technology Labs (2023). *Energy Dispersive X-Ray Spectroscopy (EDS/EDX)*. URL: https://particletechlabs.com/analytical-testing/energy-dispersive-x-ray-spectroscopy-eds-edx/ (visited on 23rd May 2023).

Popovich, V.A. et al. (2017). 'Functionally graded Inconel 718 processed by additive manufacturing: Crystallographic texture, anisotropy of microstructure and mechanical properties'. In: *Materials and Design* 114, pp. 441–449.

Ringel, Bjoern et al. (2022). 'Advancing functional integration through multi-material additive manufacturing: Simulation and experimental validation of a burner nozzle'. In: *Materials Today: Proceedings* 70, pp. 296–303.

Rottenfusser, R., E. E. Wilson and M. W. Davidson (2022). *Education in Microscopy and Digital Imaging*. URL: https://zeiss-campus.magnet.fsu.edu/articles/basics/reflected.html (visited on 20th Dec. 2022).

Sahu, A. K. and S. Bag (2021). 'Design of a double aging treatment for the improvement of mechanical and microstructural properties of pulse micro-plasma arc welded alloy 718'. In: *The Journal of Materials Science* 56.

Sláma, Peter, Jaromír Dlouhý and Michal Kövér (2014). 'Influence of heat treatment on the microstructure and mechanical properties of aluminium bronze'. In: *Materials and Technology* 48.

Solberg, Jan Ketil (2017). *Teknologisk metaller og legeringer*. NTNU.

Special Metals Corporation (2022). *Inconel alloy 718*. URL: https://www.specialmetals.com/documents/technical-bulletins/inconel/inconel-alloy-718.pdf (visited on 14th Dec. 2022).

Strondl, A. et al. (2008). 'Investigations of MX and / precipitates in the nickel-based superalloy 718 produced by electron beam melting'. In: *Materials Science and Engineering: A* 480.1, pp. 138–147. ISSN: 0921-5093. DOI: https://doi.org/10.1016/j.msea.2007.07.012. URL: https://www.sciencedirect.com/science/article/pii/S0921509307013949.

Strößner, Johannes, Michael Terock and Uwe Glatzel (2015). 'Mechanical and Microstructural Investigation of Nickel-Based Superalloy IN718 Manufactured by Selective Laser Melting (SLM)'. In: *Advanced Engineering Materials* 17.

Sutton, Michael et al. (2007). 'Scanning Electron Microscopy for Quantitative Small and Large Deformation Measurements Part I: SEM Imaging at Magnifications from 200 to 10,000'. In: *Experimental Mechanics* 47, pp. 775–787. DOI: 10.1007/s11340-007-9042-z.

Toray Research Center (2023). *Electron Backscatter Diffraction EBSD*. URL: https://www.toray-research.co.jp/en/technicaldata/techniques/EBSD.html (visited on 27th May 2023).

Tucho, Wakshum M. et al. (2017). 'Microstructure and hardness studies of Inconel 718 manufactured by selective laser melting before and after solution heat treatment'. In: *Materials Science & Engineering A* 689, pp. 220–232.

UTP Maintenance (2023). *UTP A 34*. URL: https://www.alruqee.com/Userfiles/Product/TablePdf/11062016000000UTP%5C%20A%5C%2034.pdf (visited on 24th Jan. 2023).

Villars, Pierre and Hiroaki Okamoto, eds. (n.d.). *Cu-Ni Binary Phase Diagram 0-100 at.% Ni: Datasheet from "PAULING FILE Multinaries Edition – 2022" in SpringerMaterials (https://materials.springer.com/isp/phase-diagram/docs/c_0906411)*. accessed 2023-05-30. URL: https://materials.springer.com/isp/phase-diagram/docs/c_0906411.

Wang, Chenyang et al. (2020). 'Laser additive manufacturing of bimetallic structure from TC4 to IN718 via Ta/Cu multi-interlayer'. In: *Materials Research Express* 7.

Wang, Jian and Xinghang Zhang (2016). 'Twinning effects on strength and plasticity of metallic materials'. In: *MRS Bulletin* 41.4, pp. 274–281. DOI: 10.1557/mrs.2016.67.

Wei, Xian-ping et al. (2013). 'Elemental Partitioning Characteristics of Equilibrium Phases in Inconel 718 Alloy at 600-1100°'. In: *Journal of Iron and Steel Research* 20(6), pp. 88–94.

Wright, Roger N. (2016). *Wire Technology (Second Edition)*. Butterworth-Heinemann.

Yen, Yee-wen, Jian-wei Su and Dong-ping Huang (2008). 'Phase equilibria of the Fe–Cr–Ni ternary systems and interfacial reactions in Fe–Cr alloys with Ni substrate'. In: *Journal of Alloys and Compounds* 457, pp. 270–278. ISSN: 0925-8388. DOI: https://doi.org/10.1016/j.jallcom.2007.03.053. URL: https://www.sciencedirect.com/science/article/pii/S0925838807006895.

Zapata, A. et al. (2016). 'Investigation on the Cause-Effect Relationships between the Process Parameters and the Resulting Geometric Properties for Wire-Based Coaxial Laser Metal Deposition'. In: *Robotics and Computer-Integrated Manufacturing* 39, pp. 32–42.

Zhong, C., A. Gasser, G. Backes et al. (2022). 'Laser additive manufacturing of Inconel 718 at increased deposition rates'. In: *Materials Science and Engineering: A* 844.

Zhong, C., A. Gasser, J. Kittel et al. (2016). 'Improvement of material performance of Inconel 718 formed by high deposition-rate laser metal deposition'. In: *Materials and Design* 98, pp. 128–134.

Zhou, W. et al. (2006). 'Fundamentals of Scanning Electron Microscopy'. In: *Scanning microscopy for Nanotechnology*, pp. 1–40.

ZwickRoell (2023). *Vickers hardness test to ISO 6507/ASTM E384*. URL: https://www.zwickroell.com/industries/metals/metals-standards/vickers-test-iso-6507/ (visited on 22nd May 2023).

Appendix

A Process parameters for sample no. 2

Material	**Layer**	$P[W]$	$v_t[mm/s]$	$v_w[mm/s]$	$P_w[W]$	$Z[mm]$	$d[mm]$
IN718	1-8	1200	8	7	350	-0.5	1.5
CuAl7	9-12	1200	8	7	350	-0.5	1.5

Table 16: Process parameters used in the discrete layers for specimen manufacturing of the second specimen (sample no. 2) by LMWD. P is the laser power, v_t is the traverse speed, v_w represents the wire feed rate and P_w is the hot wire power, while Z and d are the laser beam focal position and the hatch spacing, respectively.

B EDS analysis

B.1 Analysis of microstructure with EDS

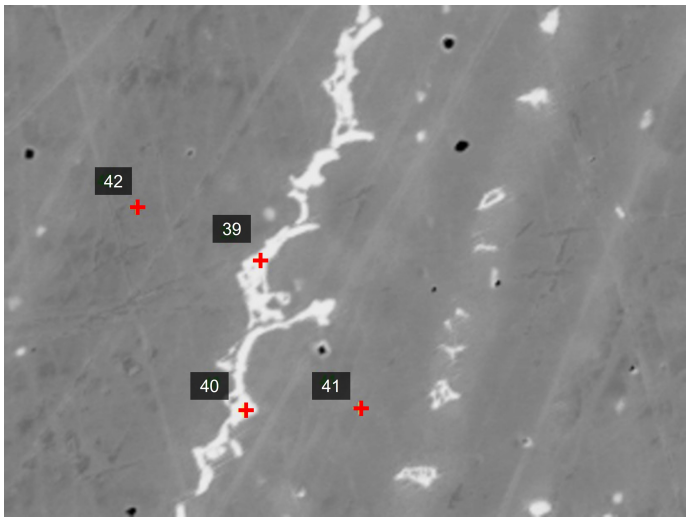

(a)

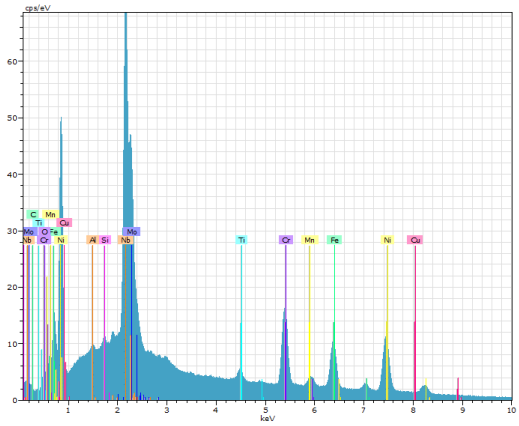

(b) 39

El	AN	Series	unn. C [wt.%]	norm. C [wt.%]	Atom. C [at.%]	Error (1 Sigma) [wt.%]
Ni	28	K-series	29.44	39.76	42.94	1.17
Fe	26	K-series	11.55	15.60	17.70	0.43
Cr	24	K-series	9.82	13.26	16.16	0.34
Nb	41	L-series	16.90	22.83	15.57	0.63
Mo	42	L-series	4.62	6.25	4.13	0.19
Ti	22	K-series	0.87	1.18	1.56	0.05
Si	14	K-series	0.30	0.40	0.91	0.04
Mn	25	K-series	0.44	0.59	0.68	0.04
Al	13	K-series	0.11	0.15	0.34	0.03
C	6	K-series	0.00	0.00	0.00	0.00
O	8	K-series	0.00	0.00	0.00	0.00
Cu	29	L-series	0.00	0.00	0.00	0.00
		Total:	74.05	100.00	100.00	

(c) 39

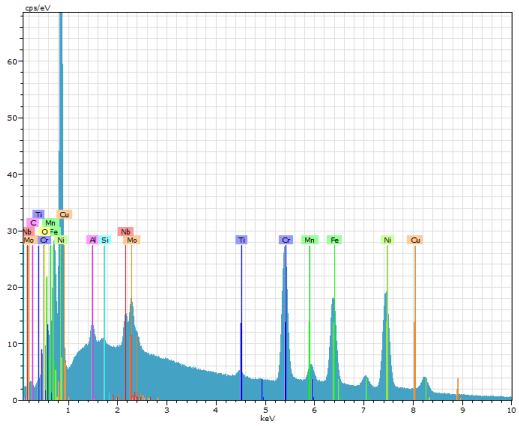

(d) 42

El	AN	Series	unn. C [wt.%]	norm. C [wt.%]	Atom. C [at.%]	Error (1 Sigma) [wt.%]
Ni	28	K-series	41.36	55.08	53.60	1.63
Fe	26	K-series	16.54	22.02	22.52	0.59
Cr	24	K-series	12.88	17.15	18.84	0.44
Mo	42	L-series	1.53	2.04	1.22	0.08
Al	13	K-series	0.39	0.52	1.09	0.04
Nb	41	L-series	1.29	1.71	1.05	0.07
Mn	25	K-series	0.73	0.97	1.01	0.05
Ti	22	K-series	0.30	0.40	0.48	0.04
Si	14	K-series	0.07	0.09	0.18	0.03
C	6	K-series	0.00	0.00	0.00	0.00
O	8	K-series	0.00	0.00	0.00	0.00
Cu	29	L-series	0.00	0.00	0.00	0.00
		Total:	75.08	100.00	100.00	

(e) 42

Figure B.1: Raw data from EDS of microstructure in the IN718.

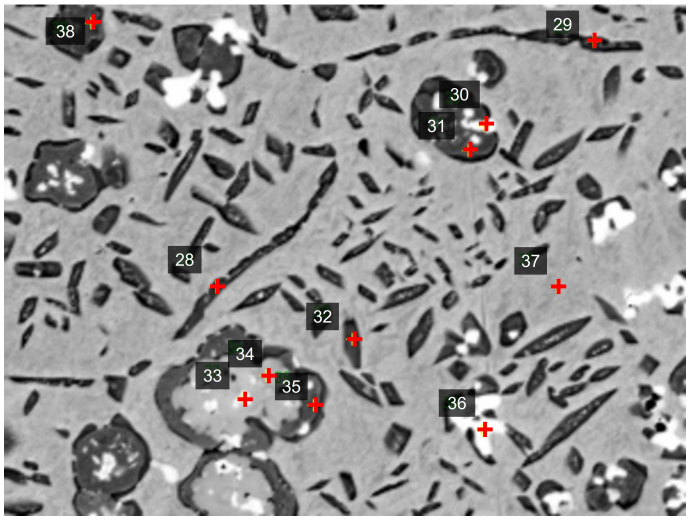

(a) Sample area in CuAl7, approximately $400\mu m$ from interface.

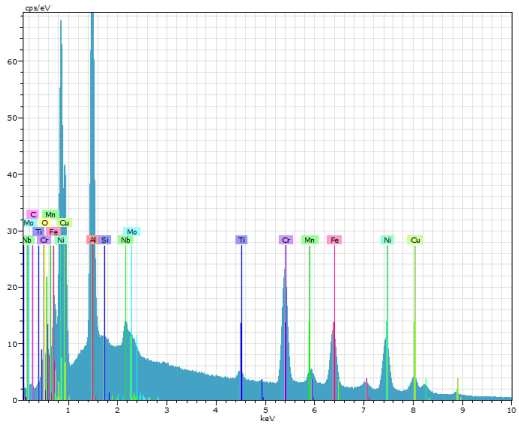

(b) 29

El	AN	Series	unn. C [wt.%]	norm. C [wt.%]	Atom. C [at.%]	Error (1 Sigma) [wt.%]
Ni	28	K-series	26.08	35.36	30.97	1.04
Al	13	K-series	7.82	10.59	20.18	0.38
Cr	24	K-series	12.36	16.76	16.57	0.42
Fe	26	K-series	12.82	17.38	16.00	0.47
Cu	29	L-series	10.69	14.50	11.73	1.25
Mn	25	K-series	0.97	1.32	1.23	0.06
Nb	41	L-series	1.48	2.00	1.11	0.08
Si	14	K-series	0.38	0.51	0.93	0.04
Ti	22	K-series	0.60	0.81	0.87	0.05
Mo	42	L-series	0.57	0.77	0.42	0.05
C	6	K-series	0.00	0.00	0.00	0.00
O	8	K-series	0.00	0.00	0.00	0.00
		Total:	73.77	100.00	100.00	

(c) 29

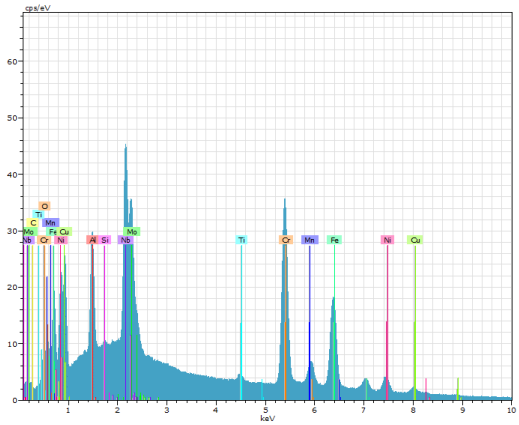

(d) 30

El	AN	Series	unn. C [wt.%]	norm. C [wt.%]	Atom. C [at.%]	Error (1 Sigma) [wt.%]
Cr	24	K-series	22.83	28.49	31.65	0.76
Fe	26	K-series	23.05	28.78	29.76	0.82
Ni	28	K-series	9.16	11.44	11.25	0.39
Cu	29	L-series	6.80	8.49	7.72	0.84
Nb	41	L-series	9.90	12.36	7.68	0.38
Al	13	K-series	2.15	2.69	5.76	0.12
Mo	42	L-series	4.26	5.31	3.20	0.18
Mn	25	K-series	1.17	1.46	1.53	0.07
Ti	22	K-series	0.53	0.66	0.80	0.04
Si	14	K-series	0.26	0.32	0.65	0.04
C	6	K-series	0.00	0.00	0.00	0.00
O	8	K-series	0.00	0.00	0.00	0.00
		Total:	80.12	100.00	100.00	

(e) 30

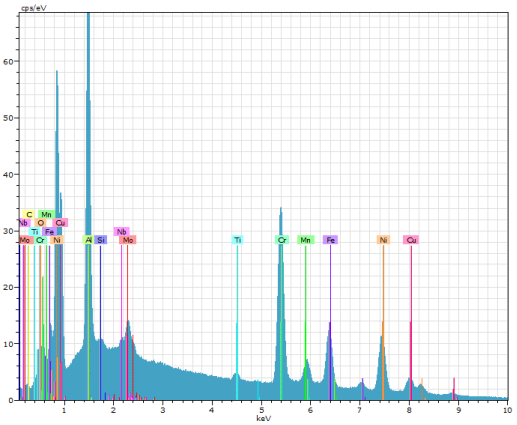

(f) 31

El	AN	Series	unn. C [wt.%]	norm. C [wt.%]	Atom. C [at.%]	Error (1 Sigma) [wt.%]
Ni	28	K-series	27.26	33.85	30.05	1.08
Cr	24	K-series	19.45	24.16	24.21	0.65
Al	13	K-series	6.87	8.53	16.48	0.34
Fe	26	K-series	12.89	16.01	14.94	0.47
Cu	29	L-series	9.88	12.27	10.06	1.16
Mn	25	K-series	1.27	1.57	1.49	0.07
Mo	42	L-series	1.47	1.82	0.99	0.08
Si	14	K-series	0.29	0.36	0.67	0.04
Ti	22	K-series	0.46	0.57	0.62	0.04
Nb	41	L-series	0.69	0.86	0.48	0.05
C	6	K-series	0.00	0.00	0.00	0.00
O	8	K-series	0.00	0.00	0.00	0.00
		Total:	80.52	100.00	100.00	

(g) 31

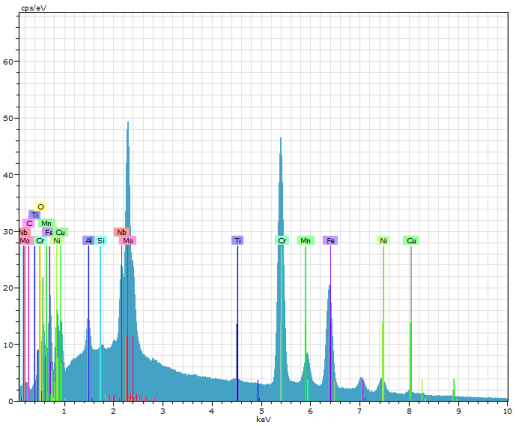

(h) 33

El	AN	Series	unn. C [wt.%]	norm. C [wt.%]	Atom. C [at.%]	Error (1 Sigma) [wt.%]
Cr	24	K-series	29.49	35.30	39.63	0.97
Fe	26	K-series	25.32	30.31	31.68	0.89
Ni	28	K-series	8.73	10.45	10.39	0.37
Mo	42	L-series	10.06	12.05	7.33	0.38
Cu	29	L-series	3.43	4.10	3.77	0.47
Nb	41	L-series	4.14	4.96	3.12	0.17
Al	13	K-series	0.65	0.78	1.69	0.06
Mn	25	K-series	1.32	1.58	1.68	0.07
Ti	22	K-series	0.26	0.31	0.38	0.04
Si	14	K-series	0.14	0.16	0.34	0.03
C	6	K-series	0.00	0.00	0.00	0.00
O	8	K-series	0.00	0.00	0.00	0.00
		Total:	83.54	100.00	100.00	

(i) 33

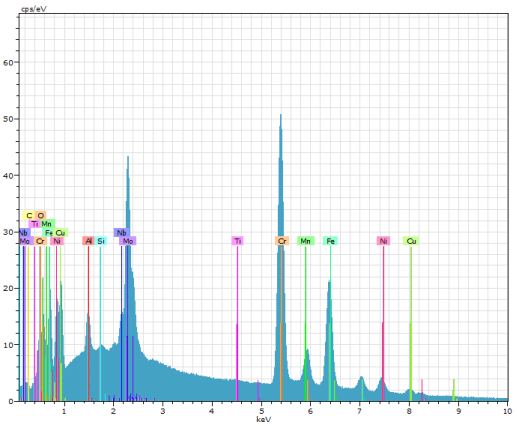

(j) 34

El	AN	Series	unn. C [wt.%]	norm. C [wt.%]	Atom. C [at.%]	Error (1 Sigma) [wt.%]
Cr	24	K-series	31.26	37.06	40.88	1.02
Fe	26	K-series	25.71	30.47	31.29	0.91
Ni	28	K-series	8.57	10.16	9.93	0.37
Cu	29	L-series	5.88	6.97	6.29	0.74
Mo	42	L-series	8.64	10.24	6.12	0.33
Mn	25	K-series	1.50	1.78	1.85	0.08
Al	13	K-series	0.72	0.85	1.81	0.06
Nb	41	L-series	1.83	2.17	1.34	0.09
Si	14	K-series	0.12	0.14	0.28	0.03
Ti	22	K-series	0.14	0.17	0.21	0.03
C	6	K-series	0.00	0.00	0.00	0.00
O	8	K-series	0.00	0.00	0.00	0.00
		Total:	84.37	100.00	100.00	

(k) 34

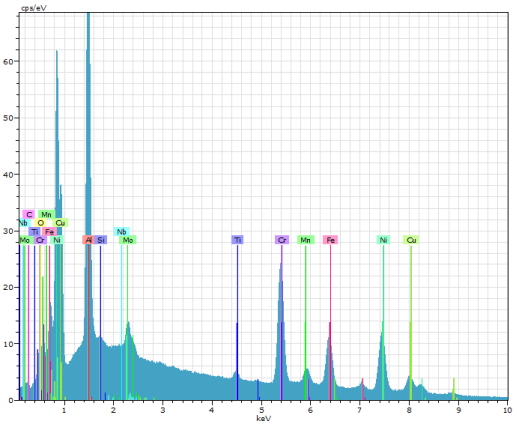

(l) 35

El	AN	Series	unn. C [wt.%]	norm. C [wt.%]	Atom. C [at.%]	Error (1 Sigma) [wt.%]
Ni	28	K-series	27.05	37.73	32.95	1.08
Al	13	K-series	7.73	10.79	20.49	0.38
Cr	24	K-series	12.82	17.88	17.63	0.44
Fe	26	K-series	10.90	15.21	13.96	0.40
Cu	29	L-series	9.71	13.55	10.93	1.14
Mn	25	K-series	0.88	1.23	1.15	0.06
Mo	42	L-series	1.41	1.96	1.05	0.08
Si	14	K-series	0.32	0.44	0.81	0.04
Ti	22	K-series	0.51	0.71	0.76	0.04
Nb	41	L-series	0.35	0.49	0.27	0.04
C	6	K-series	0.00	0.00	0.00	0.00
O	8	K-series	0.00	0.00	0.00	0.00
		Total:	71.68	100.00	100.00	

(m) 35

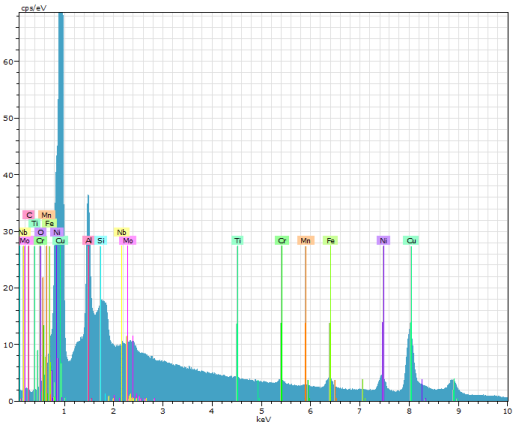

(n) 37

El	AN	Series	unn. C [wt.%]	norm. C [wt.%]	Atom. C [at.%]	Error (1 Sigma) [wt.%]
Cu	29	L-series	29.86	64.34	56.46	3.21
Ni	28	K-series	8.21	17.70	16.82	0.35
Al	13	K-series	2.94	6.34	13.09	0.16
Si	14	K-series	1.31	2.83	5.63	0.08
Fe	26	K-series	2.23	4.80	4.79	0.11
Cr	24	K-series	0.53	1.14	1.22	0.04
Mo	42	L-series	0.63	1.35	0.79	0.05
Nb	41	L-series	0.39	0.84	0.51	0.04
Mn	25	K-series	0.22	0.47	0.48	0.04
Ti	22	K-series	0.09	0.19	0.22	0.03
O	8	K-series	0.00	0.00	0.00	0.00
C	6	K-series	0.00	0.00	0.00	0.00
		Total:	46.40	100.00	100.00	

(o) 37

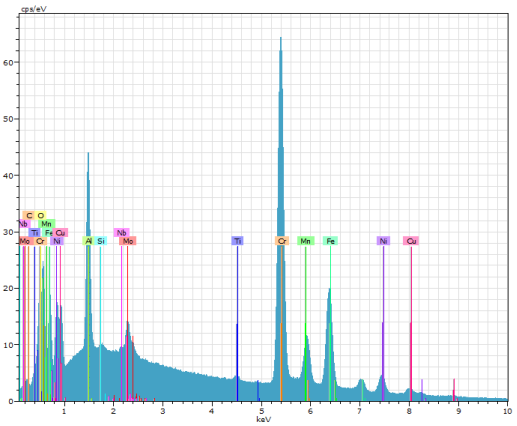

(p) 38

El	AN	Series	unn. C [wt.%]	norm. C [wt.%]	Atom. C [at.%]	Error (1 Sigma) [wt.%]
Cr	24	K-series	37.85	47.00	47.58	1.23
Fe	26	K-series	22.27	27.65	26.06	0.79
Ni	28	K-series	9.00	11.17	10.02	0.38
Al	13	K-series	3.20	3.98	7.76	0.17
Cu	29	L-series	4.12	5.11	4.23	0.54
Mn	25	K-series	2.01	2.49	2.39	0.10
Mo	42	L-series	1.36	1.69	0.93	0.07
Ti	22	K-series	0.32	0.40	0.44	0.04
Si	14	K-series	0.12	0.15	0.28	0.03
Nb	41	L-series	0.26	0.32	0.18	0.04
O	8	K-series	0.03	0.04	0.13	0.03
C	6	K-series	0.00	0.00	0.00	0.00
		Total:	80.53	100.00	100.00	

(q) 38

Figure B.2: Raw data from EDS of microstructure in the interface (zone 1).

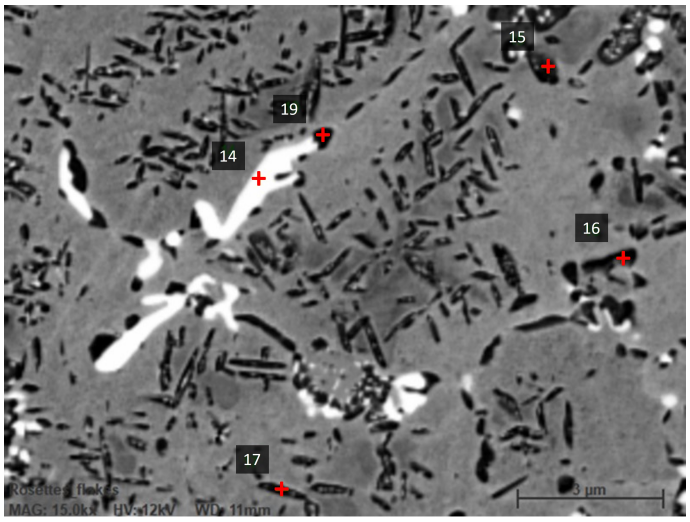

(a) Sample area in CuAl7, approximately $300\mu m$ from interface.

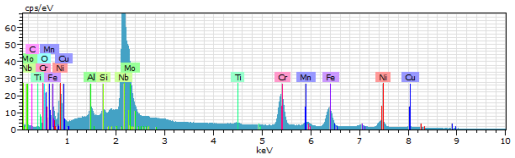

(b) 14

El	AN	Series	unn. C [wt.%]	norm. C [wt.%]	Atom. C [at.%]	Error (1 Sigma) [wt.%]
Fe	26	K-series	17.47	22.48	25.55	0.63
Cr	24	K-series	14.93	19.21	23.45	0.50
Ni	28	K-series	15.43	19.85	21.47	0.63
Nb	41	L-series	23.80	30.63	20.93	0.88
Mo	42	L-series	3.41	4.39	2.90	0.15
Al	13	K-series	0.60	0.77	1.82	0.05
Si	14	K-series	0.53	0.69	1.55	0.05
Mn	25	K-series	0.74	0.96	1.11	0.05
Ti	22	K-series	0.49	0.63	0.84	0.04
Cu	29	L-series	0.30	0.38	0.38	0.08
O	8	K-series	0.00	0.00	0.00	0.00
C	6	K-series	0.00	0.00	0.00	0.00
		Total:	77.71	100.00	100.00	

(c) 14

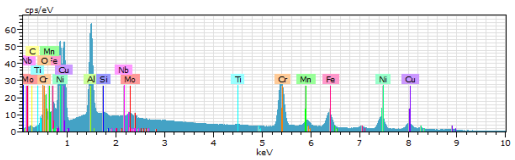

(d) 15

El	AN	Series	unn. C [wt.%]	norm. C [wt.%]	Atom. C [at.%]	Error (1 Sigma) [wt.%]
Ni	28	K-series	19.22	28.56	25.67	0.78
Cr	24	K-series	16.00	23.78	24.12	0.54
Cu	29	L-series	13.67	20.32	16.87	1.56
Fe	26	K-series	10.89	16.19	15.29	0.40
Al	13	K-series	5.03	7.47	14.60	0.25
Mn	25	K-series	1.17	1.74	1.67	0.07
Si	14	K-series	0.28	0.41	0.77	0.04
Mo	42	L-series	0.62	0.93	0.51	0.05
Ti	22	K-series	0.21	0.31	0.34	0.03
Nb	41	L-series	0.20	0.29	0.16	0.03
C	6	K-series	0.00	0.00	0.00	0.00
O	8	K-series	0.00	0.00	0.00	0.00
		Total:	67.30	100.00	100.00	

(e) 15

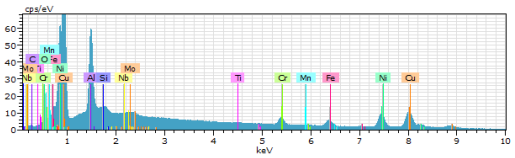

(f) 16

El	AN	Series	unn. C [wt.%]	norm. C [wt.%]	Atom. C [at.%]	Error (1 Sigma) [wt.%]
Cu	29	L-series	22.09	41.15	34.88	2.42
Ni	28	K-series	19.03	35.45	32.53	0.77
Al	13	K-series	4.74	8.82	17.61	0.24
Fe	26	K-series	3.76	7.00	6.75	0.16
Cr	24	K-series	2.39	4.45	4.61	0.10
Si	14	K-series	0.60	1.12	2.15	0.05
Mo	42	L-series	0.46	0.85	0.48	0.04
Mn	25	K-series	0.24	0.45	0.45	0.04
Ti	22	K-series	0.14	0.27	0.30	0.03
Nb	41	L-series	0.23	0.42	0.24	0.03
O	8	K-series	0.00	0.00	0.00	0.00
C	6	K-series	0.00	0.00	0.00	0.00
		Total:	53.67	100.00	100.00	

(g) 16

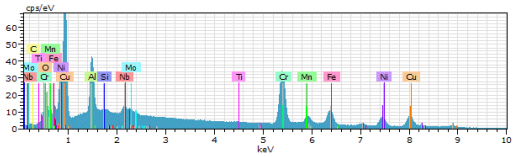

(h) 17

El	AN	Series	unn. C [wt.%]	norm. C [wt.%]	Atom. C [at.%]	Error (1 Sigma) [wt.%]
Cr	24	K-series	18.12	25.68	27.15	0.61
Cu	29	L-series	21.22	30.08	26.02	2.35
Ni	28	K-series	13.94	19.77	18.51	0.57
Fe	26	K-series	10.73	15.22	14.98	0.40
Al	13	K-series	3.14	4.46	9.08	0.17
Mn	25	K-series	1.36	1.92	1.93	0.07
Nb	41	L-series	1.10	1.56	0.92	0.07
Si	14	K-series	0.30	0.42	0.82	0.04
Mo	42	L-series	0.54	0.76	0.44	0.05
Ti	22	K-series	0.10	0.14	0.16	0.03
C	6	K-series	0.00	0.00	0.00	0.00
O	8	K-series	0.00	0.00	0.00	0.00
		Total:	70.55	100.00	100.00	

(i) 17

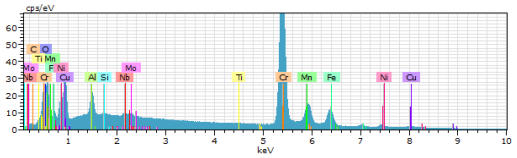

(j) 19

El	AN	Series	unn. C [wt.%]	norm. C [wt.%]	Atom. C [at.%]	Error (1 Sigma) [wt.%]
Cr	24	K-series	54.42	61.73	63.15	1.76
Fe	26	K-series	13.14	14.91	14.20	0.48
Cu	29	L-series	9.74	11.05	9.25	1.16
Ni	28	K-series	5.22	5.92	5.36	0.24
Mn	25	K-series	3.34	3.79	3.67	0.14
Al	13	K-series	1.29	1.46	2.88	0.08
O	8	K-series	0.20	0.23	0.75	0.06
Si	14	K-series	0.11	0.13	0.25	0.03
Nb	41	L-series	0.33	0.38	0.22	0.04
Mo	42	L-series	0.26	0.30	0.16	0.04
Ti	22	K-series	0.09	0.10	0.11	0.03
C	6	K-series	0.00	0.00	0.00	0.00
		Total:	88.14	100.00	100.00	

(k) 19

Figure B.3: Raw data from EDS of microstructure in the interface (zone 3).

B.2 Mapping the prior position of CuAl7_h tensile specimen within the 3D printed part by EDS

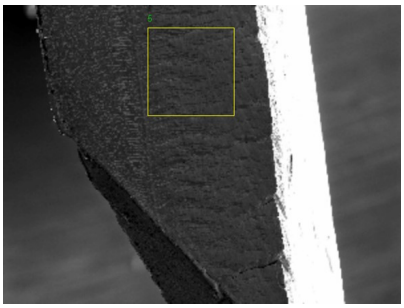

(a) $CuAl7_h$(Series1)

El	AN	Series	unn. C [wt.%]	norm. C [wt.%]	Atom. C [at.%]	Error (1 Sigma) [wt.%]
Cu	29	L-series	91.21	91.21	82.33	9.97
Al	13	K-series	7.53	7.53	16.01	0.37
Si	14	K-series	0.37	0.37	0.76	0.05
Mn	25	K-series	0.28	0.28	0.29	0.05
Ni	28	K-series	0.25	0.25	0.25	0.06
Fe	26	K-series	0.15	0.15	0.16	0.04
Ti	22	K-series	0.12	0.12	0.14	0.04
Nb	41	L-series	0.08	0.08	0.05	0.03
Cr	24	K-series	0.01	0.01	0.01	0.03
		Total:	100.00	100.00	100.00	

(b) Chemical composition.

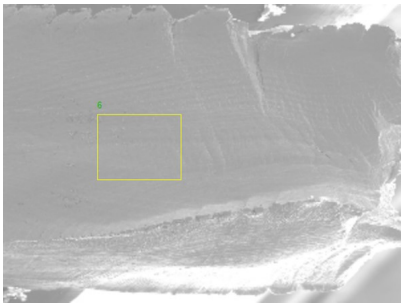

(c) $CuAl7_h$(Series2)

El	AN	Series	unn. C [wt.%]	norm. C [wt.%]	Atom. C [at.%]	Error (1 Sigma) [wt.%]
Cu	29	L-series	91.95	91.95	83.27	10.07
Al	13	K-series	7.25	7.25	15.46	0.36
Si	14	K-series	0.45	0.45	0.91	0.05
Ni	28	K-series	0.21	0.21	0.20	0.06
Mn	25	K-series	0.12	0.12	0.13	0.04
Fe	26	K-series	0.03	0.03	0.03	0.03
Cr	24	K-series	0.00	0.00	0.00	0.00
Ti	22	K-series	0.00	0.00	0.00	0.00
Nb	41	L-series	0.00	0.00	0.00	0.00
		Total:	100.00	100.00	100.00	

(d) Chemical composition.

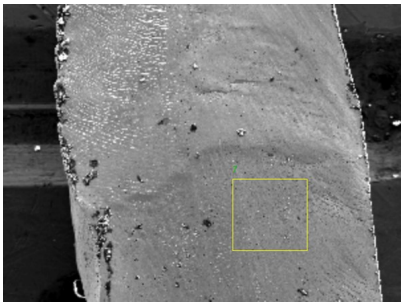

(e) $CuAl7_h$(Series3)

El	AN	Series	unn. C [wt.%]	norm. C [wt.%]	Atom. C [at.%]	Error (1 Sigma) [wt.%]
Cu	29	L-series	80.71	89.53	80.60	8.84
Al	13	K-series	6.81	7.56	16.02	0.34
Ni	28	K-series	1.30	1.44	1.41	0.12
Si	14	K-series	0.44	0.48	0.99	0.05
Fe	26	K-series	0.36	0.40	0.41	0.05
Mn	25	K-series	0.23	0.25	0.26	0.05
Cr	24	K-series	0.20	0.22	0.24	0.04
Mo	42	L-series	0.08	0.09	0.05	0.03
Nb	41	L-series	0.03	0.03	0.02	0.03
Ti	22	K-series	0.00	0.00	0.00	0.00
		Total:	90.15	100.00	100.00	

(f) Chemical composition.

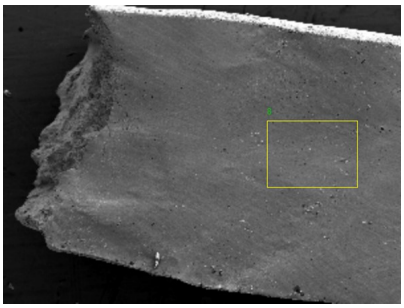

(g) $CuAl7_h$(Series4)

El	AN	Series	unn. C [wt.%]	norm. C [wt.%]	Atom. C [at.%]	Error (1 Sigma) [wt.%]
Cu	29	L-series	81.52	84.95	76.55	8.94
Al	13	K-series	6.59	6.87	14.58	0.33
Ni	28	K-series	3.62	3.77	3.68	0.22
Fe	26	K-series	1.56	1.63	1.67	0.11
Si	14	K-series	0.75	0.79	1.60	0.06
Cr	24	K-series	1.29	1.35	1.49	0.08
Nb	41	L-series	0.39	0.41	0.25	0.05
Mo	42	L-series	0.17	0.18	0.11	0.04
Ti	22	K-series	0.04	0.04	0.05	0.03
Mn	25	K-series	0.02	0.02	0.02	0.03
		Total:	95.97	100.00	100.00	

(h) Chemical composition.

Figure B.4: $CuAl7_h$ from unknown position in as-deposited sample. EDS area analysis with SEM/SE pictures to the left and the respective chemical concentrations to the right.

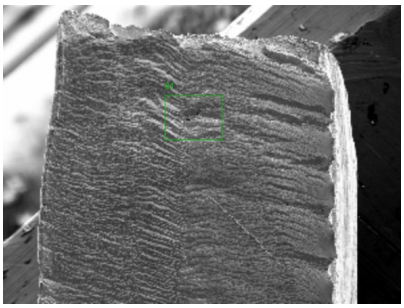

(a) $CuAl7_{h(1)}$ (1_1)

El	AN	Series	unn. C [wt.%]	norm. C [wt.%]	Atom. C [at.%]	Error (1 Sigma) [wt.%]
Cu	29	L-series	88.94	88.94	73.15	9.70
Al	13	K-series	7.41	7.41	14.36	0.37
C	6	K-series	2.30	2.30	10.00	0.49
O	8	K-series	0.40	0.40	1.31	0.12
Si	14	K-series	0.32	0.32	0.60	0.04
Ni	28	K-series	0.27	0.27	0.24	0.06
Mn	25	K-series	0.24	0.24	0.23	0.05
Cr	24	K-series	0.08	0.08	0.08	0.04
Mo	42	L-series	0.03	0.03	0.01	0.03
Nb	41	L-series	0.01	0.01	0.00	0.03
Fe	26	K-series	0.00	0.00	0.00	0.00
Ti	22	K-series	0.00	0.00	0.00	0.00
Total:			100.00	100.00	100.00	

(b) Chemical composition.

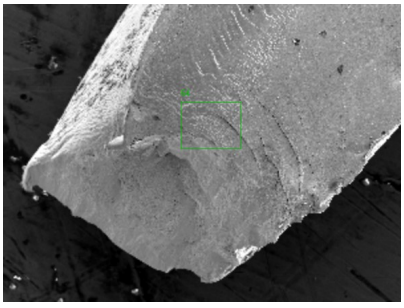

(c) $CuAl7_{h(1)}$ (1_2)

El	AN	Series	unn. C [wt.%]	norm. C [wt.%]	Atom. C [at.%]	Error (1 Sigma) [wt.%]
Cu	29	L-series	74.77	84.47	64.42	8.36
C	6	K-series	3.72	4.20	16.95	0.74
Al	13	K-series	6.83	7.71	13.85	0.34
O	8	K-series	0.67	0.76	2.29	0.18
Ni	28	K-series	1.27	1.44	1.19	0.13
Mn	25	K-series	0.51	0.57	0.51	0.06
Fe	26	K-series	0.38	0.42	0.37	0.06
Cr	24	K-series	0.24	0.27	0.26	0.05
Si	14	K-series	0.07	0.07	0.13	0.03
Mo	42	L-series	0.07	0.08	0.04	0.03
Nb	41	L-series	0.00	0.00	0.00	0.00
Ti	22	K-series	0.00	0.00	0.00	0.00
Total:			88.52	100.00	100.00	

(d) Chemical composition.

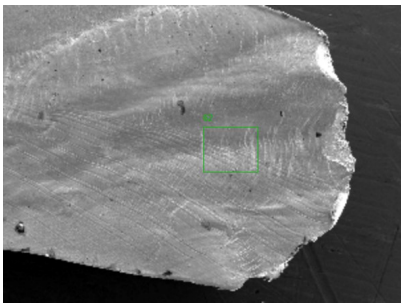

(e) $CuAl7_{h(2)}$ (2_1)

El	AN	Series	unn. C [wt.%]	norm. C [wt.%]	Atom. C [at.%]	Error (1 Sigma) [wt.%]
Cu	29	L-series	79.49	85.65	68.92	8.73
Al	13	K-series	6.25	6.74	12.77	0.32
C	6	K-series	2.77	2.98	12.70	0.56
O	8	K-series	0.53	0.57	1.83	0.14
Ni	28	K-series	1.84	1.98	1.73	0.14
Fe	26	K-series	0.79	0.85	0.78	0.08
Cr	24	K-series	0.56	0.60	0.59	0.06
Si	14	K-series	0.17	0.18	0.33	0.04
Mn	25	K-series	0.25	0.26	0.25	0.05
Mo	42	L-series	0.07	0.08	0.04	0.03
Nb	41	L-series	0.06	0.06	0.03	0.03
Ti	22	K-series	0.03	0.03	0.03	0.03
Total:			92.81	100.00	100.00	

(f) Chemical composition.

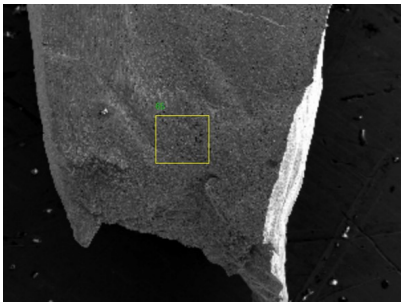

(g) $CuAl7_{h(2)}$ (2_2)

El	AN	Series	unn. C [wt.%]	norm. C [wt.%]	Atom. C [at.%]	Error (1 Sigma) [wt.%]
Cu	29	L-series	69.18	80.66	62.69	7.76
C	6	K-series	3.36	3.92	16.13	0.67
Al	13	K-series	5.58	6.50	11.90	0.29
Ni	28	K-series	3.37	3.93	3.31	0.22
O	8	K-series	0.61	0.72	2.21	0.17
Fe	26	K-series	1.45	1.69	1.49	0.11
Cr	24	K-series	1.17	1.36	1.29	0.08
Mn	25	K-series	0.43	0.50	0.45	0.06
Ti	22	K-series	0.24	0.28	0.29	0.04
Nb	41	L-series	0.24	0.28	0.15	0.04
Mo	42	L-series	0.12	0.14	0.07	0.04
Si	14	K-series	0.00	0.00	0.00	0.00
Total:			85.76	100.00	100.00	

(h) Chemical composition.

Figure B.5: $CuAl7_h$ from known position in sample. EDS area analysis with SEM/SE pictures to the left and the respective chemical concentrations to the right.

C Tensile test setup

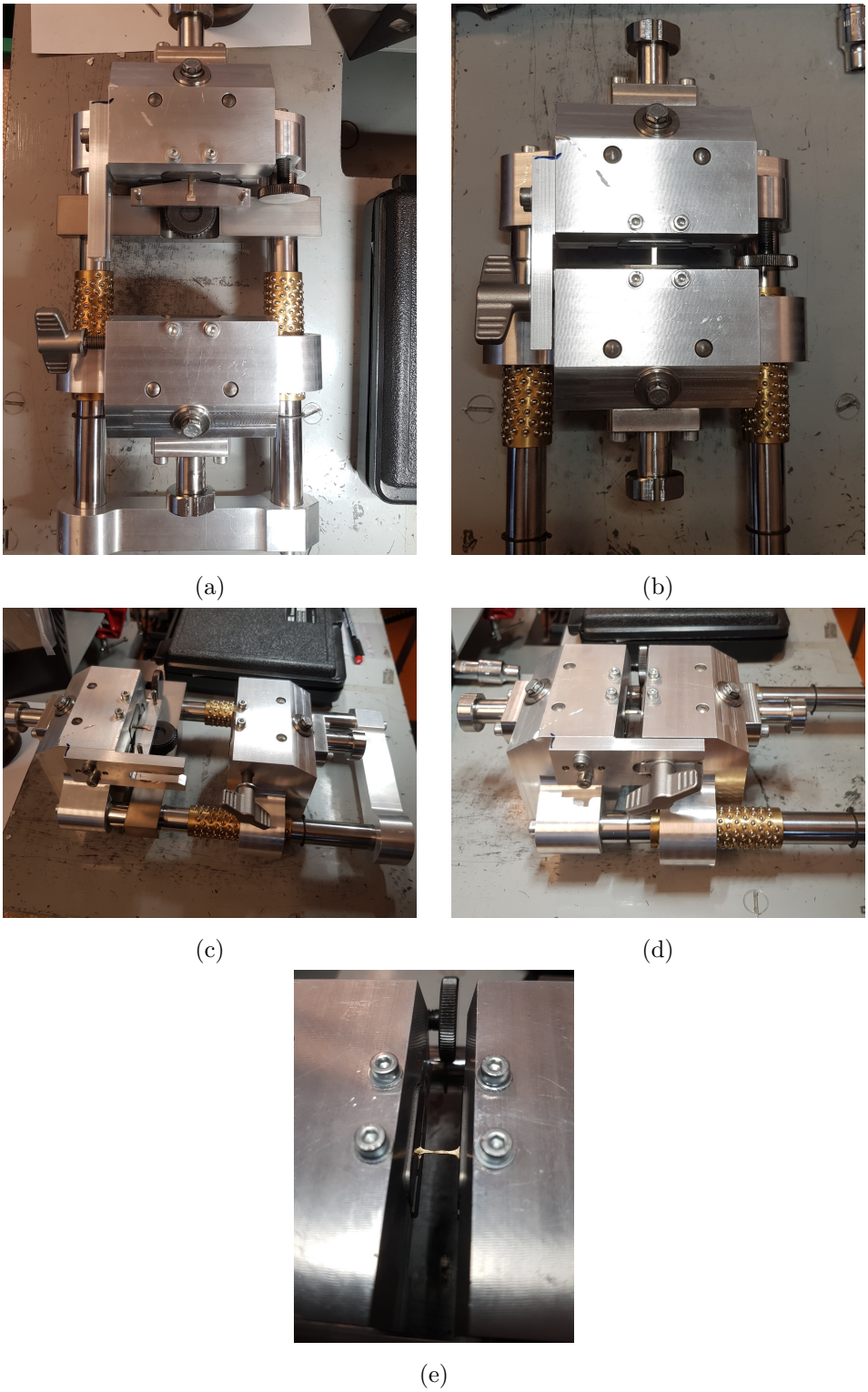

(a) (b) (c) (d) (e)

Figure C.1: Pictures showing the mounting of micro-tensile specimens. In a) and c), one side of the specimen is fastened, and in b) and d), the other side is fastened. The fixed positions of the two sides of the mount are freed before the tensile machine starts to elongate the sample. d) shows a fractured sample.

D Fracture surface

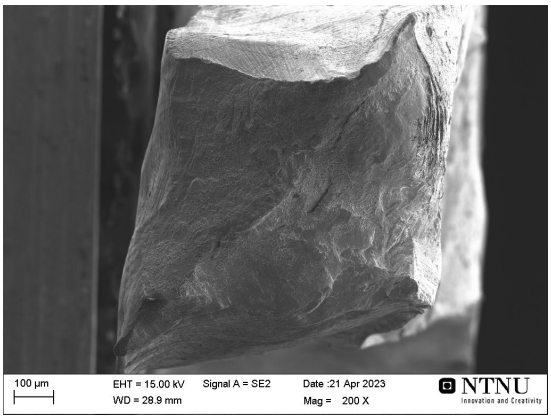

(a) $CuAl7_a$

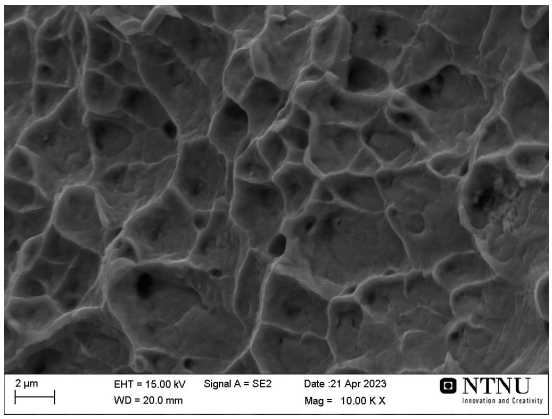

(b) $CuAl7_a$

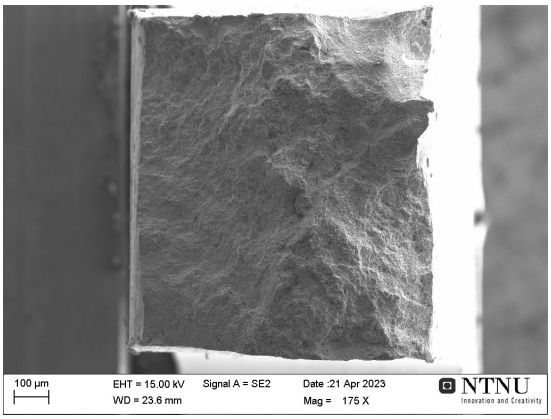

(c) $Interface_{v(2)}$

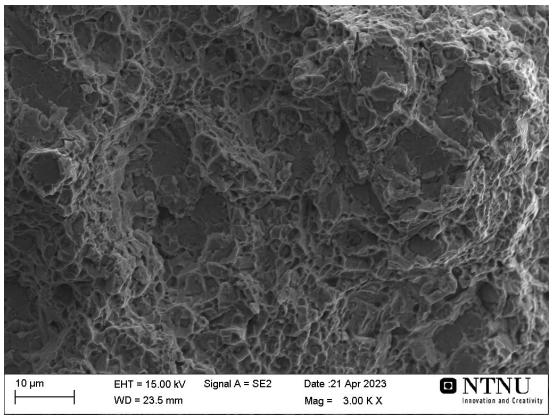

(d) $Interface_{v(2)}$

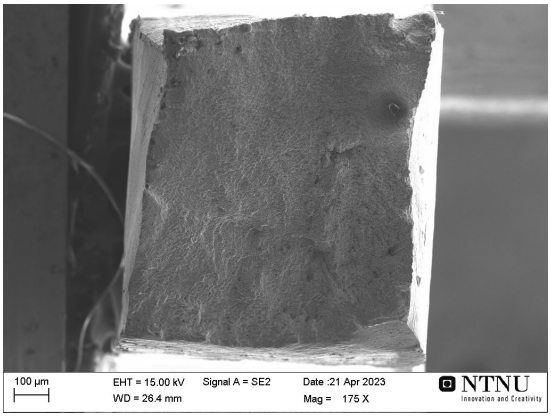

(e) $IN718_a$

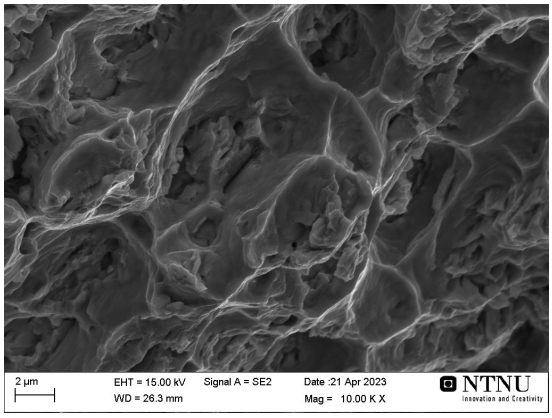

(f) $IN718_a$

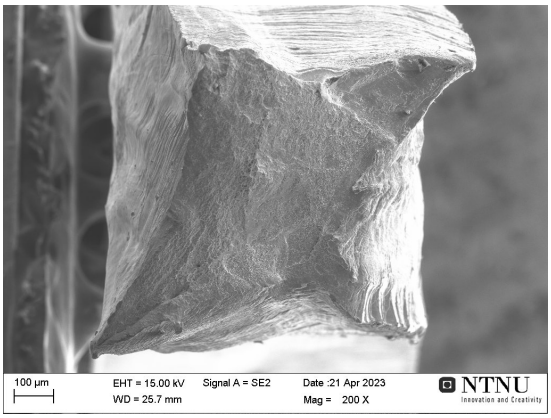

(g) $CuAl7_v$

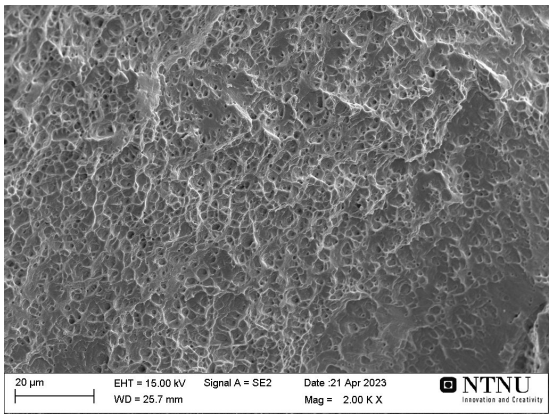

(h) $CuAl7_v$

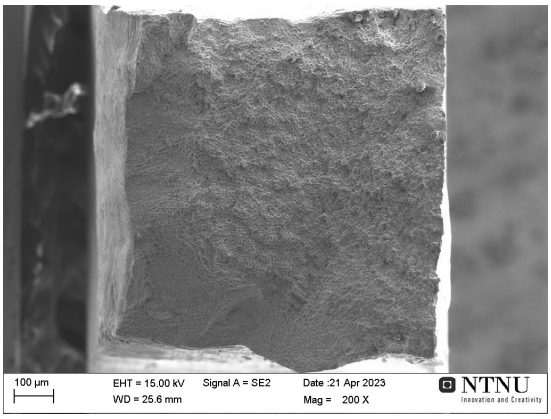

(i) $IN718_v$

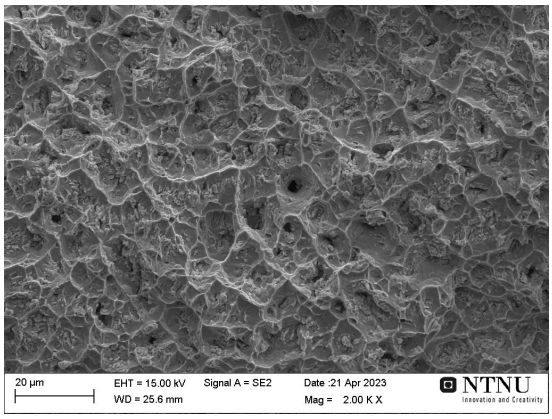

(j) $IN718_v$

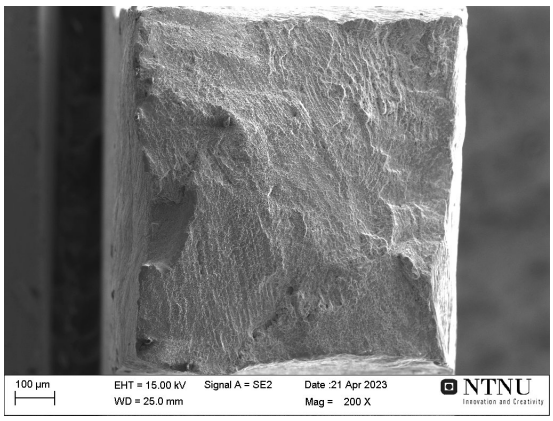

(k) $IN718_h$

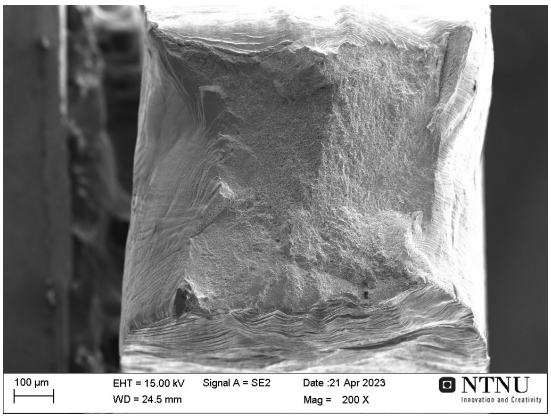

(l) $CuAl_{h(2)}$

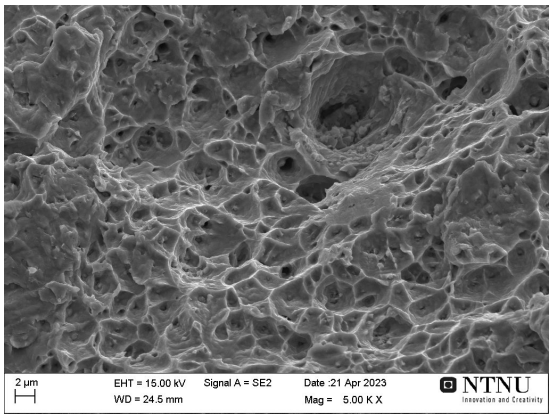

(m) $CuAl_{h(2)}$

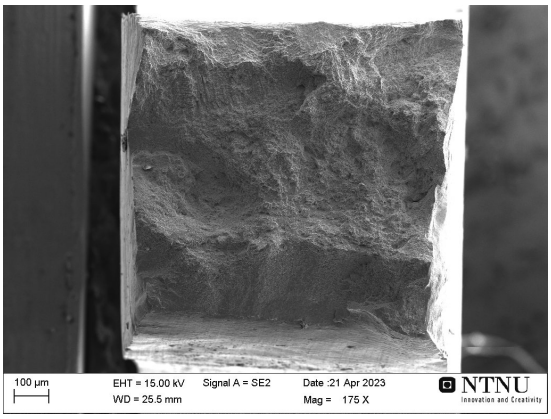

(n) $Interface_h$

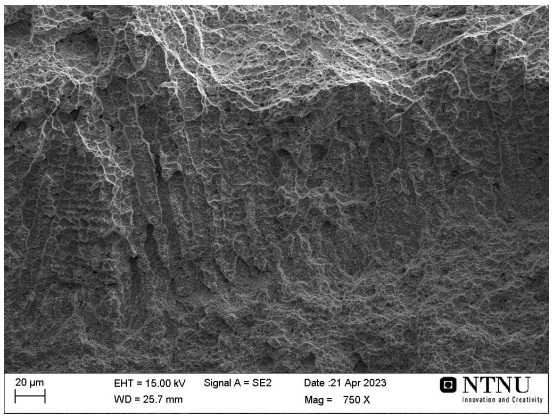

(o) IN718-rich $Interface_h$

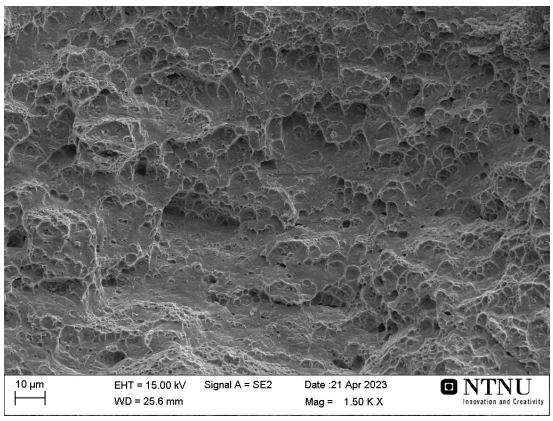

(p) CuAl7-rich $Interface_h$

Figure D.1: SE images of fracture surfaces obtained after tensile testing (to the left) and magnified SE images of the sample surface morphology (to the right).

E Hardness testing

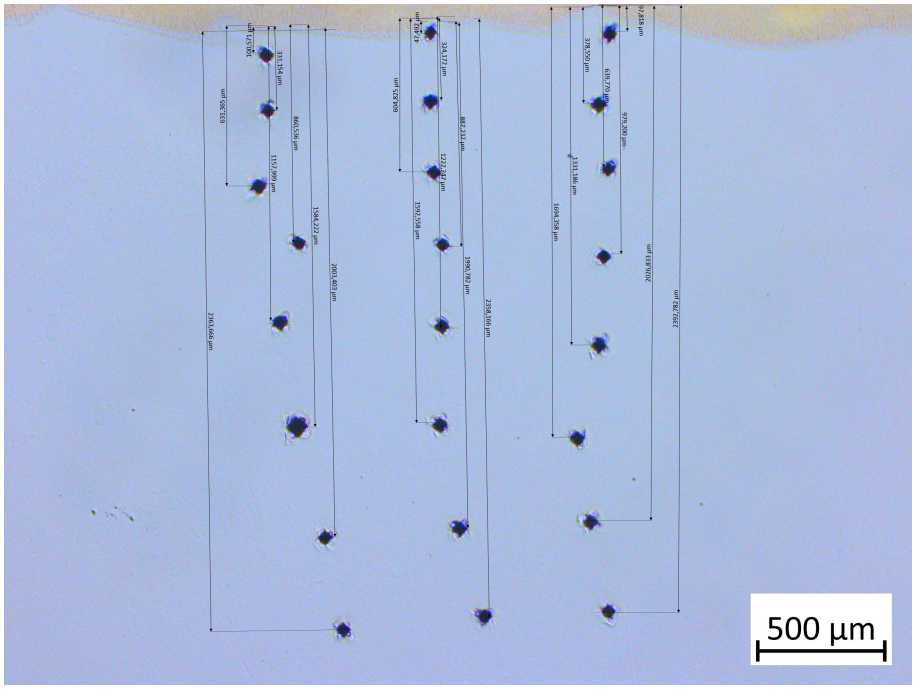

Figure E.1: Measure of distances from indent to interface in IN718 using the optical microscope software.

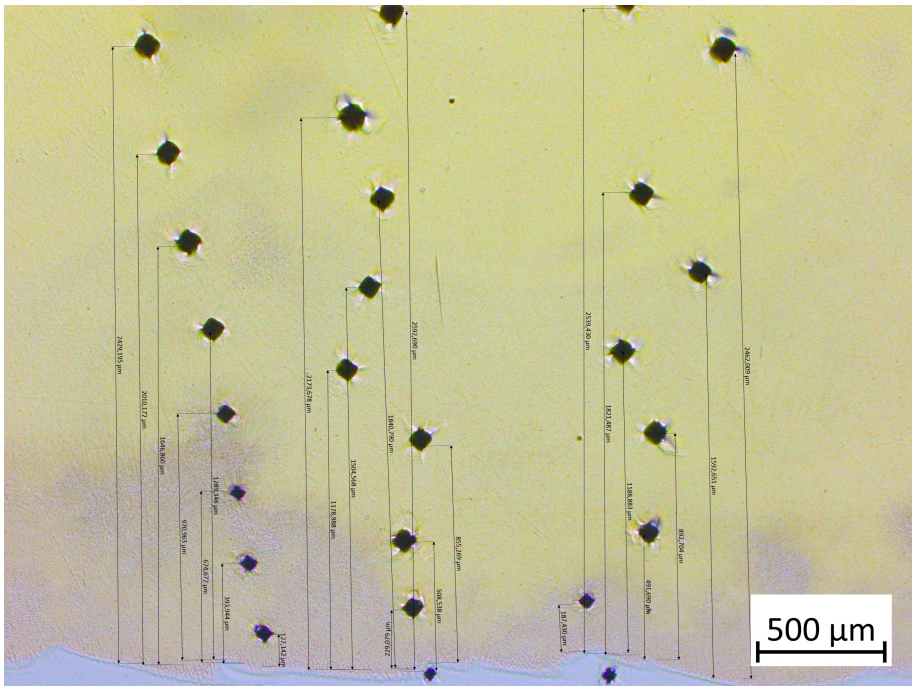

Figure E.2: Measure of distances from indent to interface in CuAl7 using the optical microscope software.

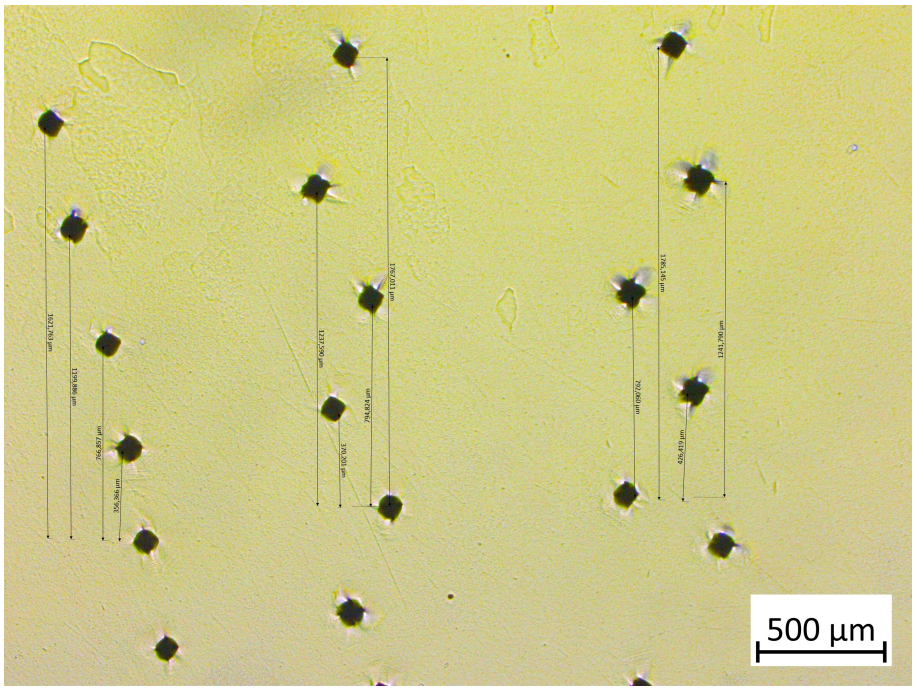

Figure E.3: Measure of distances from indent to interface further into CuAl7 using the optical microscope software.

F Further work

Some experiments were performed in the deposition of CuAl7 onto blasted S235 carbon steel. A four-layered deposition was applied on the substrate with a preheat induced prior to the printing. Macropictures of the result are shown in Figure F.1. Two different parameter combinations were used, presented in Table 17. The deposition showed good fusion between the two materials, with no bulk material defects. However, the surface roughness was higher in Sample (a) but the edges were more rounded in Sample (b) deviating from the desired geometry.

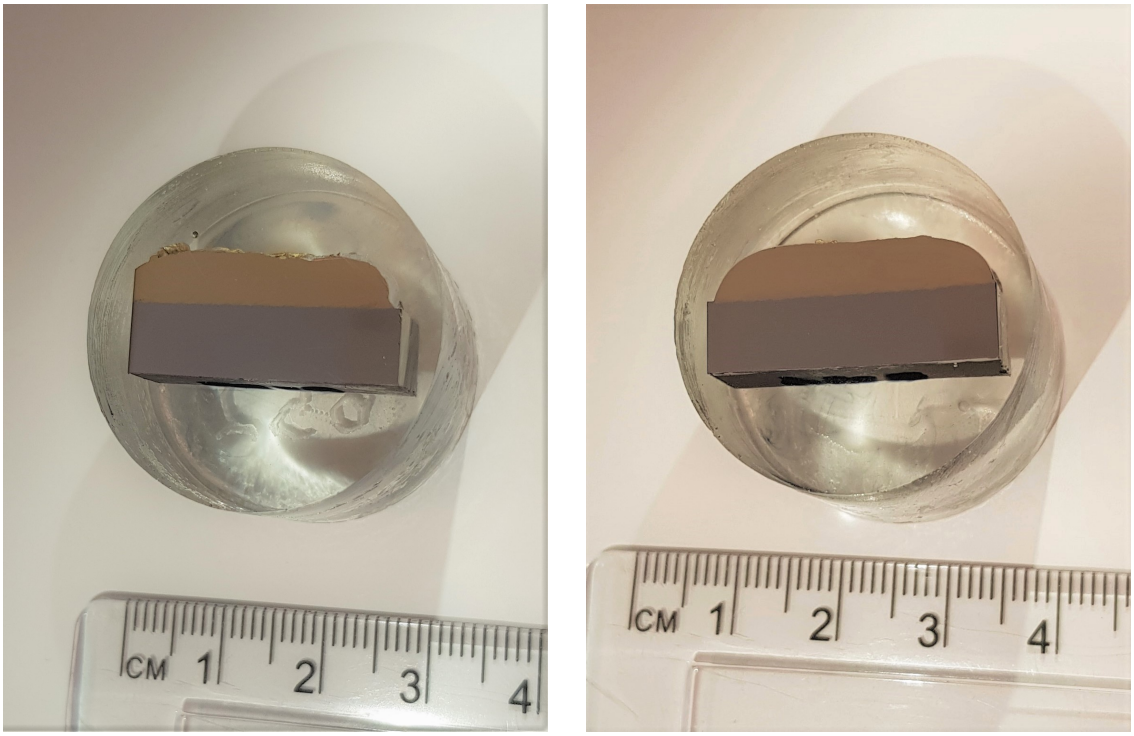

(a) (b)

Figure F.1: Deposition of CuAl7 onto S235 carbon steel for further work.

Table 17: Process parameters used for specimen manufacturing by LMWD. P is the laser power, v_t is the traverse speed, v_w represents the wire feed rate and P_w is the hot wire power, while Z and d are the laser beam focal position and the hatch spacing, respectively.

Test	$P[W]$	$v_t[mm/s]$	$v_w[mm/s]$	$P_w[W]$	$Z[mm]$	$d[mm]$	*Preheat[℃]*
(a)	1200	10	11	100	0	1.3	330-480
(b)	1200	8	8	100	0	1.3	360-500

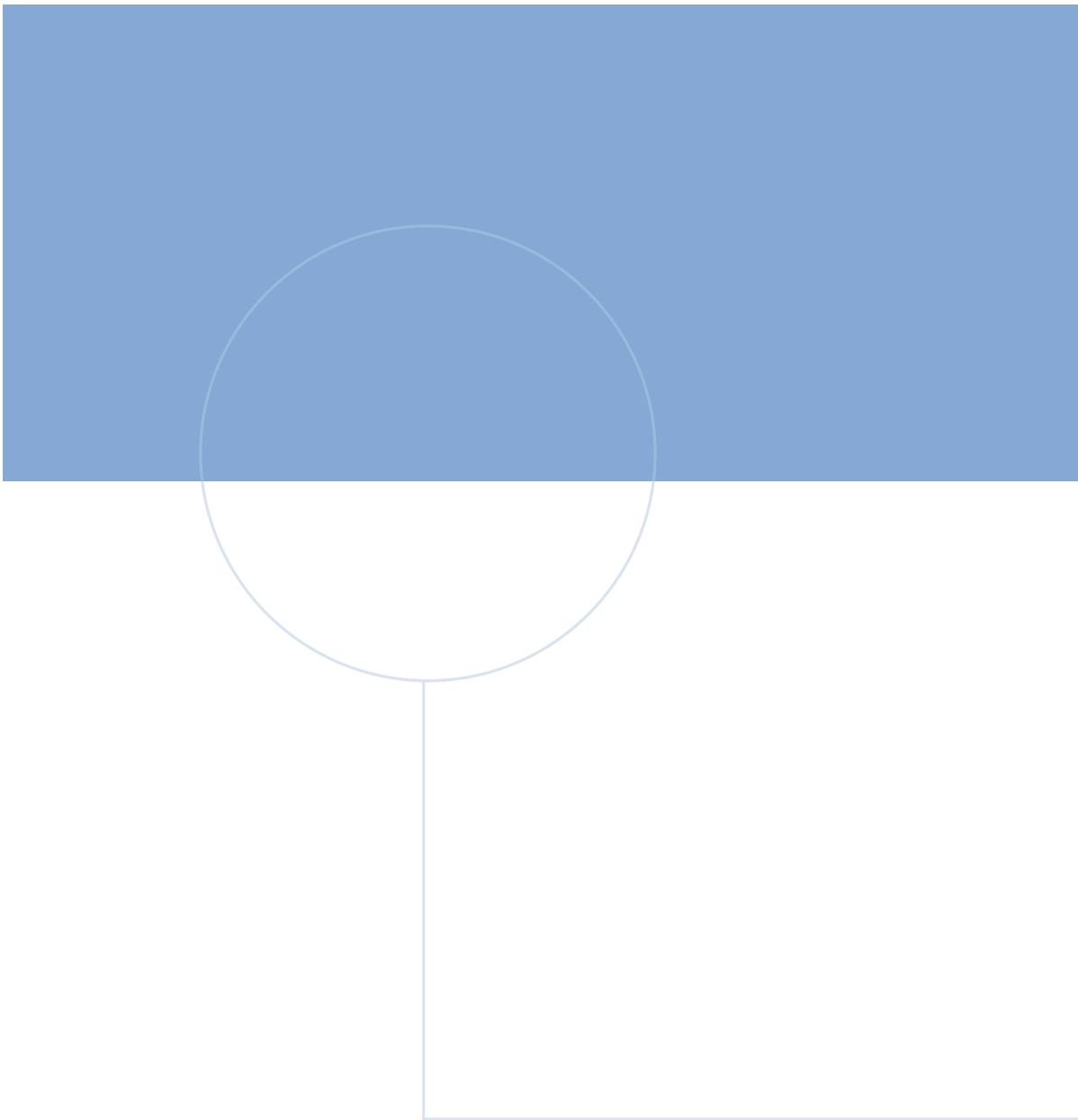

NTNU

Norwegian University of
Science and Technology